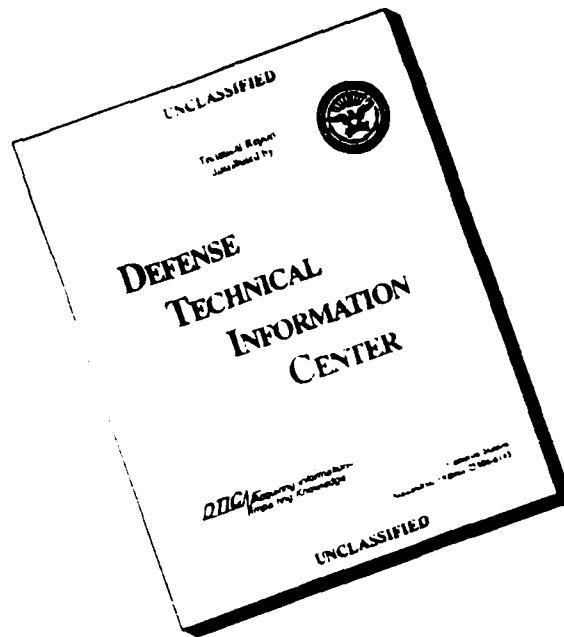


DISCLAIMER NOTICE



THIS REPORT IS INCOMPLETE BUT IS THE BEST AVAILABLE COPY FURNISHED TO THE CENTER. THERE ARE MULTIPLE MISSING PAGES. ALL ATTEMPTS TO DATE TO OBTAIN THE MISSING PAGES HAVE BEEN UNSUCCESSFUL.

AFOSR-TR- 94 0156

Approved for public release;
distribution unlimited.

**EXPERIMENTAL STUDIES OF HYPERSONIC
TRANSITIONAL AND TURBULENT BOUNDARY LAYERS IN
HYPERSONIC FLOW**

FINAL REPORT
GRANT NO. AFOSR-91-0273

December 1, 1993

Prepared For:

Air Force Office of Scientific Research
Bolling Air Force Base
Washington, DC

Prepared By:

Michael S. Holden
Calspan-UB Research Center
Buffalo, NY 14225
(716) 631-6853

94-12119



94 4 20 145

Abstract

The objective of this program of fundamental research into transitional and turbulent flows is to advance the experimental knowledge of the detailed structure of transitional and turbulent flows in regions of attached and separated viscous/inviscid interaction. The experimental program has been conducted in high Reynolds number hypersonic flow for conditions where we believe compressibility and turbulence non-equilibrium effects are of key importance. Six basic studies have been conducted in this program. The first is an experimental program in which detailed characteristics of turbulent structures are to be examined using electron-beam techniques. Flowfield measurements with both non-intrusive and intrusive instrumentation were designed to obtain the streamwise variation of turbulent scale size and density fluctuation through the interaction regions. The surface and flowfield fluctuation measurements were used to determine the magnitude and mechanism of large scale flow instabilities. The electron beam fluorescence equipment provides us with density fluctuation measurements with which to evaluate the magnitude of turbulent compressibility effects in these flows. In the second study, we have examined transitional and turbulent flows in regions of adverse pressure gradient along an inlet ramp. Detailed heat transfer and pressure measurements were made on the "Johns Hopkins Generic Inlet Configuration" at Mach numbers from 8 to 12. This program was conducted with internal and AFOSR funds and provided unique information on the mean and fluctuating characteristics of transition regions in hypersonic flow over curved compression inlets. In the third study, we have examined transitional and turbulent flows along the stagnation line of a highly swept cylinder. These measurements of crossflow transition along the leading edge of a swept hypersonic wing were acquired in a program funded internally with instrumentation acquired on an AFOSR program. This program provided the only known data to provide correlations of the occurrence of incipient transition and turbulent heating along the attachment line of a swept leading edge in the Mach 8 to 13 range. The program was conducted in the Calspan 48" shock tunnel and provided information on the mean and fluctuating characteristics of transitional and turbulent flows along the attachment line and around the leading edge. The fourth experimental study was conducted to examine the relaminarization of a turbulent boundary layer in regions of strong favorable pressure gradient. In the fifth study we examined the 3D interaction regions generated by single and double fins. Measurements of heat transfer and pressure were obtained in regions of separated shock-boundary layer interaction at Mach numbers of 8. This program was conducted with models and instrumentation which were employed in an earlier program for

NASA-Langley. Measurements were made for a wide range of fin angles producing attached and separated regions with and without film cooling. The measurements obtained in this program are being compared with similar measurements made at lower Reynolds numbers by Horstmann in the Ames 3.5 foot blow-down tunnel.

Accession For	
NTIS GRA&I	<input checked="" type="checkbox"/>
DTIC TAB	<input type="checkbox"/>
Unannounced	<input type="checkbox"/>
Justification	
By _____	
Distribution/	
Availability Codes	
Dist	Avail and/or Special
<i>R-1</i>	

TABLE OF CONTENTS

<u>Section</u>		<u>Page No.</u>
1	INTRODUCTION	1
2	SUMMARY OF CODE VALIDATION EXPERIMENTS CONDUCTED.....	3
	2.1 Introduction	3
	2.2 Electron Beam Measurements of Turbulent Flow Structure in Hypersonic Flows.....	6
	2.3 Transitional Flows Over Curved Compression Surfaces.....	15
	2.4 Attachment Line Transition on Swept Leading Edges	19
	2.5 Studies of Relaminarization in Strong Favorable Pressure Gradients	23
	2.6 Studies of 2D and 3D Crossing Shock Interaction With/Without Helium Film Cooling	27
3	CONSTRUCTION OF A DATABASE OF MEASUREMENTS IN HYPERSONIC FLOW FOR CFD CODE VALIDATION.....	34
	APPENDIX 1.....	A1
	APPENDIX 2.....	A2
	APPENDIX 3.....	A3

LIST OF FIGURES

<u>Figure No.</u>		<u>Page No.</u>
1	Nine-Foot-Long, sharp 6° Cone/30° Flare Model Installed in Calspan's 96-Inch Shock Tunnel.....	7
2	Installation Drawing of Cone/Flare Model in Calspan's 96-Inch Tunnel	8
3	General Layout of Electron-Beam Apparatus in Cone/Flare Model	9
4	Drawing of Cone/Flare Model and Vacuum System	10
5	Diagram of Modified Optical System for Boundary Layer Measurements.....	12
6	E-Beam Gun Installation in Axisymmetric Curved Compression-Ramp Model	13
7	Inlet Compression Ramp Installed in 48" Shock Tunnel	16
8	Distribution of Heat Transfer and Pressure on Compression Ramp for Three Reynolds Numbers at Mach 11	17
9	Swept Cylinder Model and Instrumentation.....	20
10	Streamwise View of Swept Cylinder Model with Float Plate Attached..	21
11	Heat Transfer Measurements Transition Region on Swept Cylinder.....	22
12	Flat Plate Expansion Ramp Model	24
13	Distribution of Heating Rate in Turbulent and Relaminarizing Flow..... on Expansion Surface	25
14	Flat Plate Film Cooling Model with Vertical Shock Generators Installed.....	28
15	Instrumentation Positions on Film Cooling/Shock Interaction Model ...	29
16	Heat Transfer Distribution Profiles of Crossing Shock/Film Coolant Interaction	32

LIST OF TABLES

<u>Table No.</u>		<u>Page No.</u>
1	Key Phenomenology in Hypersonic Flow Regimes.....	4
2	Run Matrix.....	31

1. INTRODUCTION

Direct experimental simulation of complete aerodynamic configurations has in the past been the backbone of design efforts for new aerospace vehicles. However, the emergence of advanced high-speed computing capabilities and numerical techniques, coupled with major increases in the need for numerical solutions to the full and reduced Navier-Stokes equations, has resulted in a re-focusing of both pure and applied experimental research. Recent applied experimental research has been increasingly directed toward acquiring more detailed measurements on segments of such configurations for computation-code "validation" purposes. This is particularly true for hypersonic-vehicle design, where complete experimental simulation is difficult above Mach 13, likewise, in pure research, the role of recent experiments has been increasingly one of providing insight into the macroscopic modeling of the flow (e.g., turbulence modeling) rather than as a means of constructing and validating gross flowfield models. In both cases, there is an increasing emphasis on the determination of flowfield properties, which in many cases provide the more direct and definitive evaluation of the modeling employed in the codes. The increased emphasis on transitional and turbulent interacting and separated flows has resulted in a key need for time-resolved measurements over a broad frequency range. These requirements place a premium on flow quality and duration of tests, as well as on sophisticated high-frequency surface and flowfield instrumentation.

The intense use of numerical solutions of full or reduced time-averaged Navier-Stokes equations, in the NASP program, has resulted in significant progress in the development of efficient and stable numerical algorithms and in greater understanding of gridding techniques. However, little real progress has been made in developing the fluid mechanical models required for these codes. In many instances, the phenomena of greatest importance in the aerothermal design of advanced vehicles are also the most difficult to model in the codes. The aerothermal loading and flowfield distortion that often accompany regions of transition and viscous/inviscid interaction in hypersonic flow present some of the most important and difficult problems for both the designer and the predictor. Compressibility effects, shock/turbulence interaction, and the gross instabilities associated with separated flows must also be studied. In hypersonic flows, modeling of turbulence in regions of strong pressure gradients, embedded shocks, and separated flow is one of the most difficult and important problems.

To provide the information required to construct and verify the transitional turbulence models used in the codes, flowfield measurements and direct measurements of skin friction and heat transfer must be obtained. Surface pressure data provide little information to validate codes and do not provide insight for turbulence modeling. To understand the structure of hypersonic turbulent boundary layers and shear layers as well as boundary layer separation in regions of shock/wave boundary layer interaction, we must understand the structure of the flow at the base of the boundary layer (at the wall and sublayer of the turbulent flow). Such measurements can be made only with non-intrusive measurements with high spatial resolution on large models. As difficult as it is to make such measurements in high-enthalpy hypersonic flows, only by obtaining both the mean and fluctuating components of these flows can sufficient evidence be obtained to construct meaningful models of these flows.

Table 1 Key Phenomenology in Hypersonic Flow Regimes

FLOW REGIME	PHENOMENA	IMPORTANCE
Free Molecular and Laminar Nonequilibrium Hypervelocity Flows	Shock Layer/Boundary Layer Chemistry and Radiation Effects Flowfield Chemistry and Surface Catalysis Gas/Surface Interaction	Optical Windows and "Red-Out" Prediction Vehicle Stability and Heating Re-Entry Body Drag and Stability
Boundary Layer Transition and Relaminarization	Nosetip and Forebody Transition in Favorable and Adverse Pressure Gradients Attachment Line Transition Shear Layer Transition Relaminarization	Nosetip and Forebody Design and Inlet Aerodynamics Attachment Line Heating Shock/Shock Interaction Heating Scramjet Nozzle Design
HYPERSONIC TURBULENT FLOWS Shock/Boundary Layer Jet Interaction Turbulent Mixing and Combustion	Turbulent Nonequilibrium and Compressibility Effects Turbulent Modeling for Mixing and Real Gas Effects Shock/Turbulence Interaction	Scramjet Engine Design Control Surface Performance Combustor Performance Seeker Head Performance

is the development of advanced hypervelocity facilities designed to operate at extremely high energy and pressure levels, and produce high-quality, well-defined flows.

Predicting the occurrence and characteristics of two- and three-dimensional shock wave turbulent boundary interaction are of critical importance in the design of airbreathing hypersonic vehicles and represent one of the most difficult tasks in computational fluid dynamics. Obtaining detailed information with which to formulate and validate models of turbulence behavior in regions of strong pressure gradient where compressibility and shock turbulence interaction are of key importance to the development of our predictive design capability. At Mach numbers above 8, the length and structure of the boundary layer transition region can play an important role in determining the boundary layer flow entering the combustion chamber, and in turn the efficiency of a Scramjet engine. There is little or no information on how the adverse pressure gradient, developed on the curved inlet ramp, decreases the length of the transition region and controls the development of the turbulent scales, which in turn influences the overshoot of heat transfer at the end of the transition process. In order to predict the heating levels to the highly swept leading edges of hypersonic vehicles, it is essential to obtain information on the occurrence of transition along the stagnation line. There is almost no experimental measurement of attachment line transition at freestream Mach numbers above 8, thus experimental data to provide transition criteria and information on the magnitude of turbulent stagnation line heating is of key importance. The large expansions which occur as the flow exits through the combustor into the nozzle of a Scramjet engine could give rise to relaminarization. Although relaminarization has been observed in supersonic flows and on nosetips in hypersonic flow, there is little evidence the relaminarization could play a significant role in Scramjet propulsion. In the following section, we summarize the results of our studies of hypersonic viscous/inviscid interaction in turbulent flows, transitional flows over compression ramps and along highly swept leading edges, relaminarization in regions of strong adverse pressure gradient and finally the three-dimensional separated regions induced by single swept shocks and crossing shock interactions.

2.2 Electron Beam Measurements of Turbulent Flow Structure in Hypersonic Flows

In this experimental program, we are studying the mean and fluctuating turbulent flow structure over two basic flow configuration: (i) a large cone/flare model and (ii) an axisymmetric curved compression ramp. The measurements made in each of these flows will be designed principally to examine the response of the turbulent flow structure in a flow strained by an adverse pressure gradient-in one case, with a strong embedded shock system. We are also studying the development of the turbulent structure as it is allowed to relax under constant pressure on the conical flare. Flowfield measurements with both non-intrusive and intrusive instrumentation are to be focused on obtaining the streamwise variation of turbulent scale size through the interaction regions. We are also examining the surface and flowfield fluctuation measurements to determine the magnitude and mechanisms of large-scale flow instabilities in separated interaction regions. Here, we are also investigating the results of shock/turbulence interaction. Direct measurements of density and density fluctuation with the electron-beam fluorescence equipment are enabling us to determine directly the magnitude of turbulent compressibility effects in these flows.

To measure and understand the important changes in the turbulent flow structure that occur when a hypersonic turbulent boundary layer is subjected to strong adverse pressure gradients and flow separation, it is essential that detailed information be obtained in the laminar sublayer and in the wall layer. Since the wall layer is less than one-tenth of the boundary layer thickness and the resolution of most instrumentation is not better than 0.01 inch, boundary layer thicknesses of at least 1 inch are necessary for these studies. Thus, very large models are required, and we are accomplishing this by using a large slender cone model with three flare configurations at the base (see Figures 1 and 2). As discussed earlier, we have successfully obtained surface and flowfield measurements with this configuration. The model is instrumented with high-frequency heat transfer, skin friction, and pressure instrumentation. The major flowfield instrumentation will be electron-beam fluorescence equipment, installed as shown schematically in Figure 3. The traverse mechanism, also shown in Figure 4, is enabling flowfield measurements to be made at streamwise stations encompassing the complete interaction region. High-frequency thin-film, pitot pressure, and total temperature measurements will be made at each streamwise station of interest. Measurements are also being made using an axisymmetric curved compression-ramp model constructed for a

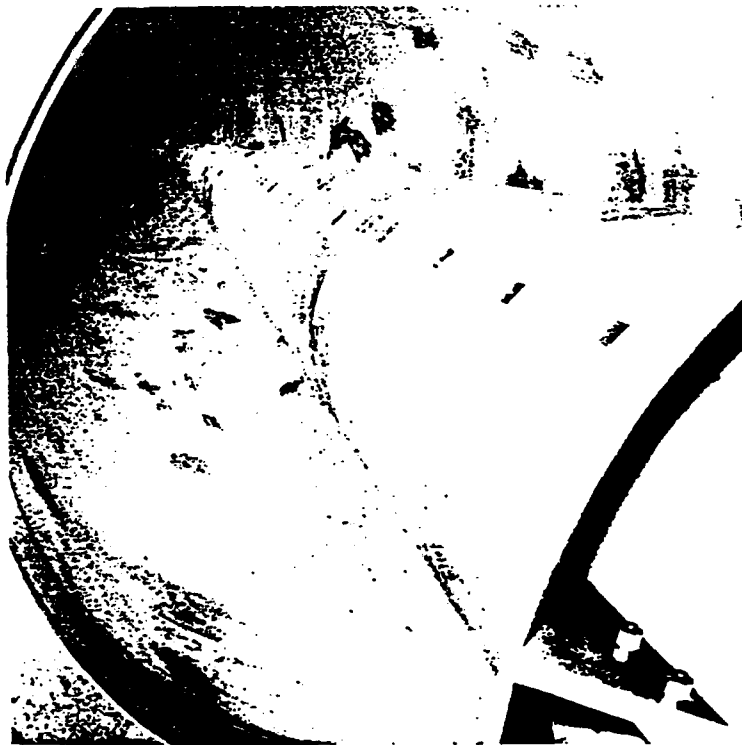
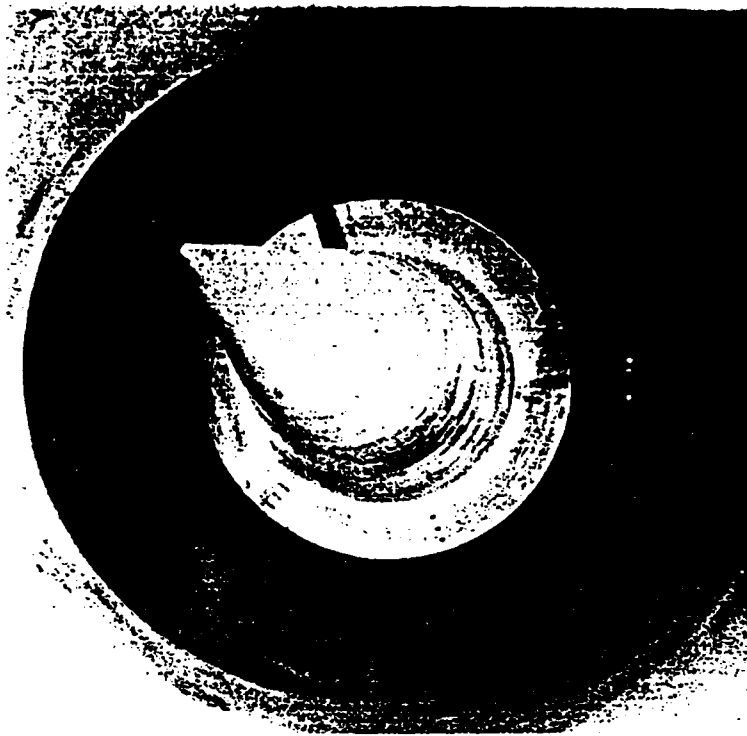


Figure 1 Nine-Foot-Long, Sharp 6° Cone/30° Flare Model
Installed in Calspan's 96-Inch Shock Tunnel

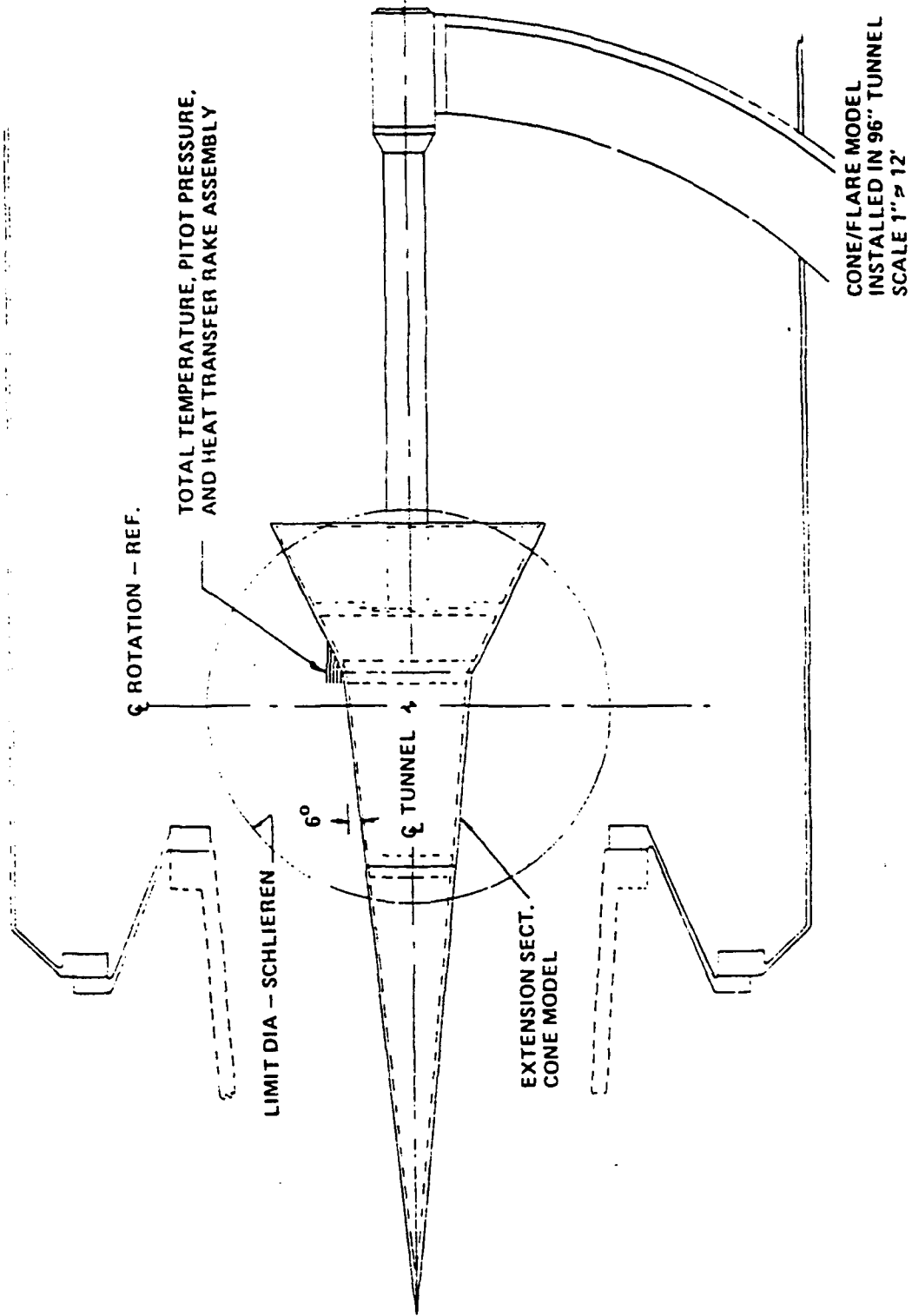


Figure 2 Installation Drawing of Cone/Flare Model in
Calspan's 96-Inch Tunnel

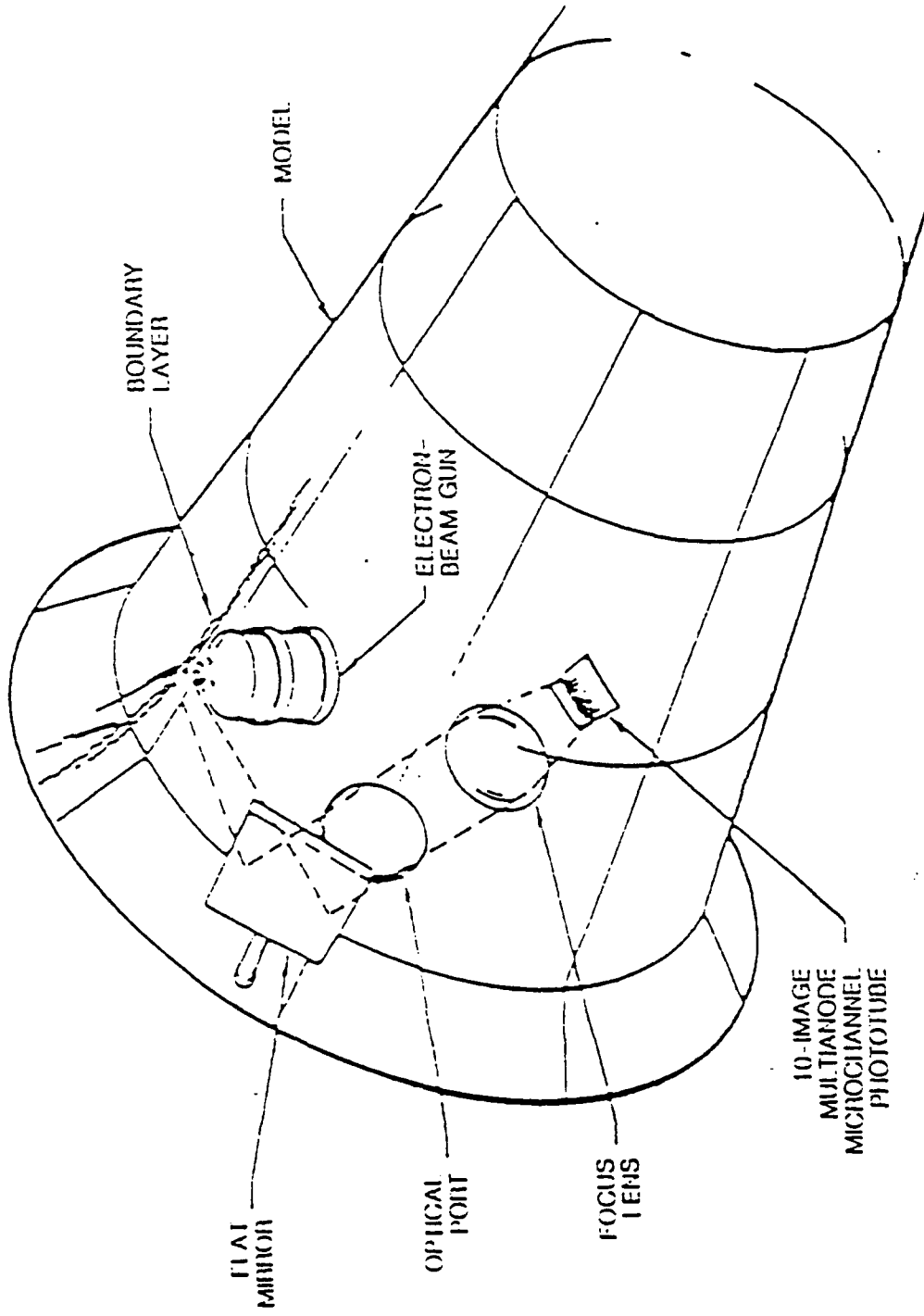


Figure 3 General Layout of Electron-Beam Apparatus in Cone/Flare Model

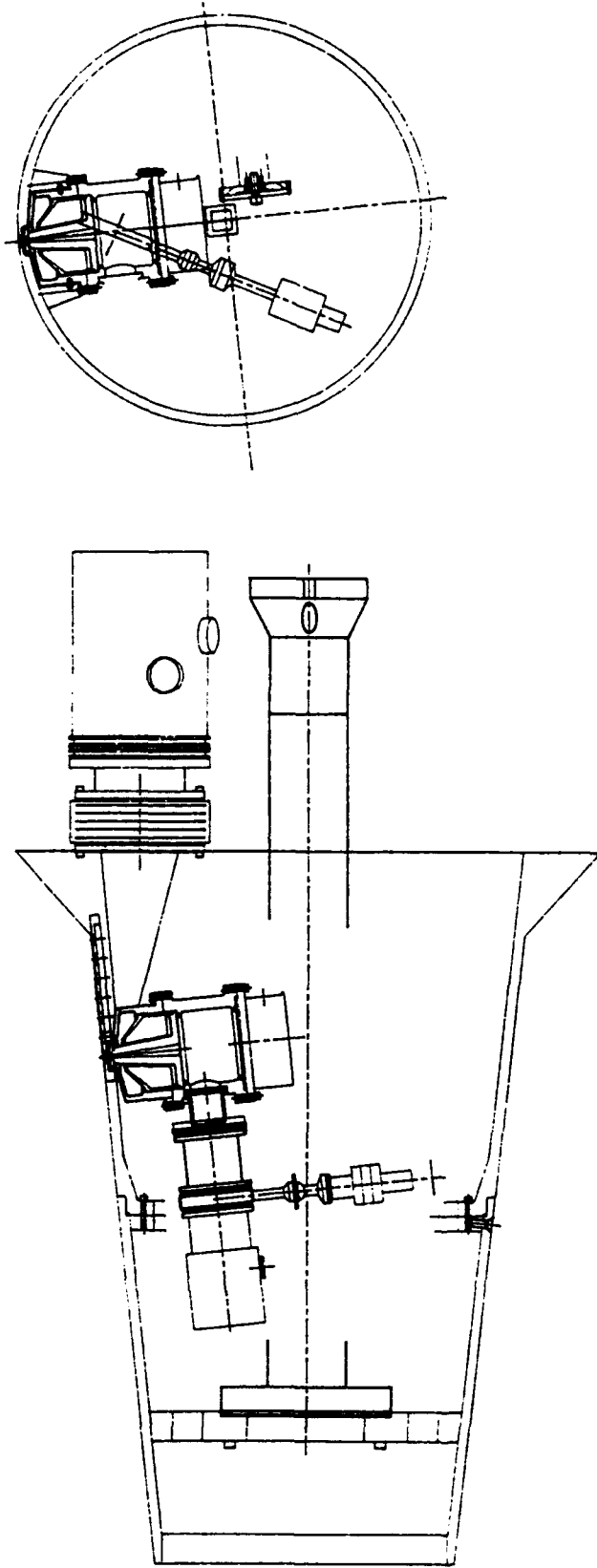


Figure 4 Drawing of Cone/Flare Model and Vacuum System

complementary research program for NASA. Our large-aperture, custom-designed optical system (Figure 5) is enabling us to record and analyze turbulent fluctuation measurements up to a frequency of 1 MHz. These optics are giving us the ability to obtain a 0.010-inch resolution across the 1.5-inch boundary layer. The 10-channel photodetector system will have a frequency response of up to 1 MHz.

In these studies, we are obtaining detailed surface and flowfield measurements for three cone/flare configurations to obtain attached, incipient separated, and well-separated interaction regions, respectively. Our earlier studies suggest that flare angles of 27, 30, and 33 degrees are required to generate these flows. The major focus of the experimental program is on defining the mean and fluctuating flowfield through the region of shockwave/boundary layer interaction at the cone/flare junction and over the flare. Flowfield measurements using high-frequency pitot pressure, thin-film, and total temperature probes and a ten-channel electron-beam fluorescence system is obtained simultaneously, at each streamwise location of interest, from instrumentation placed radially around the model. Double-pulsed holographic interferometry is used to determine both the mean flowfield density distribution and, with pulse separation to the order of 1 microsecond, the variation of turbulent scale size through the interaction region. We are also investigating the use of a pulsed electron beam coupled with downstream electron detectors to obtain direct measurements of the streamwise convective velocity distribution across the boundary layer.

The experimental studies conducted with the large axisymmetric curved compression-ramp surface (See Figure 6) is providing information on the stream wise and transverse variations of turbulent scale size in a moderate adverse pressure gradient for turbulence-modeling evaluation. These studies will be conducted at freestream Mach numbers from 11 to 15 or local Mach numbers from 9 to 12. Surveys are being made at a series of streamwise stations beginning just ahead of the curved compression ramp and continuing along the conical afterbody section downstream of the curved compression-ramp section. The model is being instrumented with high-frequency skin friction, heat transfer, and pressure instrumentation. High-frequency total pressure and total temperature probes as well as hot-film instrumentation is being used to obtain intrusive flowfield measurements. As in the earlier studies, we are employing electron-beam fluorescence equipment and holographic interferometry to obtain non-intrusive mean and fluctuating measurements of the flowfield.

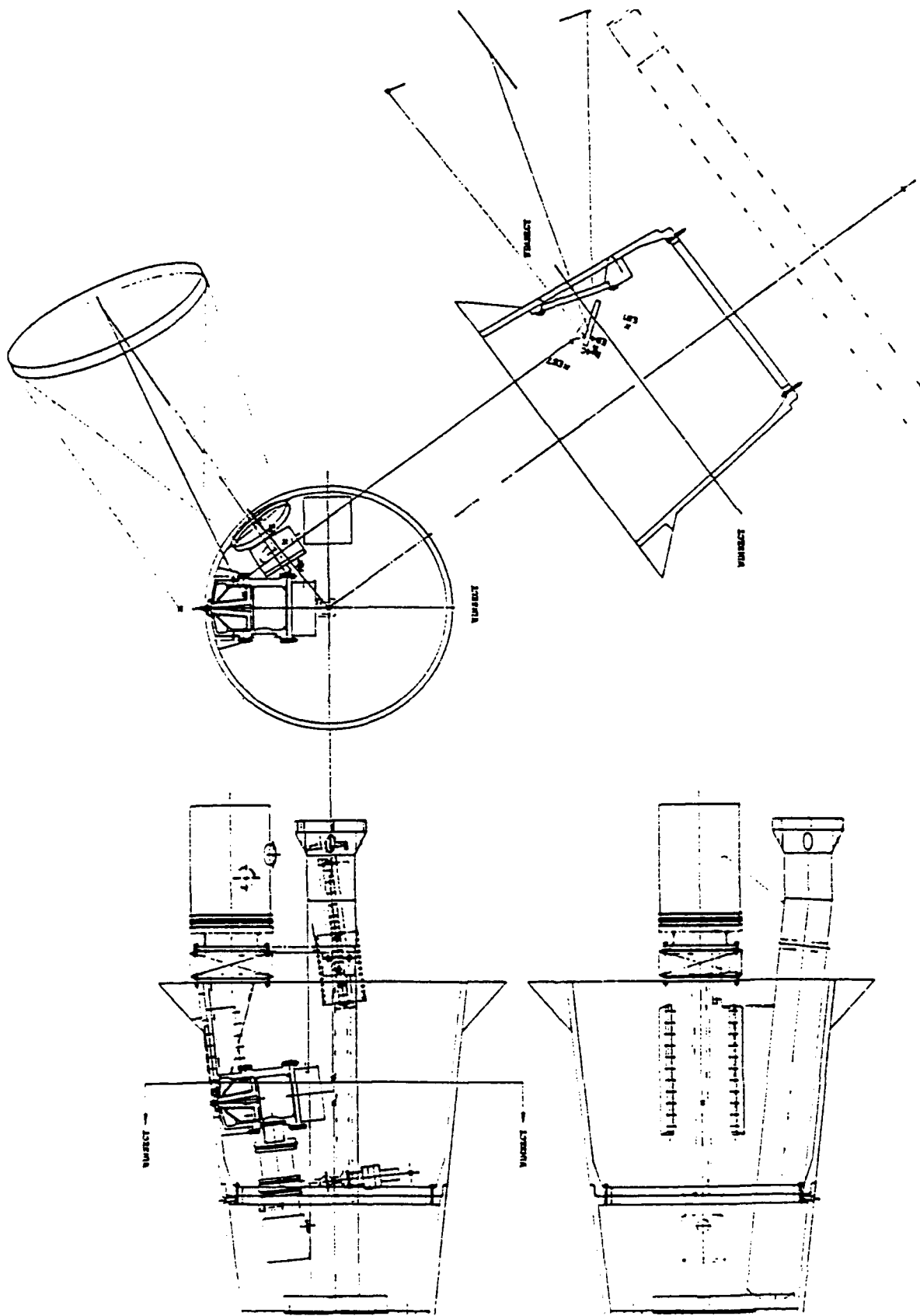


Figure 5 Diagram of Modified Optical System for Boundary Layer Measurements

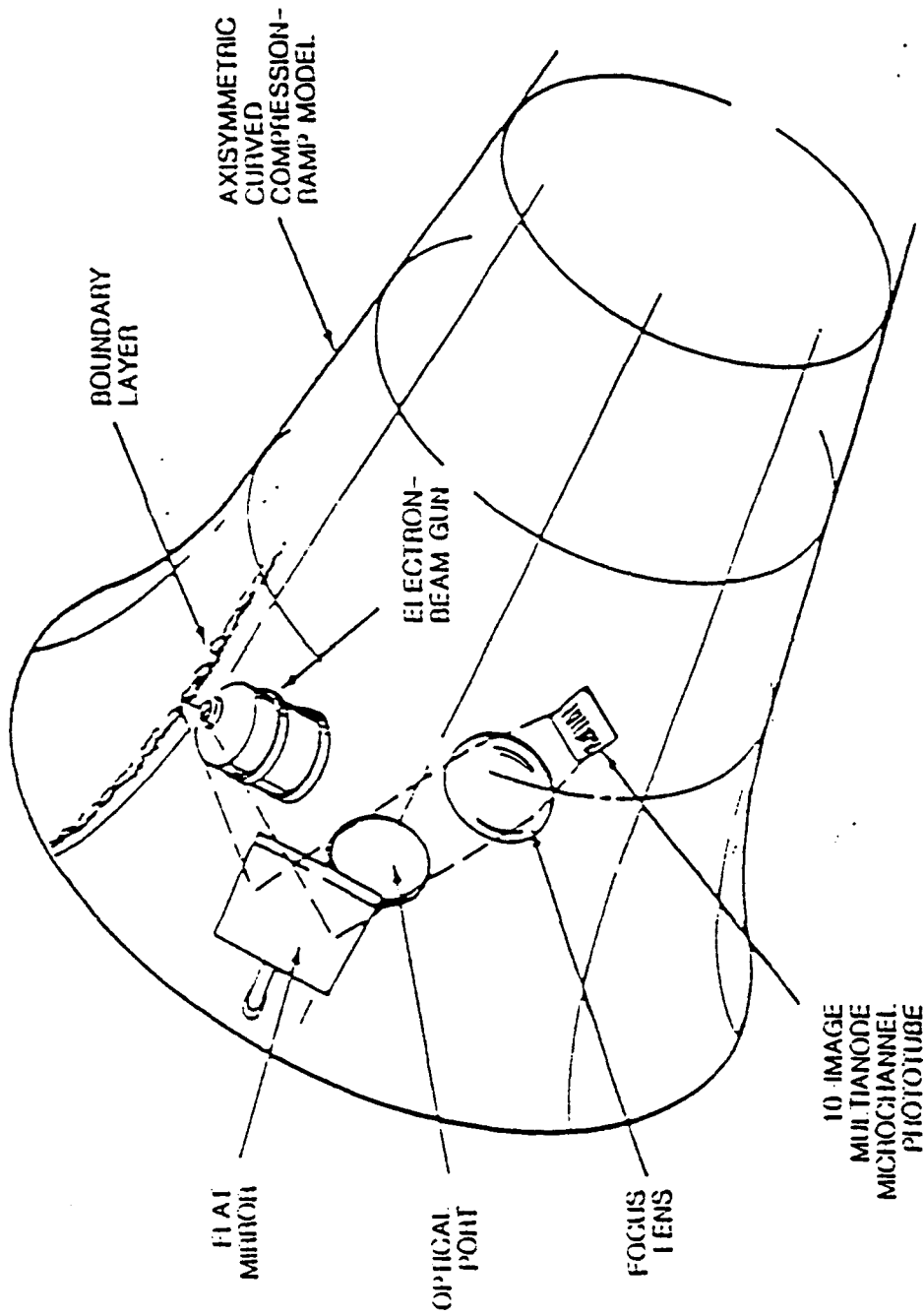


Figure 6 E-Beam Gun Installation in Axisymmetric Curved Compression-Ramp Model

The mean distributions of the flow properties across the boundary layers and shear layers are determined from the probes and from the electron-beam and interferometry measurements, so we have a number of independent ways of calculating the same property. For example, the mean density can be deduced independently from measurements using the electron beam, using interferometry, and using a combination of total temperature and total pressure measurements. Static temperatures can be determined directly from the electron-beam measurements and from a combination of probe measurements. The major efforts in analysis of the measurements are being directed towards the definition of the turbulent and unsteady structure of these flows. The knowledge of the streamwise and transverse variation of turbulent scale size through the interaction regions is of key importance to the evaluation of the models of turbulence. Scale size measurements are being determined independently from cross-correlations of transverse-fluctuation measurements with those obtained using electron-beam, pitot pressure, and thin-film instrumentation. Turbulent spectra is also being obtained from the various measurement techniques to provide the correlations required for evaluating the turbulence models and for providing insight into the fluid mechanics associated with compressibility effects, shock/turbulence interaction, and large scale flow unsteadiness. Through all phases of this program, we are working closely with other members of the AFOSR team (in particular, with Dole Knight) to provide measurements of the greatest value in evaluating and improving the models of turbulence in hypersonic interacting flows. Early results from this study are reported in Appendix 2.

2.3 Transitional Flows Over Curved Compression Surfaces

In these studies, we examined transitional flows over a curved compression ramp at Mach numbers of 10, 11 and 12, over a range of Reynolds numbers to place the beginning of transition at various stations along the ramp. Here the objective was to examine how the length of the transition region, and the distribution of heat transfer within it, was influenced by the position of the transition onset in the pressure gradient, and the local Mach number. The principal instrumentation employed in this study were platinum thin-film gages because their high frequency response enabled us to determine the onset of transition, the development and convection of gross unsteadiness, and the end of transitional flow. The compression ramp used in this study, shown in Figure 7, was constructed with an initial constant angle ramp, followed by a curved section terminated in a second constant angle ramp section. The centerline of the ramp was extensively instrumented with thin-film instrumentation in the regions of interest, and pressure instrumentation was positioned to accurately determine the pressure gradients along the ramp.

Measurements were made for a series of Reynolds numbers at each of the three Mach number conditions. The unit Reynolds number of the freestream was varied to place transition at various points along the ramp. Figure 8 shows the distributions of heating along the compression ramp for a series of unit Reynolds numbers at a Mach number of 11. Also shown on this plot are the corresponding pressure distributions. It can be seen from the pressure data that there is little influence of boundary layer characteristics on the pressure distributions along the model. Pressure measurements also show that the curve compression ramp begins at 10 inches from the leading edge and extends to 21 inches from the leading edge. The small variation in pressure just downstream of the curve ramp results from the coalition of the compression waves and associated reflective wave structure. For the highest Reynolds number, transition begins on the initial ramp and is completed approximately half way along the curved compression surface. At this point, the heating continues to increase along the surface because of the increase in the pressure level. At the lowest Reynolds number, transition begins several inches downstream of the beginning of the curved section, continues along the entire curved section, and is completed on the third segment of the compression surface. Here we see that there is a significant overshoot in the heat transfer rate which reflects the generation of large scale instabilities. At the intermediate Reynolds number, which was selected to position transition at the beginning of the curve compression ramp,



Run 23. Mach 11. Re = 2.99E6
 Run 21. Mach 11. Re = 3.45E6

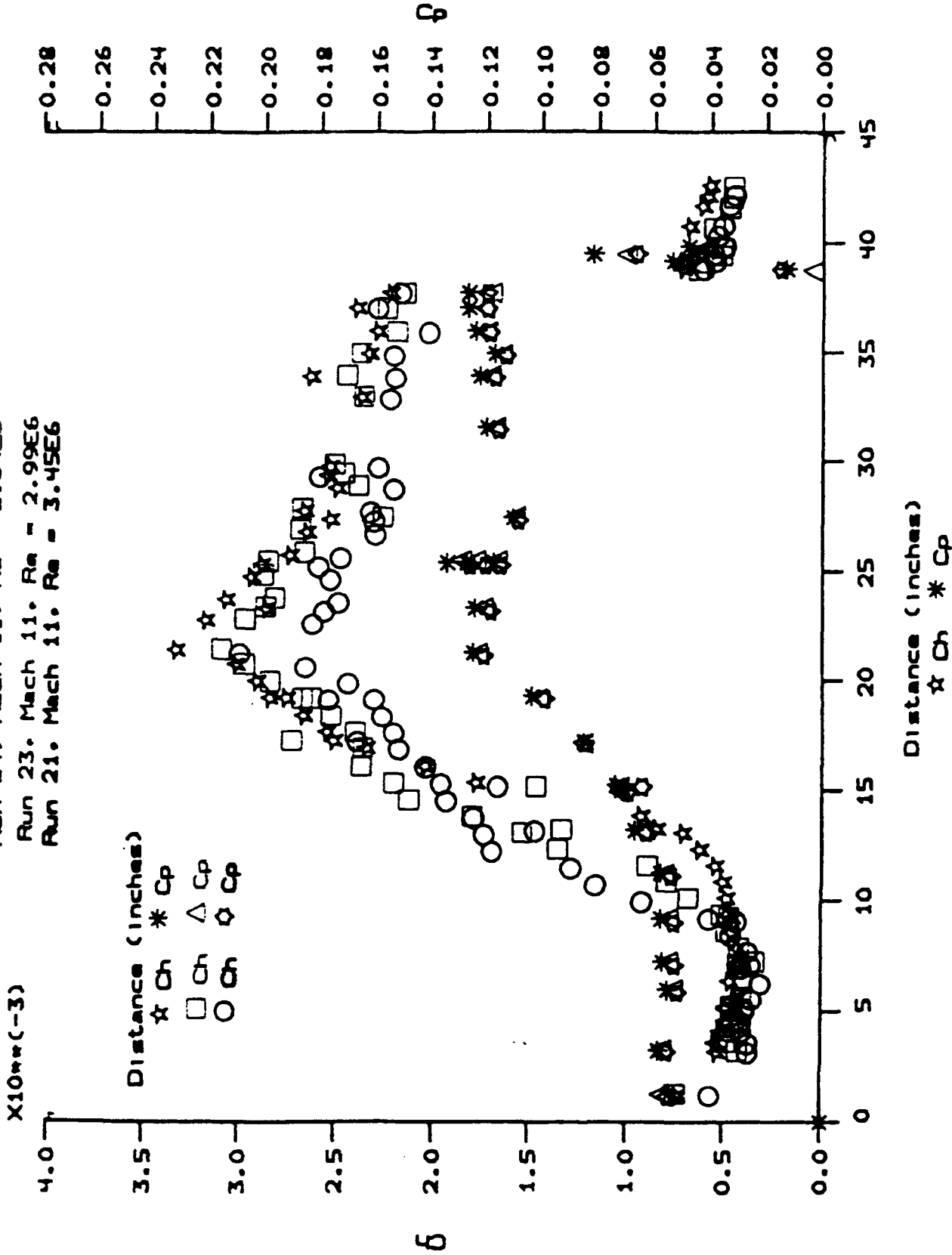


Figure 8 Distribution of Heat Transfer and Pressure
 on Compression Ramp for Three
 Reynolds Numbers at Mach 11

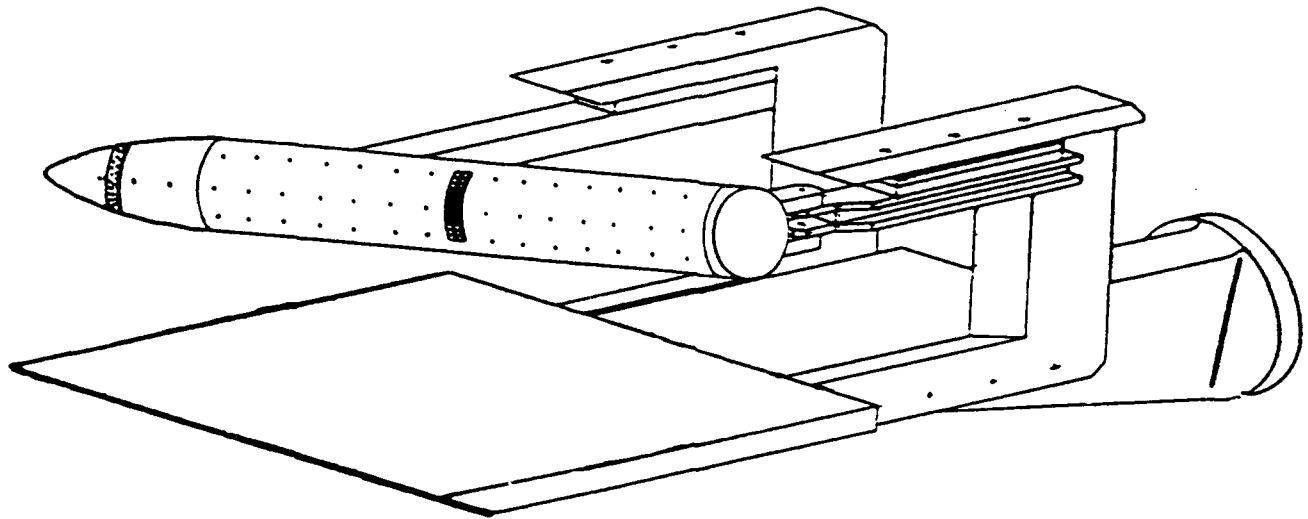
transition was completed just ahead of the end of the curve compression ramp with a measurable overshoot in the heating level. These measurements demonstrated that the length of the transition region can be shortened significantly by an adverse pressure gradient. In the current studies where both mean and fluctuation measurements were available, we observed that although the mean heat transfer distributions continue to rise downstream at the end of transition on the curved section, the distinctive nature of the rise and overshoot in the transition region can be used to determine the extent of transition if fluctuation measurements are not available.

2.4 Attachment Line Transition on Swept Leading Edges

The occurrence of transition on the stagnation line of a highly swept leading edge and the associated increase in thermal loads represents a key design of hypersonic vehicles designed to fly at low altitudes. Despite the importance of information on this phenomena, there have been no known experimental studies to date to determine criteria for attachment line transition and the magnitude of transitional and turbulent attachment line heating at Mach numbers above 10. The purpose of the study conducted under the present contract was to determine transition criteria for sweep angles between 60 and 80 degrees and Mach numbers from 11 to 18. The program was highly successful and yielded measurements under these high Mach number, high Reynolds number conditions to define transition criteria for the onset of attachment line transition and the magnitude of the transitional and turbulent flows which subsequently develop.

The experimental studies were conducted in the Calspan 48-inch shock tunnel at Mach numbers between 11 and 18 and Reynolds numbers from 1×10^6 to 10×10^6 . A three-inch diameter cylindrical model instrumented along the attachment line, and around the circumference at a series of longitudinal stations, was used in the experimental program. High-frequency thin-film heat transfer instrumentation and piezoelectric pressure transducers were used to determine the mean and fluctuating characteristics of the heat transfer and pressure loading (See Figure 9). At its upstream end, the cylinder was configured either with a sharp leading edge or attached to a flat plate (as shown in Figure 10) to provide two basic upstream boundary conditions. For the sharp leading edge configuration, trips were also employed just downstream of the leading edge. Measurements were made for a range of sweep angles between 60 and 80 degrees varying the unit of the Reynolds number at freestream and boundary conditions at the leading edge. Transition was determined by observing the unsteady outputs of the thin-film heat transfer instrumentation. Turbulent 'bursts' were clearly evident when transition was present on the stagnation line (See Figure 11). The intermittent nature of the transition region was also observed as was the increase in heating between laminar and turbulent stagnation line boundary layers. An experimental program of 37 runs was conducted.

We are currently completing the analysis of this data and preparing a paper for publication in a forthcoming AIAA conference.



Model/Instrumentation

- 3-inch diameter cylinder of varying length from 23" to 35"
- 80 thin film heat transfer gages located along the 0° (stagnation) and $\pm 45^\circ$ at the circumferentially distributed about the cylinder from $\pm 45^\circ$ at the mid-span
- Various tip configurations to keep leeward side of cylinder tip parallel to freestream
- Two types of roughness elements, .015" and .030" grit located 2" downstream of tip in a 0.235" wide circumferential strip
- Tip end plate mounted parallel to freestream, with a running length of 4.73"

Figure 9 Swept Cylinder Model and Instrumentation

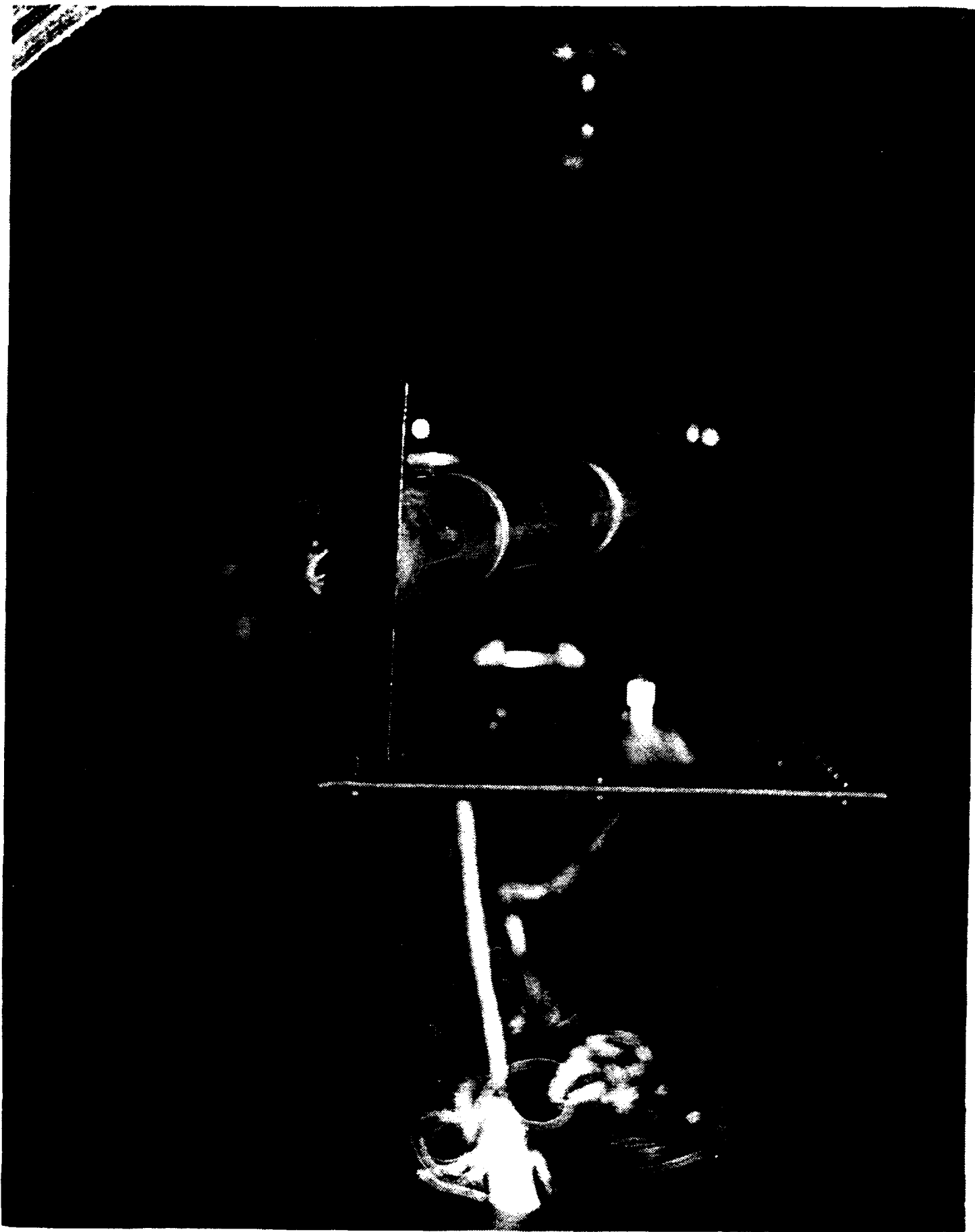
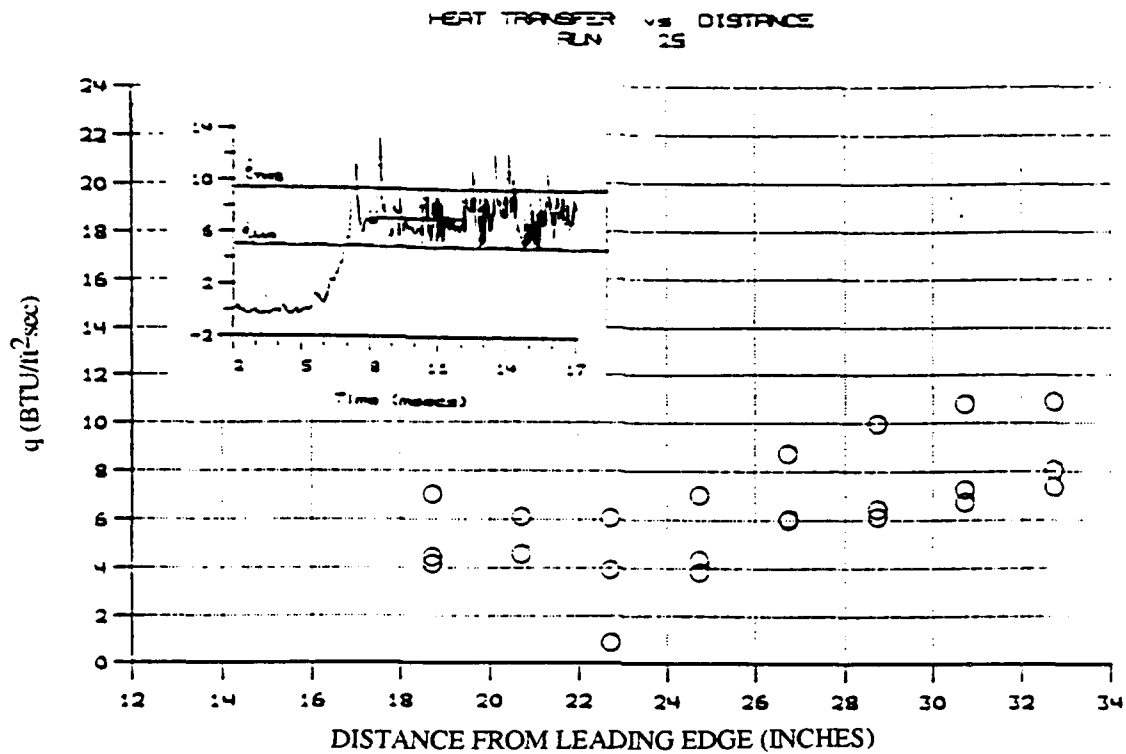


Figure 10 Steamwise View of Swept Cylinder Model with
Float Plate Attached 21



Parameters Varied in Study:

1. Freestream Mach Number
2. Cross Flow Reynolds Number

$$\bar{R}^* \equiv \sqrt{\frac{u_\infty^2}{v_* \left(\frac{\partial v_e}{\partial y} \right)_{y=0}}}$$

3. Sweep Angle
4. Boundary Layer Trips
 - a. Roughness elements
 - b. End plate (ramp)

Figure 11 Heat Transfer Measurements Transition Region on Swept Cylinder

2.5 Studies of Relaminarization in Strong Favorable Pressure Gradients

If the initial expansion from the Scramjet combustor into the nozzle entrance is severe, the strong favorable pressure gradient could lead to relaminarization. A laminar boundary layer on the nozzle would significantly effect the performance of the engine. Thus, it is of crucial importance to understand the conditions under which relaminarization occurs and the characteristics and extent of the laminar region. Surprisingly, there is almost no definitive experimental data to support relaminarization criteria at hypersonic speeds, nor are there any experimental measurements available to aid in the modeling of the subsequent retransitioning process. In the present series of studies, we attempted to define when relaminarization would occur and the length and characteristics of the region between relaminarization and transition.

A simple flat plate-expansion ramp model, shown in Figure 12, was used in this program. The length of the flat plate was selected to insure that there was a fully turbulent boundary layer in the upstream of the expansion region at all freestream conditions. The strength of the interaction was controlled by changing the angle between the flat plate and the second expansion surface. Both the flat plate and the expansion surface were fully instrumented with heat transfer and pressure gages, with a high density of instrumentation located just upstream and downstream of the expansion corner. The high frequency thin-film instrumentation enabled us to determine the position of transition of the flat plate and the fluctuating characteristics of the region in the expansion corner. The extent of the region of relaminarization was determined from mean distribution of the heat transfer rate as well as the heat fluctuations in this region. The distribution of heating rates over this model were examined for an extensive number of turning configurations and freestream unit Reynolds numbers. In all these studies, the Mach number on the flat plate was between 4 and 8, typical of the Mach number that would occur in the Scramjet combustor. We were unable to find a condition where the boundary layer was fully turbulent on the flat plate with some evidence of relaminarization downstream of the expansion corner for turning angles of less than 17 degrees. Figure 13 shows the distribution of heating rate over a model configuration with a 17.8 degree turning angle for a series of unit Reynolds numbers of the flow over the flat plate. We see that only for the largest unit Reynolds number, is there a significantly larger decrease in heat transfer rate in the expansion corner and a subsequent rise to a uniform turbulent level downstream of this process. Although there is a distinctive region in which the flow is not fully turbulent, the small extent of this region,

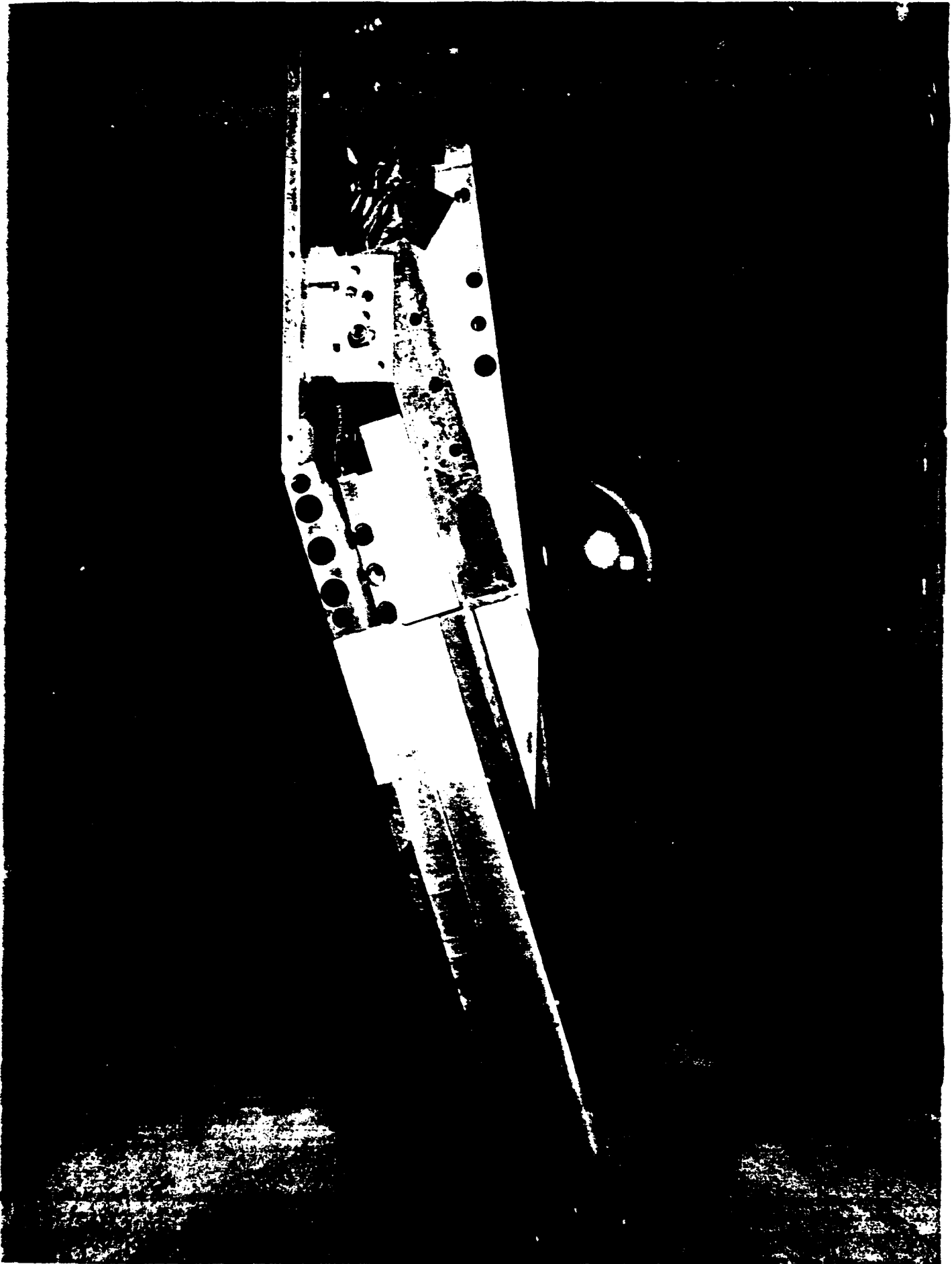


Figure 12 Flat Plate Expansion Surface Model used in Relaminarization Studies

Ch vs DISTANCE
beta = -17.80

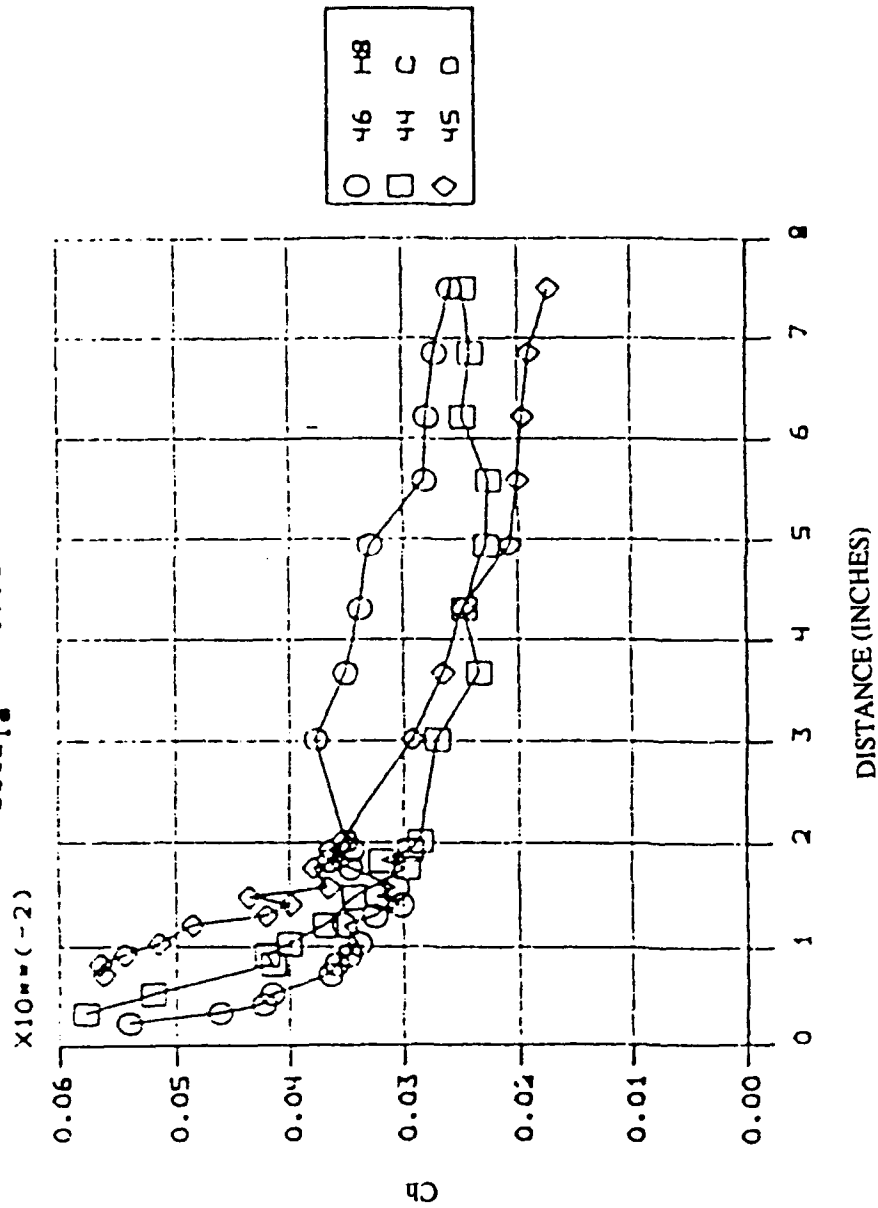


Figure 13 Distribution of Heating Rate in Turbulent and Relaminarizing Flow on Expansion Surface

coupled with the minimal decrease in heat transfer rate, even for the very large decrease in pressure in the expansion region, suggests that expectations of significant drag reduction associated with relaminarization may not be well-founded. Clearly, further experimental studies are required to establish the importance of relaminarization, particularly in combustor nozzle flows. Accurately defining the results of these experiments will prove difficult because of the distortions that are developed in the combustor as a result of injectors and burning.

2.6 Studies of 2D and 3D Crossing Shock Interaction With/Without Helium Film Cooling

A key technology in the development of SCRAMJET propulsion is associated with the active cooling of the walls of the inlet, combustor and nozzle of the engine. Here, the relative merits of film cooling must be evaluated against complications associated with the combustion of the coolant and the interaction between the coolant layer and shock waves generated by the compression ramp and the cowl, and induced by vectored injection or injector struts. However, while there is a significant body of information on film cooling, and regions of shock wave/boundary layer in supersonic and hypersonic flows, there is little information on the vertically-oriented swept shock wave/cooling layer interaction. For this reason a study has been developed to determine the effectiveness of film cooling in regions of swept shock wave/cooling layer interaction. We also seek to provide a detailed set of measurements to describe the key features of these flows against which to evaluate computational codes and turbulence modeling.

A flat plate film cooling model used in this study is shown in figures 14 and 15. A coolant reservoir system, located external to the model, supplied coolant to the internal passages in the model via fast acting Valcor valves. Once energized, the film coolant is injected tangential to the model surface from a series of Mach 2.7 nozzles located across the entire span of the model. The nozzle bank presented a backwards facing step to the flow, and its location relative to the leading edge was varied by using different length flat plates upstream. This gave variation in local Reynolds number and ensured a fully developed turbulent boundary layer existed upstream of the coolant injection point.

The surface of the flat plate upstream and downstream of the coolant injection points was densely instrumented with both high frequency thin film heat transfer gages and pressure transducers. The entire passage from coolant reservoir to coolant nozzle exit plane was instrumented to accurately determine the coolant flow rate and nozzle exit condition.

Vertical shock generators (fins) were fitted to the flat plate model to produce single and crossing swept shock/film coolant interactions. The size and location of the fins were designed such that the interaction occurred far enough downstream of the coolant nozzles so any upstream influence from the shock waves would be measured and bounded by the

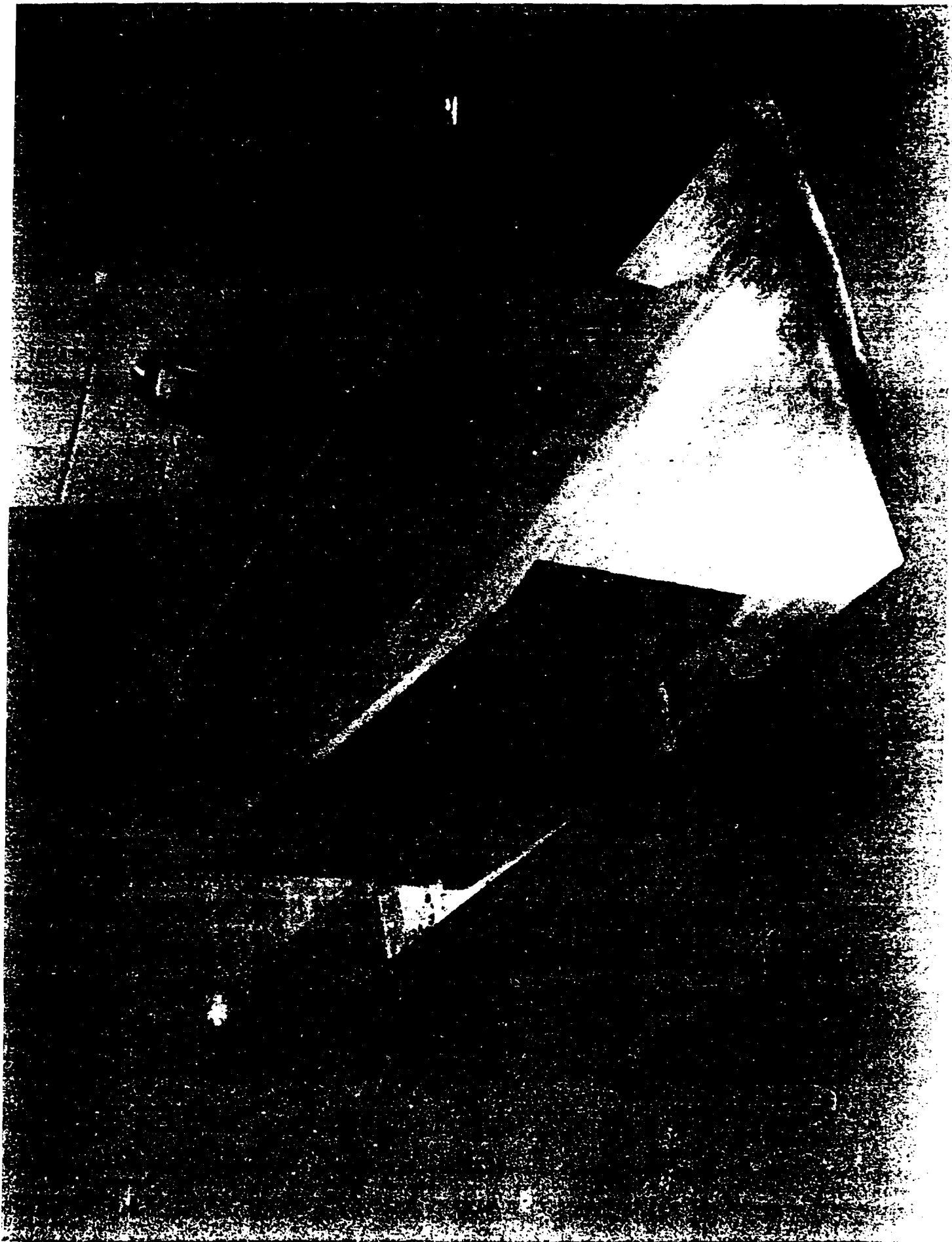
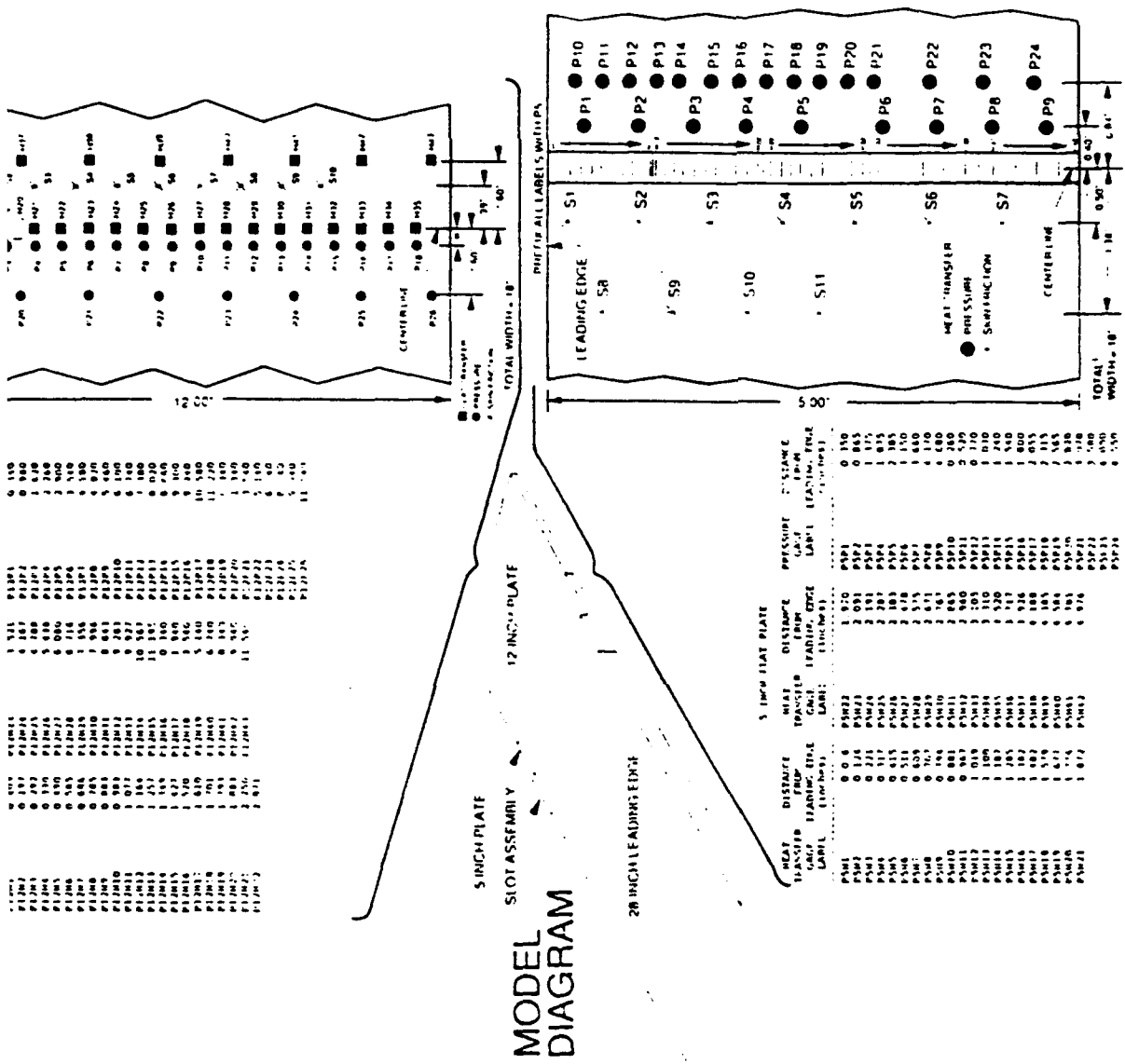


**Figure 14 Flat Plate Film Cooling Model with
Vertical Shock Generators Installed**



P100	P101	P102	P103	P104	P105	P106	P107	P108	P109	P110	P111	P112	P113	P114	P115	P116	P117	P118	P119	P120	P121	P122	P123	P124
0.100	0.101	0.102	0.103	0.104	0.105	0.106	0.107	0.108	0.109	0.110	0.111	0.112	0.113	0.114	0.115	0.116	0.117	0.118	0.119	0.120	0.121	0.122	0.123	0.124
0.130	0.131	0.132	0.133	0.134	0.135	0.136	0.137	0.138	0.139	0.140	0.141	0.142	0.143	0.144	0.145	0.146	0.147	0.148	0.149	0.150	0.151	0.152	0.153	0.154
0.160	0.161	0.162	0.163	0.164	0.165	0.166	0.167	0.168	0.169	0.170	0.171	0.172	0.173	0.174	0.175	0.176	0.177	0.178	0.179	0.180	0.181	0.182	0.183	0.184
0.190	0.191	0.192	0.193	0.194	0.195	0.196	0.197	0.198	0.199	0.200	0.201	0.202	0.203	0.204	0.205	0.206	0.207	0.208	0.209	0.210	0.211	0.212	0.213	0.214
0.220	0.221	0.222	0.223	0.224	0.225	0.226	0.227	0.228	0.229	0.230	0.231	0.232	0.233	0.234	0.235	0.236	0.237	0.238	0.239	0.240	0.241	0.242	0.243	0.244
0.250	0.251	0.252	0.253	0.254	0.255	0.256	0.257	0.258	0.259	0.260	0.261	0.262	0.263	0.264	0.265	0.266	0.267	0.268	0.269	0.270	0.271	0.272	0.273	0.274
0.280	0.281	0.282	0.283	0.284	0.285	0.286	0.287	0.288	0.289	0.290	0.291	0.292	0.293	0.294	0.295	0.296	0.297	0.298	0.299	0.300	0.301	0.302	0.303	0.304
0.310	0.311	0.312	0.313	0.314	0.315	0.316	0.317	0.318	0.319	0.320	0.321	0.322	0.323	0.324	0.325	0.326	0.327	0.328	0.329	0.330	0.331	0.332	0.333	0.334
0.340	0.341	0.342	0.343	0.344	0.345	0.346	0.347	0.348	0.349	0.350	0.351	0.352	0.353	0.354	0.355	0.356	0.357	0.358	0.359	0.360	0.361	0.362	0.363	0.364
0.370	0.371	0.372	0.373	0.374	0.375	0.376	0.377	0.378	0.379	0.380	0.381	0.382	0.383	0.384	0.385	0.386	0.387	0.388	0.389	0.390	0.391	0.392	0.393	0.394
0.400	0.401	0.402	0.403	0.404	0.405	0.406	0.407	0.408	0.409	0.410	0.411	0.412	0.413	0.414	0.415	0.416	0.417	0.418	0.419	0.420	0.421	0.422	0.423	0.424
0.430	0.431	0.432	0.433	0.434	0.435	0.436	0.437	0.438	0.439	0.440	0.441	0.442	0.443	0.444	0.445	0.446	0.447	0.448	0.449	0.450	0.451	0.452	0.453	0.454
0.460	0.461	0.462	0.463	0.464	0.465	0.466	0.467	0.468	0.469	0.470	0.471	0.472	0.473	0.474	0.475	0.476	0.477	0.478	0.479	0.480	0.481	0.482	0.483	0.484
0.490	0.491	0.492	0.493	0.494	0.495	0.496	0.497	0.498	0.499	0.500	0.501	0.502	0.503	0.504	0.505	0.506	0.507	0.508	0.509	0.510	0.511	0.512	0.513	0.514
0.520	0.521	0.522	0.523	0.524	0.525	0.526	0.527	0.528	0.529	0.530	0.531	0.532	0.533	0.534	0.535	0.536	0.537	0.538	0.539	0.540	0.541	0.542	0.543	0.544
0.550	0.551	0.552	0.553	0.554	0.555	0.556	0.557	0.558	0.559	0.560	0.561	0.562	0.563	0.564	0.565	0.566	0.567	0.568	0.569	0.570	0.571	0.572	0.573	0.574
0.580	0.581	0.582	0.583	0.584	0.585	0.586	0.587	0.588	0.589	0.590	0.591	0.592	0.593	0.594	0.595	0.596	0.597	0.598	0.599	0.600	0.601	0.602	0.603	0.604
0.610	0.611	0.612	0.613	0.614	0.615	0.616	0.617	0.618	0.619	0.620	0.621	0.622	0.623	0.624	0.625	0.626	0.627	0.628	0.629	0.630	0.631	0.632	0.633	0.634
0.640	0.641	0.642	0.643	0.644	0.645	0.646	0.647	0.648	0.649	0.650	0.651	0.652	0.653	0.654	0.655	0.656	0.657	0.658	0.659	0.660	0.661	0.662	0.663	0.664
0.670	0.671	0.672	0.673	0.674	0.675	0.676	0.677	0.678	0.679	0.680	0.681	0.682	0.683	0.684	0.685	0.686	0.687	0.688	0.689	0.690	0.691	0.692	0.693	0.694
0.700	0.701	0.702	0.703	0.704	0.705	0.706	0.707	0.708	0.709	0.710	0.711	0.712	0.713	0.714	0.715	0.716	0.717	0.718	0.719	0.720	0.721	0.722	0.723	0.724
0.730	0.731	0.732	0.733	0.734	0.735	0.736	0.737	0.738	0.739	0.740	0.741	0.742	0.743	0.744	0.745	0.746	0.747	0.748	0.749	0.750	0.751	0.752	0.753	0.754
0.760	0.761	0.762	0.763	0.764	0.765	0.766	0.767	0.768	0.769	0.770	0.771	0.772	0.773	0.774	0.775	0.776	0.777	0.778	0.779	0.780	0.781	0.782	0.783	0.784
0.790	0.791	0.792	0.793	0.794	0.795	0.796	0.797	0.798	0.799	0.800	0.801	0.802	0.803	0.804	0.805	0.806	0.807	0.808	0.809	0.810	0.811	0.812	0.813	0.814
0.820	0.821	0.822	0.823	0.824	0.825	0.826	0.827	0.828	0.829	0.830	0.831	0.832	0.833	0.834	0.835	0.836	0.837	0.838	0.839	0.840	0.841	0.842	0.843	0.844
0.850	0.851	0.852	0.853	0.854	0.855	0.856	0.857	0.858	0.859	0.860	0.861	0.862	0.863	0.864	0.865	0.866	0.867	0.868	0.869	0.870	0.871	0.872	0.873	0.874
0.880	0.881	0.882	0.883	0.884	0.885	0.886	0.887	0.888	0.889	0.890	0.891	0.892	0.893	0.894	0.895	0.896	0.897	0.898	0.899	0.900	0.901	0.902	0.903	0.904
0.910	0.911	0.912	0.913	0.914	0.915	0.916	0.917	0.918	0.919	0.920	0.921	0.922	0.923	0.924	0.925	0.926	0.927	0.928	0.929	0.930	0.931	0.932	0.933	0.934
0.940	0.941	0.942	0.943	0.944	0.945	0.946	0.947	0.948	0.949	0.950	0.951	0.952	0.953	0.954	0.955	0.956	0.957	0.958	0.959	0.960	0.961	0.962	0.963	0.964
0.970	0.971	0.972	0.973	0.974	0.975	0.976	0.977	0.978	0.979	0.980	0.981	0.982	0.983	0.984	0.985	0.986	0.987	0.988	0.989	0.990	0.991	0.992	0.993	0.994
0.995	0.996	0.997	0.998	0.999	1.000	1.001	1.002	1.003	1.004	1.005	1.006	1.007	1.008	1.009	1.010	1.011	1.012	1.013	1.014	1.015	1.016	1.017	1.018	1.019

HEAT TRANSFER GAUGE LABEL	DISTANCE LEADING EDGE (INCHES)	HEAT TRANSFER GAUGE LABEL	DISTANCE LEADING EDGE (INCHES)	PRESSURE GAUGE LABEL	DISTANCE LEADING EDGE (INCHES)
P501	0.10	P502	0.20	P503	0.30
P504	0.40	P505	0.50	P506	0.60
P507	0.70	P508	0.80	P509	0.90
P510	1.00	P511	1.10	P512	1.20
P513	1.30	P514	1.40	P515	1.50
P516	1.60	P517	1.70	P518	1.80
P519	1.90	P520	2.00	P521	2.10
P522	2.20	P523	2.30	P524	2.40
P525	2.50	P526	2.60	P527	2.70
P528	2.80	P529	2.90	P530	3.00
P531	3.10	P532	3.20	P533	3.30
P534	3.40	P535	3.50	P536	3.60
P537	3.70	P538	3.80	P539	3.90
P540	4.00	P541	4.10	P542	4.20
P543	4.30	P544	4.40	P545	4.50
P546	4.60	P547	4.70	P548	4.80
P549	4.90	P550	5.00	P551	5.10
P552	5.20	P553	5.30	P554	5.40
P555	5.50	P556	5.60	P557	5.70
P558	5.80	P559	5.90	P560	6.00
P561	6.10	P562	6.20	P563	6.30
P564	6.40	P565	6.50	P566	6.60
P567	6.70	P568	6.80	P569	6.90
P570	7.00	P571	7.10	P572	7.20
P573	7.30	P574	7.40	P575	7.50
P576	7.60	P577	7.70	P578	7.80
P579	7.90	P580	8.00	P581	8.10
P582	8.20	P583	8.30	P584	8.40
P585	8.50	P586	8.60	P587	8.70
P588	8.80	P589	8.90	P590	9.00
P591	9.10	P592	9.20	P593	9.30
P594	9.40	P595	9.50	P596	9.60
P597	9.70	P598	9.80	P599	9.90
P600	10.00	P601	10.10	P602	10.20
P603	10.30	P604	10.40	P605	10.50
P606	10.60	P607	10.70	P608	10.80
P609	10.90	P610	11.00	P611	11.10
P612	11.20	P613	11.30	P614	11.40
P615	11.50	P616	11.60	P617	11.70
P618	11.80	P619	11.90	P620	12.00
P621	12.10	P622	12.20	P623	12.30
P624	12.40	P625	12.50	P626	12.60
P627	12.70	P628	12.80	P629	12.90
P630	13.00	P631	13.10	P632	13.20
P633	13.30	P634	13.40	P635	13.50
P636	13.60	P637	13.70	P638	13.80
P639	13.90	P640	14.00	P641	14.10
P642	14.20	P643	14.30	P644	14.40
P645	14.50	P646	14.60	P647	14.70
P648	14.80	P649	14.90	P650	15.00
P651	15.10	P652	15.20	P653	15.30
P654	15.40	P655	15.50	P656	15.60
P657	15.70	P658	15.80	P659	15.90
P660	16.00	P661	16.10	P662	16.20
P663	16.30	P664	16.40	P665	16.50
P666	16.60	P667	16.70	P668	16.80
P669	16.90	P670	17.00	P671	17.10
P672	17.20	P673	17.30	P674	17.40
P675	17.50	P676	17.60	P677	17.70
P678	17.80	P679	17.90	P680	18.00
P681	18.10	P682	18.20	P683	18.30
P684	18.40	P685	18.50	P686	18.60
P687	18.70	P688	18.80	P689	18.90
P690	19.00	P691	19.10	P692	19.20
P693	19.30	P694	19.40	P695	19.50
P696	19.60	P697	19.70	P698	19.80
P699	19.90	P700	20.00	P701	20.10
P702	20.20	P703	20.30	P704	20.40
P705	20.50	P706	20.60	P707	20.70
P708</					

instrumentation. Care was taken so that the expansion off the trailing edge of the vertical fins did not interfere with the compression process in the instrumented area of the model.

Freestream tunnel conditions were selected to produce a Mach 8 flat plate air flow with a fully developed turbulent boundary layer existing well upstream of the coolant injection point, conditions typical in a Scramjet combustor. Shock strengths generated by the vertical fins followed side wall compressions commonly suggested for Scramjet geometries, varying from 5° , $7\text{-}1/2^\circ$, and 10° turning angle. Helium was chosen as the coolant to be tested, since it is representative of a low density, high specific heat coolant, such as hydrogen. The coolant flow rates were chosen such that the coolant nozzles operated in matched and under-expanded exit plane pressures.

The effectiveness of helium film cooling in this environment was investigated and a run matrix summary of the successfully completed runs is shown in Table II. The flat plate turbulent boundary layer, with no coolant flow, was interacted with varying strength swept shocks. The single and crossing shocks produced pressure and heat transfer rises on the flat plate model, and configurations were selected that produced attached and separated flows in the shock wave/boundary layer interaction region. Several tunnel runs were conducted at each fin configuration while varying the location of the interaction relative to the flat plate instrumentation. This approach will allow us to combine several runs to produce surface pressure and heat transfer "profiles" of the interaction region, parallel and perpendicular to the flat plate flow. These profiles quantify the distribution of the surface pressure and heat transfer enhancements that are generated for a given shock strength. Figure 16 gives an example of such profiles.

For each of these configurations, two different cooling rates, corresponding to matched and underexpanded coolant nozzle flows, were issued and the resulting surface heat transfer and pressure distributions were investigated. Again, each cooling rate/shock configuration was repeated to produce surface data "profiles".

The comparisons of various profiles showed that the addition of the relatively low momentum helium coolant to the interaction region caused flow separation to occur for weaker shocks than the no coolant flow configurations. This is critical since coolant flow separation enhances mixing, disabling the effectiveness of the film to provide thermal protection from the large heat transfer rates generated by the swept shocks. In instances when the flows did not separate, the heat transfer data shows that film coolant

Table 2 RUN MATRIX

37 runs successfully completed

MACH 8

Run	Local Reynolds No. @ Nozzle Exit Plane	Shock Generator Angle	Shock Type	Helium Coolant Exit Pressure Ratio Pc/Pe
2	4.0 (+7)	Flat Plate	None	0
4		7.5°	Single	
5		↓		
6		10°		
7		↓		
8		↓		
10		↓		
16		7.5°		
17		5°		
18		7.5°		
19	↓	5°		
20	4.3 (+7)	7.5°		
22		↓		
23		Flat Plate		
24		7.5°		
25		5°		
26		↓	↓	
27		7.5°	Double	
28		5°	↓	
29		7.5°		
30		↓		
31		↓		
32		↓		
33		↓	↓	
34		↓	Single	
35		↓	↓	↓
36		↓	↓	2
38		↓	↓	2
39		↓	↓	1
40		↓	↓	1
41		↓	Double	1
42		↓	↓	2
43		5°	↓	2
44		↓	↓	1
45		↓	Single	1
46		↓	↓	2

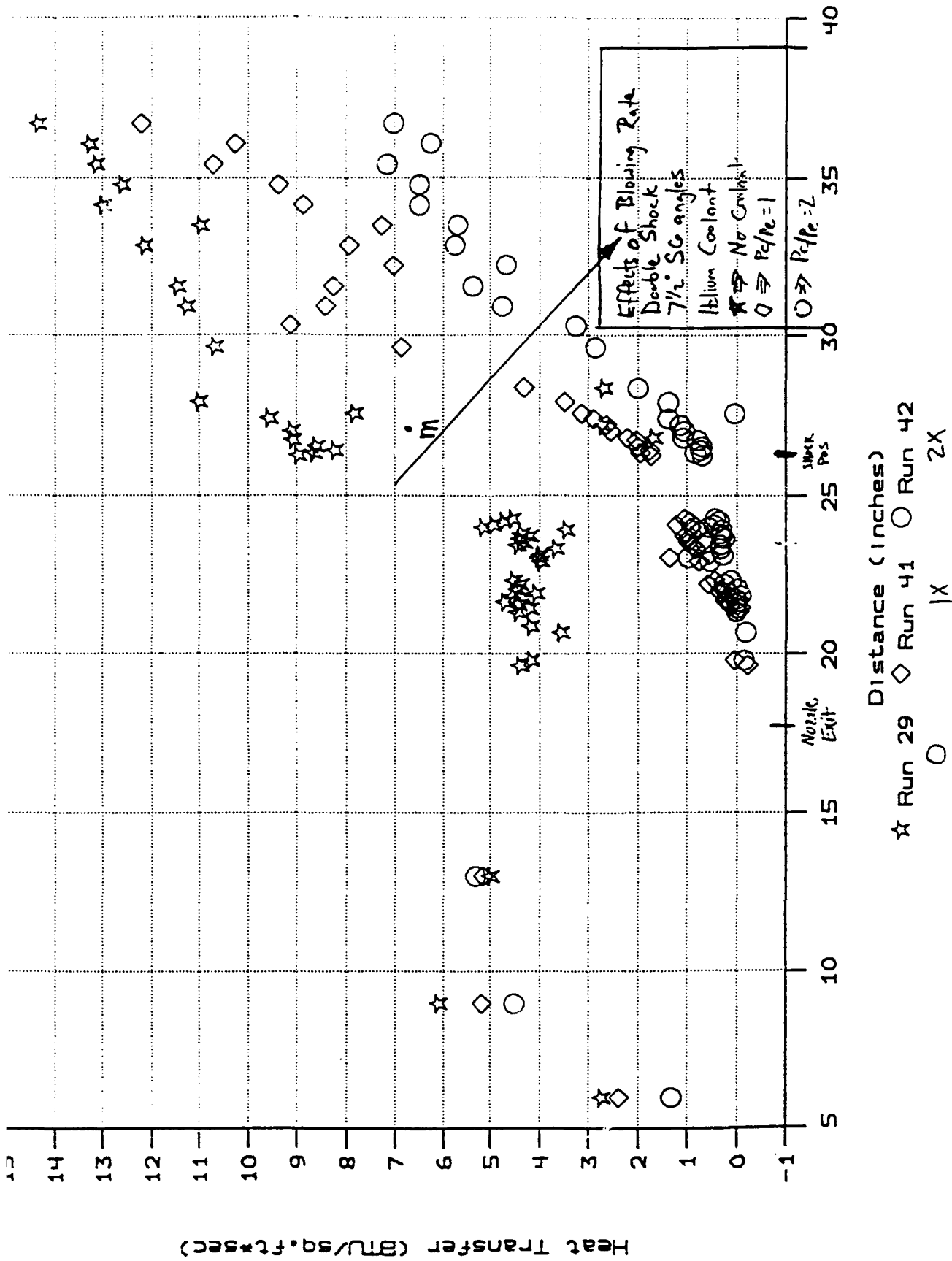


Figure 16 Heat Transfer distribution Profiles of Crossing Shock/Film Coolant Interaction

did not provide a significant reduction in the peak heat transfer for distances just downstream of the interaction.

The analysis of this data is currently ongoing, and results are being prepared for publication in an upcoming AIAA conference.

3. CONSTRUCTION OF A DATABASE OF MEASUREMENTS IN HYPERSONIC FLOW FOR CFD CODE VALIDATION

In this segment of the program, a detailed examination has been made of the experimental data collected on fundamental flow phenomena in laminar transitional and turbulent flows in programs supported by AFOSR during the past 25 years. On the basis of this detailed examination, an experimental database, selected and compiled from aerothermal measurements obtained on basic model configurations on which fundamental flow phenomena were obtained, has been generated.

The experimental studies were conducted in hypersonic flows in Calspan's 48-inch, 96-inch, and 6-foot shock tunnels during the past 25 years. The measurements selected for this database were assembled from a far larger set by choosing only the measurements in laminar, transitional, and turbulent flows, which we believe are of the greatest value for code validation. A special computer program, "CUBDAT," was constructed to provide easy access to the measurements in the database as well as the means to plot the measurements and compare them with imported data. The database contains tabulations of model configurations; freestream conditions; and measurements of heat transfer, pressure, and skin friction for each of the studies selected for inclusion. The measurements tabulated in this database are divided into seven main areas. The first segment contains measurements in laminar flow emphasizing shock wave-boundary layer interaction. In the second segment, we present measurements in transitional flows over flat plates and cones. The third segment comprises measurements in regions of shock wave/turbulent boundary layer interactions. Studies of the effects of surface roughness of nosetips and conical afterbodies are presented in the fourth segment of the database. Detailed measurements in regions of shock/shock boundary layer interaction are contained in the fifth segment. Measurements in regions of wall jet and transpiration cooling are presented in the final two segments.

This program represented a significant effort under the contract and provides a unique database with which to examine the computation of complex interacting viscous/inviscid interacting flowfields. A paper describing the database, AIAA 92-4023, A Database of Aerothermal Measurements in Hypersonic Flow for CFD Validation, was presented at the AIAA Ground Testing Symposium in Nashville. This paper is attached as Appendix 3.

APPENDIX 1

AIAA PAPER NO. 93-5005

**RECENT ADVANCES IN HYPERSONIC TEST FACILITIES
AND EXPERIMENTAL RESEARCH**



AIAA-93-5005

**Recent Advances in
Hypersonic Test Facilities and
Experimental Research**

M. Holden,
Calspan Corporation,
Buffalo, NY, USA

**AIAA/DGLR FIFTH INTERNATIONAL
AEROSPACE PLANES AND HYPERSONICS
TECHNOLOGIES CONFERENCE**
30 NOVEMBER - 3 DECEMBER 1993 / MUNICH, GERMANY

RECENT ADVANCES IN HYPERSONIC TEST FACILITIES AND EXPERIMENTAL RESEARCH*

Michael S. Holden**
Calspan Corporation
Buffalo, New York

Abstract

In this paper we review some key aerothermodynamic phenomena which must be understood and predicted in the design of advanced hypersonic interceptors and air-breathing vehicles. The facility requirements to perform these studies are briefly reviewed. Calibration and validation studies in the recently constructed Large Energy National Shock Tunnel (LENS) facility are presented. The application of this facility to study complex chemical and turbulent non-equilibrium flows is discussed. Recent experimental studies to examine important phenomena associated with boundary layer transition and relaminarization, transpiration cooling, and shock wave boundary layer interaction are presented.

1. INTRODUCTION

The development of new hypersonic vehicles will center about the capability to understand and predict a number of key complex aerothermodynamic phenomena. To develop such a capability will require computational and experimental research integrated more closely than in the past. The design of such experimental programs, and the measurements made in them, will require detailed pre- and post-test predictions. The post-test analysis of the experimental measurements and their integration into the detailed modeling employed within the codes will also require an intrinsically more sophisticated coupling between experimenter and code developer. Currently, there are three major program areas where the ability to predict complex aerothermodynamic phenomena are crucial to the development of a successful design. The first is the development of hypersonic interceptors designed to maneuver and seek targets through highly distorted shock layer flows for velocities of up to 5 km/sec. The second is the development of hypersonic air-breathing vehicles designed to cruise at Mach numbers between 6 to 10, or scramjet/rocket propulsion systems designed to accelerate vehicles into orbit. Finally, there is continuing interest in the design of shuttle-like vehicles and interplanetary probes designed to travel at orbital and super-orbital velocities at relatively high altitudes. In Figure 1 we show the configurations and requirements for hypersonic interceptors and air-breathing vehicles. Although these systems have individual problems, the key phenomena which must be understood in developing both the interceptor and air-breathing vehicles are associated with the transitional and

turbulent hypersonic boundary layer in strong pressure gradients and flows where flowfield and combustion chemistry are important phenomena. In the high altitude regime, which is important to all three systems, we are required to understand and predict shock layer chemistry and gas surface interaction effects in order to design a stable and effective system, and predict the propagation of information through the shock layer.

Table I lists key phenomena in each hypersonic flow regime and their importance to vehicle design. In the high-altitude regime, with velocities large enough to fully dissociate the shock layer, flowfield and surface chemistry, and radiation effects, are of key importance. Here, even with the advanced DMSC codes currently available, we require detailed experimental information in high-temperature flows to define gas chemistry associated with dissociation and the phenomenology associated with gas surface interaction. Without such information, we will be unable to accurately predict the electromagnetic propagation through the shock layer as well as vehicle heating and stability at super-orbital velocities. At lower altitudes, where transition from laminar to turbulent flow is experienced, experimental information is required to assist in the development of models of the onset of transition and the structure of the transitional flow which follows. In these flows, the influence of chemical nonequilibrium on transitional characteristics remain to be quantified. In fully turbulent hypersonic flows, compressibility, turbulent mixing and combustion, flow separation, and real gas chemistry are the key phenomena which must be understood and described in order to successfully design scramjet engines; and effective seekerheads and divert thrusters on hypervelocity interceptors. A critical element in the successful pursuit of these objectives is the development of advanced hypervelocity facilities designed to operate at extremely high energy and pressure levels, and produce high-quality, well-defined flows.

In this paper, we briefly review the design, construction and calibration of the LENS facility (Reference 1) designed to develop high-quality hypersonic flows at velocities up to 5 km/sec for altitudes down to 30 km. The aerothermal and aero-optical instrumentation, which is being developed to provide key information for tunnel performance and interceptor and air-breathing vehicle design, is briefly reviewed. Experiments designed to validate and compare the performance of LENS with blow-down tunnels having

* This paper is declared a work of the U.S. Government and is not subject to copyright protection in the United States.

** Research Fellow; Associate Fellow, AIAA

longer flow duration are described. We then briefly review a series of experiments conducted to investigate key phenomena which must be modeled in advanced Navier Stokes codes.

2. CALIBRATION AND VALIDATION STUDIES IN THE LENS FACILITY

2.1 Description of the LENS Facility

The LENS facility is a conventional reflected shock tunnel whose design is based on principles established during the past 30 years of shock tunnel operation at Calspan. This shock tunnel was initially conceived in 1986 to provide a high-quality, long test duration flow, in which to examine fluid dynamic problems associated with complex turbulent interacting flows at high Reynolds numbers and Mach numbers. Initially, our objective was to design a facility to operate at high pressures but low-enthalpy levels, in which fully turbulent flows at Mach numbers between 6 and 14 could be generated, with test durations of up to 20 milliseconds, to study complex regions of separated turbulent flow and turbulent base flows. With the emergence of the NASP program, the design of the LENS facility was upgraded to provide Reynolds number duplication at Mach numbers from 6 to 15 (See Figure 2). The additional objective, to generate the high-enthalpy and pressure levels necessary to study scramjet combustion up to Mach number 15, necessitated the redesign of the driver for hydrogen operation. Finally, in its role as a major test facility to evaluate and develop the aerothermal and aero-optic characteristics of hypersonic interceptors, the design of the LENS facility was refined to upgrade its low-altitude performance and provide a measurement capability to accurately measure the aero-optic distortions which can occur over a seekerhead.

A schematic diagram of the LENS facility is shown in Figure 3. In this facility, the driver is connected to the driven tube through a double diaphragm assembly which enables the flow to be initiated with accuracy. A centerbody valve is installed between the driven tube and the nozzle assembly to terminate the flow through the nozzle after the steady test flow. In this way, we can minimize throat heating and particle damage to the model in the test section. The nozzle has a exit diameter of 48 in. enabling models of up to 4 ft in length to be tested. These models are mounted in the test section on a specially designed inertial isolation platform to minimize acceleration loads and model movement during the steady test time. The large driver volume necessitates the use of a large ballast tank attached to the test section to prevent overpressurizing the schlieren windows in the event of a centerbody failure. A wave diagram of the LENS facility operating under tailored interface conditions is compared with the operation of a free-piston shock tunnel in Figure 4. Although employing a large driver tube with

the conventional driver configuration necessitates the use of a large amount of driver gas relative to the free-piston shock tunnel, it has the advantage that the flow through the tunnel can be accurately initiated with a double diaphragm valve. Also, because it is extremely difficult to develop a wave-free flow in the compression tube of a piston-driven tunnel, the fluctuation levels in the reservoir and the resulting freestream are far steadier in the conventionally driven shock tunnel - a significant factor in the studies of transitional flows and turbulent mixing with combustion.

The LENS facility was designed for pressure levels in the driver and driven tubes of up to 30,000 psi. Three nozzles will be available for this facility covering the Mach number range from 6 to 18. The velocity-altitude performance of the LENS facility is plotted in Figure 5 together with a band of typical trajectories for air-breathing hypersonic vehicles. Figure 6 shows how the LENS facility is capable of duplicating the conditions required for combustion testing up to Mach 12 and generating conditions in a "direct-connect mode" which will enable duplication of conditions in hypersonic scramjet combustors to be obtained up to Mach 15. Figure 7 shows that the velocity-altitude capability of the LENS facility duplicates the freestream requirements of the major interceptor programs currently being considered in the U.S.

2.2 Measurements in Calibration and Validation Studies

Surface and Flowfield Instrumentation

A summary of the surface and flowfield instrumentation which is being assembled for use in the LENS facility is shown in Table II. The surface instrumentation which are now routinely used in the LENS facility have been developed over the past 30 years of shock tunnel operation. Thin film, calorimeter and coaxial heat transfer instrumentation are used to obtain heat transfer rates from .01 to 10,000 BTU/sec. The thin-film instrumentation, which has a frequency response of 1 MHz, has been used extensively in investigating the unsteady nature of transitional and turbulent separated flows. The calorimeter instrumentation has been used to obtain measurements on rough surfaces, and the coaxial heat transfer gages have been used to measure high heat transfer rates under high enthalpy where flow abrasion can become important. Both piezoelectric and strain gage instrumentation have been used to obtain high-frequency pressure measurements. Piezoelectric PCB transducers, which are sensitive to heating, have generally been used beneath orifices where as the Kulite strain gage transducers are mounted flush with the surface. In laminar flows we have employed skin friction transducers, based on a miniaturized single component force balance compensated for both acceleration and normal pressure, with success. Gas cap radiation and flush mounted

electro-static probes have been used to obtain radiation and electron density measurements respectively in highly-ionized nonequilibrium flows.

We routinely employ miniature pitot pressure, total temperature and thin-film instrumentation to obtain measurements to characterize the freestream and boundary layers about flows with velocities less than 8,000 ft/sec. We have generally employed miniature strain gage pressure transducers in the pitot probes, platinum-rhodium thermocouples in the total temperature probes, and thin-film instrumentation in the fluctuation probes. In high-temperature ionized flows, ion or Langmuir probes have been used to obtain measurements of electron density. We are employing a number of non-intrusive flowfield measurement techniques to determine properties in the freestream and around models in high-temperature flows. We have used interferometry and electron beam measurements to determine freestream and flowfield density. Electron beam techniques have also been used to obtain static-temperature measurements and density-fluctuation measurements. More recently, laser induced fluorescence (LIF) has been used successfully in shock tunnel studies to measure flowfield studies. Absorption spectroscopy is currently being developed to measure species concentrations in the LENS facility.

A sophisticated instrumentation set is being used to obtain non-intrusive measurements of the aero-optic disturbances generated in the flowfield over interceptor seekerheads. Refractive and radiative instrumentation is being developed to provide quantitative measurements of the distortion of electromagnetic waves through the shock layer and the radiation emitted from the near flowfield. A visible and infrared imagery system is also being developed to quantify the integrated effects of flowfield distortion on seekerhead characteristics. This instrumentation is described in more detail in Reference 2.

Calibration Studies

The conditions for which measurements of the performance of the LENS facility have been obtained or will be obtained in the near future are shown in Figure 8. The facility is being calibrated at velocities down to 5,000 ft/sec in order to support the comparison studies with measurements made on identical models in AEDC and NSWC. Calibrations are being obtained at 2, 3, and 4 km/sec for a range of altitudes in support of the interceptor programs. Detailed flowfield surveys, including measurements determining the chemical composition of the flow, will be obtained from 3 to 5 km/sec to define the flow environment for combustor testing. Flow survey measurements at all of the key test conditions will be compared with computations using Navier Stokes codes employing real gas chemistry and chemical nonequilibrium where important. A typical comparison made during calibration studies of the D-

nozzle in preparation for validation studies with the HEDI configuration are shown in Figure 9. As can be seen, the theory is in reasonably good agreement with experiment, and it is clear that real gas effects must be correctly included when running at these high pressure conditions.

Validation Studies

During this continuing phase of the program, flowfield and surface measurements are being obtained on model configurations duplicating or representative of seekerhead configurations to be tested later in the LENS facility. Of particular interest, are measurements on configurations tested in other facilities. The HEDI configuration is such an example where measurements have been obtained previously at AEDC and NSWC. Flight test measurements were also obtained on this test configuration. In our shock tunnel studies with the HEDI configuration, we obtained surface and flowfield measurements for direct comparison with earlier studies conducted at NSWC. Our objectives were to compare with the NSWC surface and flowfield measurements made under similar freestream conditions and at the same time determine whether there were any significant flow establishment problems in the shock tunnel. The use of the HEDI configuration to explore flow establishment problems was particularly stressing because of the large scale of the model and the very large blowing rates which were employed to cool the windows. Measurements were obtained on the HEDI configuration (See Figure 10) oriented at 0 and 5 degrees incident to the freestream. Comparisons between the heat transfer measurements in the LENS facility and those at NSWC, without window cooling are shown in Figure 11 for 0 degrees incidence. The two sets of centerline measurements can be seen to be in excellent agreement. The measurements in the LENS study also identify a significant variation across the uncooled HEDI window.

Flowfield surveys were obtained with rake assemblies containing high frequency pitot pressure and total temperature gages in both the LENS and NSWC studies. Comparisons between the total temperature and pitot temperature surveys at the mid-window station are shown in Figure 12. It can be seen that the measurements from the two facilities are in excellent agreement. We also observed in the shock tunnel studies that the flow establishment at the highest blowing rates, where extensive separation was observed over the forebody, was less than 2 milliseconds. The agreement between both the surface and flowfield measurements from these facilities is excellent. This agreement is somewhat surprising because of potential differences which might arise in the position transition in the HEDI configuration as a result of potential differences in the freestream noise environment.

3. RECENT STUDIES OF AEROTHERMAL PHENOMENA ASSOCIATED WITH ADVANCED HYPERSONIC VEHICLES

3.1 Introduction

In order to successfully design air-breathing hypersonic vehicles, it is necessary to develop accurate models of key fluid dynamic and thermodynamic processes which are used in the DMSC or Navier Stokes codes. At Mach numbers above 8, the length and structure of the boundary layer transition region can play an important role in determining the boundary layer flow entering the combustion chamber, and in turn the efficiency of the engine. There is little or no information on how the adverse pressure gradient developed on the curved compression ramp, decreases the length of the transition region and controls the development of the turbulent scales, which in turn influences the overshoot of heat transfer at the end of the transition process. The large aerothermal loads generated in a scramjet combustor at free stream Mach numbers above 10 make it necessary to employ an active cooling system to protect the combustor walls. Our studies of film cooling demonstrated that, in regions of shock impingement, film effectiveness can be significantly degraded. Transpiration cooling has been shown to be a very effective technique in hypersonic flow, however, because this technique intrinsically introduces a low momentum layer close to the surface, shock impingement could induce large separated regions and destroy cooling effectiveness. The large expansions which occur as the flow exits the combustor into the nozzle could give rise to relaminarization. Although relaminarization has been observed in supersonic flows and on noseups in hypersonic flow, there is little evidence the relaminarization could play a significant role in scramjet propulsion. In the remainder of this paper, we review the results of preliminary studies to obtain definitive measurements in transitional flows over curved inlets, transpiration-cooled flows with shock impingement, and relaminarizing flows in regions of strong expansion.

3.2 Transitional Flows Over Curved Compression Surfaces

In these studies, we examined transitional flows over a curved compression ramp at Mach numbers of 10, 11 and 12, over a range of Reynolds numbers to place the beginning of transition at various stations along the ramp. Here the objective was to examine how the length of the transition region, and the distribution of heat transfer within it, was influenced by the position of the transition onset in the pressure gradient, and the local Mach number. The principal instrumentation employed in this study were platinum thin-film gages because their high frequency response enabled us to determine the onset of transition, the development and convection of gross unsteadiness,

and the end of transitional flow. The compression ramp used in this study, shown in Figure 13, was constructed with an initial constant angle ramp, followed by a curved section terminated in a second constant angle ramp section. The centerline of the ramp was extensively instrumented with thin-film instrumentation in the regions of interest, and pressure instrumentation was positioned to accurately determine the pressure gradients along the ramp.

Measurements were made for a series of Reynolds numbers at each of the three Mach number conditions. The unit Reynolds number of the freestream was varied to place transition at various points along the ramp. Figure 14 shows the distributions of heating along the compression ramp for a series of unit Reynolds numbers at a Mach number of 11. Also shown on this plot are the corresponding pressure distributions. It can be seen from the pressure data that there is little influence of boundary layer characteristics on the pressure distributions along the model. Pressure measurements also show that the curve compression ramp begins at 10 inches from the leading edge and extends to 21 inches from the leading edge. The small variation in pressure just downstream of the curve ramp results from the coalition of the compression waves and associated reflective wave structure. For the highest Reynolds number, transition begins on the initial ramp and is completed approximately half way along the curved compression surface. At this point, the heating continues to increase along the surface because of the increase in the pressure level. At the lowest Reynolds number, transition begins several inches downstream of the beginning of the curved section, continues along the entire curved section, and is completed on the third segment of the compression surface. Here we see that there is a significant overshoot in the heat transfer rate which reflects the generation of large scale instabilities. At the intermediate Reynolds number, which was selected to position transition at the beginning of the curve compression ramp, transition was completed just ahead of the end of the curve compression ramp with a measurable overshoot in the heating level. These measurements demonstrated that the length of the transition region can be shortened significantly by an adverse pressure gradient. In the current studies where both mean and fluctuation measurements were available, we observed that although the mean heat transfer distributions continue to rise downstream at the end of transition on the curved section, the distinctive nature of the rise and overshoot in the transition region can be used to determine the extent of transition if fluctuation measurements are not available.

3.3 Shock Impingement Effects on Transpiration Cooled Surface

Effective methods to actively cool the walls of a scramjet combustor represent one of the most important

areas of engine research. Although film cooling has been shown to be an effective method in the absence of flow disturbances, earlier studies have shown that the film can be easily removed in regions of shock impingement. In general, transpiration cooling has been found to be more effective than film cooling, however, because of the low momentum wall region introduced by this technique, concern has been expressed as to its viability in regions of flow disturbances. In this experimental study, measurements were first made to examine the effectiveness of transpiration cooling for both helium and nitrogen coolants in the absence of external disturbances. We then conducted studies to examine the effect of shock impingement on the size and distribution of properties over these transpiration cooled surfaces. Measurements were made of the effectiveness of transpiration cooling of Mach numbers of 6 and 8 for flows where the boundary layers were fully-turbulent well upstream of the beginning of transpiration cooling. Both helium and nitrogen coolants were employed in the studies, and the flow rates were varied up to a level that increased blowing rates which had little further effect on cooling effectiveness. The model used in the experimental studies is shown in Figure 15. Miniature thin-film heat transfer gages were embedded in the transpiration cooled surface between the injection ports, and Kulite pressure gages were also installed in a manner so as not to influence the porous surface. Figure 16 shows the distribution of heating downstream of the beginning of transpiration cooling, with a helium coolant, for a range of blowing rates from 0 to 2 percent of the freestream mass flow rate. We observe that at the largest flow rates, the heating levels have dropped to less than 5 percent of their original level and the boundary layer is beginning to be blown from the surface. In Figure 17, we show the effects of shock impingement on the heating level for the same freestream conditions and a helium coolant. We see that in the absence of coolant, the heat transfer rate downstream of shock impingement, for a total flow turning angle of 14 degrees, is close to 10 times the initial turbulent value. Introducing coolant in and downstream of the region of shock impingement progressively reduces this level. For a 5 percent mass addition factor, we can reduce the heating downstream of shock impingement to the level of heating in the uncooled flow upstream of shock impingement. What is particularly surprising, is that the upstream influence of the shock impingement region is not significantly altered when transpiration cooling is introduced. In fact in these flows, transpiration cooling acts to further decrease the heating rate upstream of shock impingement. Further measurements, for a range of shock impingement strengths up to turning angles of 20 degrees, indicated that shock impingement on transpiration cooled surfaces did not induce significant distortions to the flowfield upstream or downstream of the impingement point; and the heat transfer could easily be reduced to pre-impingement levels with relatively small levels of mass addition. A remaining key question is, if hydrogen were

used as a coolant in the attached flow downstream of shock impingement, would it burn to the wall rendering transpiration cooling ineffective?

3.4 Studies of Relaminarization in Strong Adverse Pressure Gradients

If the initial expansion from the scramjet combustor into the nozzle entrance is severe, the strong favorable pressure gradient could lead to relaminarization. A laminar boundary layer on the nozzle would significantly effect the performance of the engine. Thus, it is of crucial importance to understand the conditions under which relaminarization occurs and the characteristics and extent of the laminar region. Surprisingly, there is almost no definitive experimental data to support relaminarization criteria at hypersonic speeds, nor are there any experimental measurements available to aid in the modeling of the subsequent retransitioning process. In the present series of studies, we attempted to define when relaminarization would occur and the length and characteristics of the region between relaminarization and transition. A simple flat plate-expansion ramp model, shown in Figure 18, was used in this program. The length of the flat plate was selected to insure that there was a fully turbulent boundary layer in the upstream of the expansion region at all freestream conditions. The strength of the interaction was controlled by changing the angle between the flat plate and the second expansion surface. Both the flat plate and the expansion surface were fully instrumented with heat transfer and pressure gages, with a high density of instrumentation located just upstream and downstream of the expansion corner. The high frequency thin-film instrumentation enabled us to determine the position of transition of the flat plate and the fluctuating characteristics of the region in the expansion corner. The extent of the region of relaminarization was determined from mean distribution of the heat transfer rate as well as the heat fluctuations in this region. The distribution of heating rates over this model were examined for an extensive number of turning configurations and freestream unit Reynolds numbers. In all these studies, the Mach number on the flat plate was between 4 and 8, typical of the Mach number that would occur in the scramjet combustor. We were unable to find a condition where the boundary layer was fully turbulent on the flat plate with some evidence of relaminarization downstream of the expansion corner for turning angles of less than 17 degrees. Figure 19 shows the distribution of heating rate over a model configuration with a 17.8 degree turning angle for a series of unit Reynolds numbers of the flow over the flat plate. We see that only for the largest unit Reynolds number, is there a significantly larger decrease in heat transfer rate in the expansion corner and a subsequent rise to a uniform turbulent level downstream of this process. Although there is a distinctive region in which the flow is not fully turbulent, the small extent of

this region, coupled with the minimal decrease in heat transfer rate, even for the very large decrease in pressure in the expansion region, suggests that expectations of significant drag reduction associated with relaminarization may not be well-founded. Clearly, further experimental studies are required to establish the importance of relaminarization, particularly in combustor nozzle flows. Accurately defining the results of these experiments will prove difficult because of the distortions that are developed in the combustor as a result of injectors and burning.

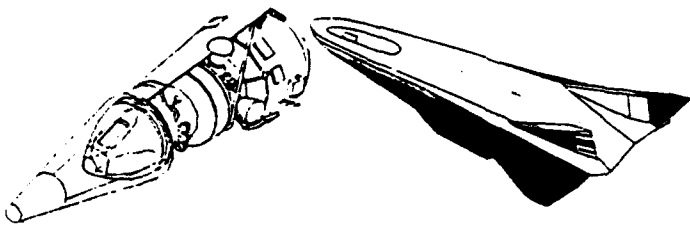
4. CONCLUSIONS

The effective design of advanced hypersonic interceptors and air-breathing vehicles requires a knowledge of key aerothermal phenomena associated with transitional flows, regions of turbulent mixing and combustion, and real gas chemistry. To advance the state of knowledge in these areas, new hypervelocity facilities must be developed to provide experimental information to be used to develop and evaluate detailed flow modeling used in the DMSC and Navier Stokes codes. The CUBRC LENS facility represents an important addition to the experimental facilities which can be used to examine turbulent reacting hypersonic flows at velocities from 6,000 to 15,000 ft/sec. Calibration and validation studies conducted in this facility are presented. Experimental studies to examine important phenomena associated with boundary layer transition and relaminarization, transpiration cooling, and shock wave boundary layer interaction have been reviewed.

References

1. Large Energy National Shock Tunnel (LENS) Description and Capabilities, Calspan-UB Research Center, February 1991.
2. "Calibration and Validation Studies in the LENS Facility," AIAA-93-2683, M. Holden, Calspan Corporation, J. Craig, STRATONICS, A. Ratliff & G. Sutton, Aero Thermo Technology, Presented at 2nd Annual AIAA SDIO Interceptor Technology Conference, June 6-9, 1993, Albuquerque, NM.

MISSIONS FOR NEW HYPERSONIC VEHICLES



HYPERSONIC INTERCEPTORS	AIR-BREATHING HYPERSONIC VEHICLES
• Endo-Interceptors* (Mach 4-14)	• Mach 6 Reconnaissance (Popular Mechanics)
• Exo-Interceptors* (Mach 6-16)	• Mach 6 Transport?
• Hypervelocity Interceptors* (Mach 20)	• Mach 6-13 Launchers for two stage to orbit
• Ramjet-Scramjet Powered, Long Range (> 200 miles) Interceptors	• NASP's SSTO *Rocket Powered

Fig. 1 Configuration and requirements for hypersonic interceptors and air-breathing vehicles.

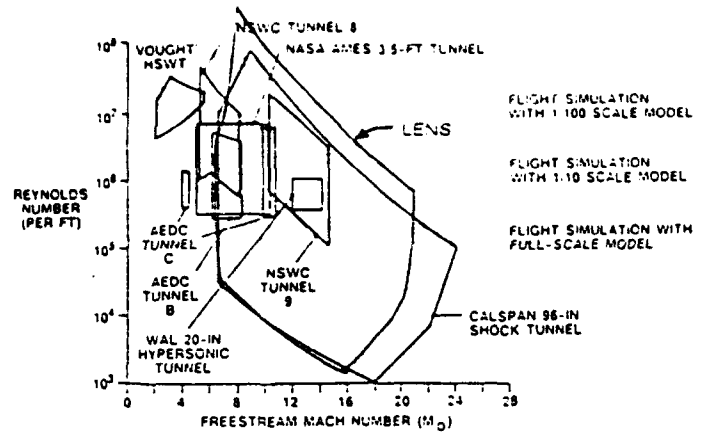


Fig. 2 Mach number/Reynolds number performance of LENS facility.

Table 1. Key phenomenology in hypersonic flow regimes.

FLOW REGIME	PHENOMENA	IMPORTANCE
Free molecular and Laminar Nonequilibrium Hypervelocity Flows	Shock Layer/Boundary Layer Chemistry and Radiation Effects	Optical Windows and "Red-Out" Prediction
	Flowfield Chemistry and Surface Catalysis	Vehicle Stability and Heating
	Gas/Surface Interaction	Re-Entry Body Drag and Stability
Boundary Layer Transition and Relaminarization	Nosetip and Forebody Transition in Favorable and Adverse Pressure Gradients	Nosetip and Forebody Design and Inlet Aerodynamics
	Attachment Line Transition	Attachment Line Heating Shock/Shock Interaction Heating
	Shear Layer Transition	Scramjet Nozzle Design
	Relaminarization	
HYPERSONIC TURBULENT FLOWS	Turbulent Nonequilibrium and Compressibility Effects	Scramjet Engine Design
	Shock/Boundary Layer Interaction	Control Surface Performance
	Jet Interaction	Combustor Performance
	Turbulent Mixing and Combustion	Seeker Head Performance
	Film & Transpiration Cooling	

Large Energy National Shock Tunnel (LENS)

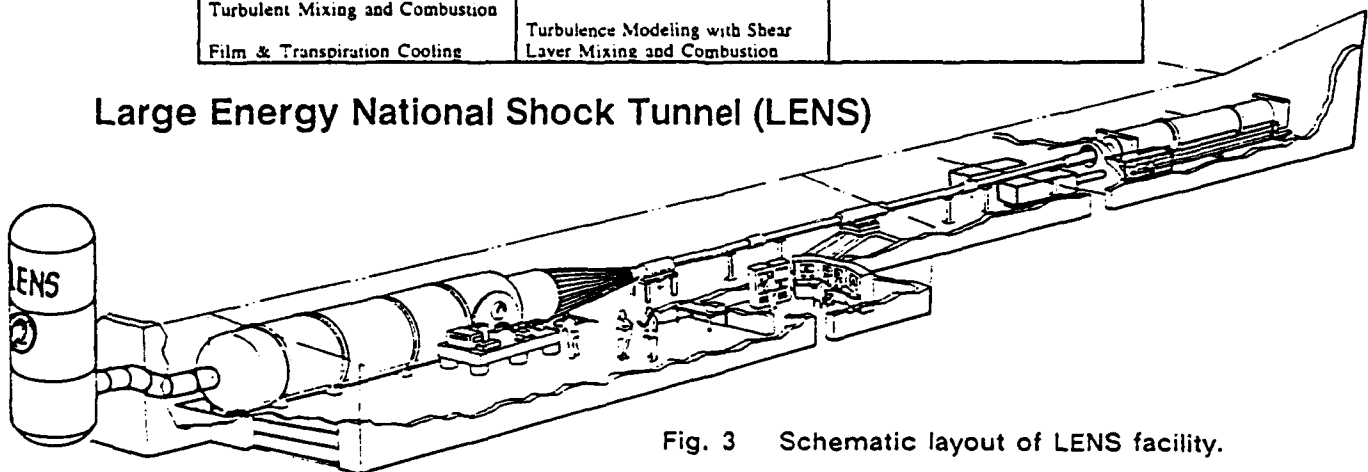


Fig. 3 Schematic layout of LENS facility.

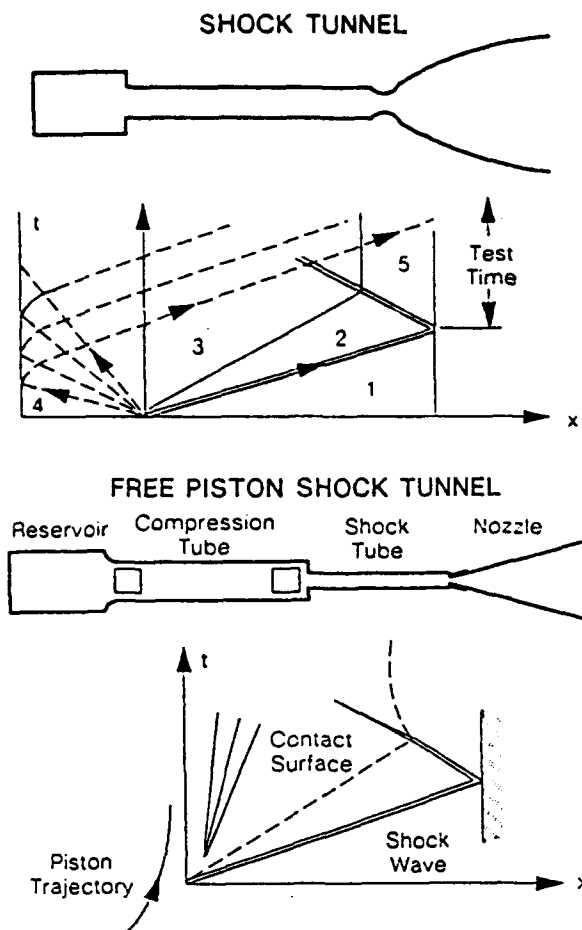


Fig. 4 Wave diagrams for conventional and free-piston reflected shock tunnels.

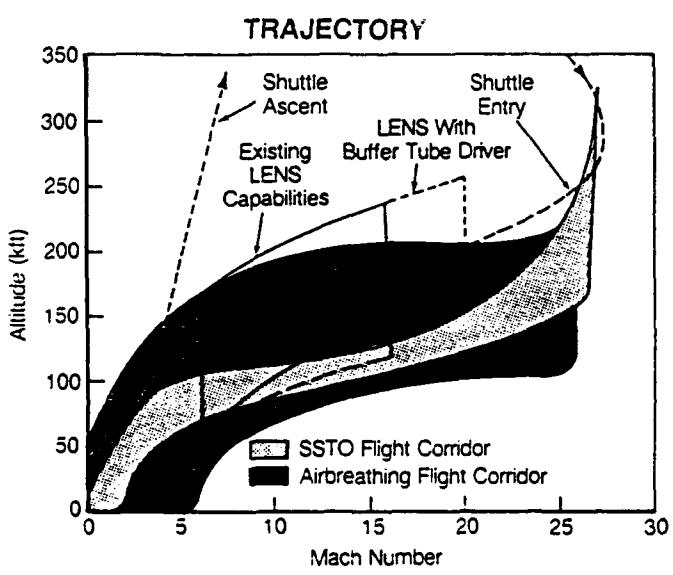


Fig. 5 LENS capabilities to perform studies for air-breathing hypersonic vehicles.

SIMULATION REQUIREMENTS FOR GROUND TESTING

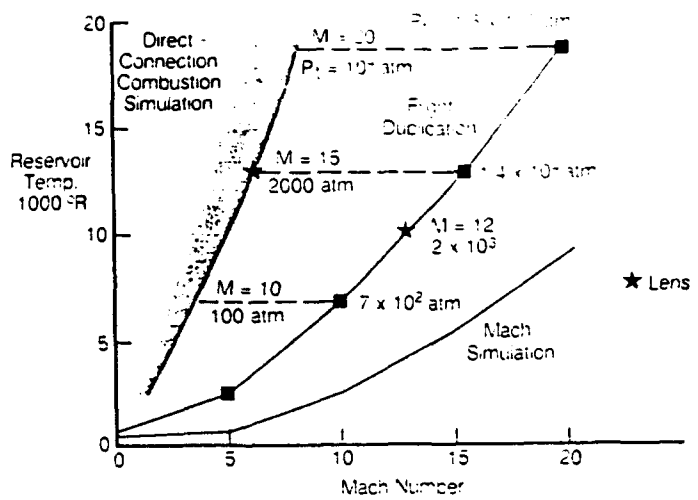


Fig. 6 Capabilities of LENS facility to perform combustor studies at Mach numbers from 8 to 15.

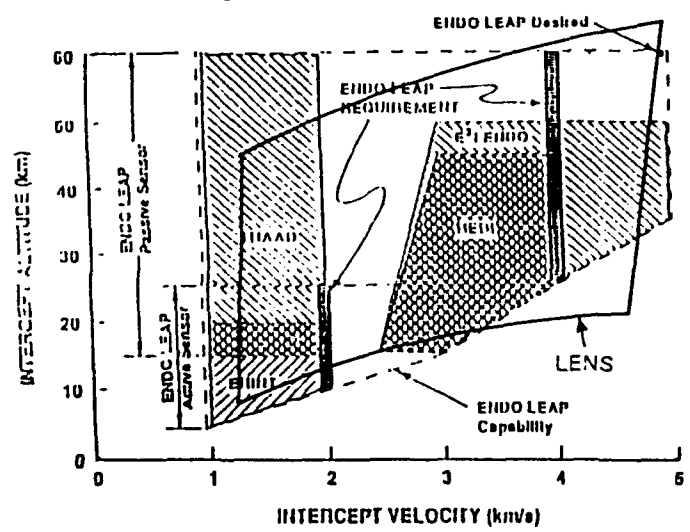


Fig. 7 Velocity altitude capabilities of LENS facility for major interceptor programs.

Table II. Summary of surface and flowfield instrumentation.

AEROTHERMAL INSTRUMENTATION	
SURFACE INSTRUMENTATION	FLOWFIELD INSTRUMENTATION
<ul style="list-style-type: none"> HEAT TRANSFER <ul style="list-style-type: none"> Thin Film Gages Gas Cap Radiation Gages Flush Electrostatic Probes Calorimeter Gages Coaxial Gages PRESSURE <ul style="list-style-type: none"> PCB Kulites SKIN FRICTION <ul style="list-style-type: none"> Force Balance - Accⁿ Comp. RADIATION AND ELECTRON DENSITY <ul style="list-style-type: none"> Gas Cap Radiation Gages Flush Electrostatic Probes 	<ul style="list-style-type: none"> INTRUSIVE <ul style="list-style-type: none"> Pitot Pressure Rake Total Temperature Rake Hot Film Rake Ion Probes Gas Samplers Total Enthalpy NON-INTRUSIVE <ul style="list-style-type: none"> Electron Beam Absorption Spectroscopy Microwave Interferometry

PERFORMANCE RANGE OF LENS FACILITY

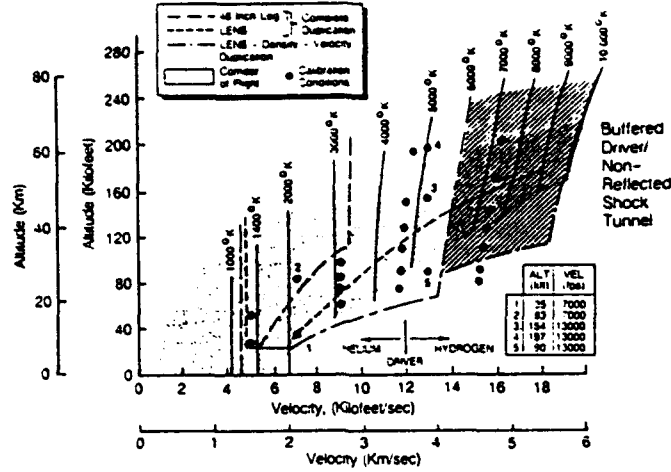


Fig. 8 Calibration conditions for LENS facility.

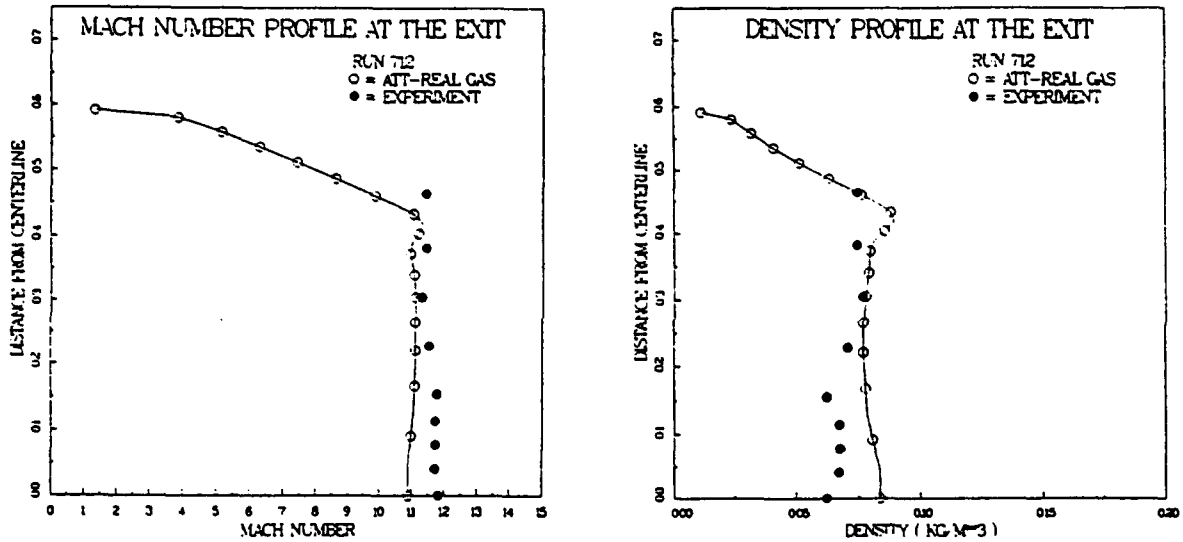


Fig. 9 Exit Mach number and density profiles of D-nozzle.

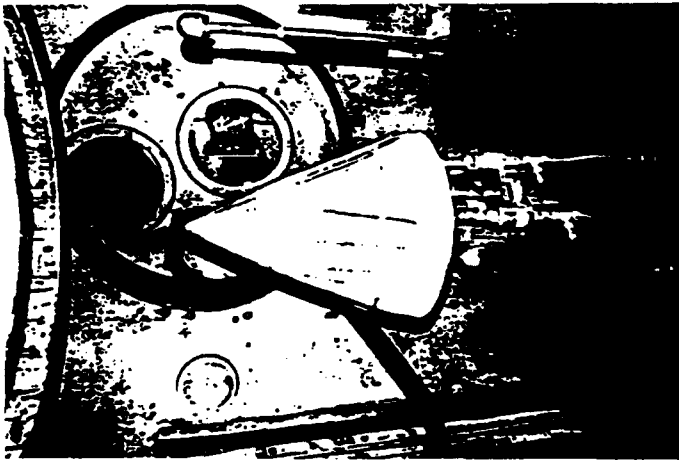


Fig. 10 HEDI seeker head in shock tunnel.

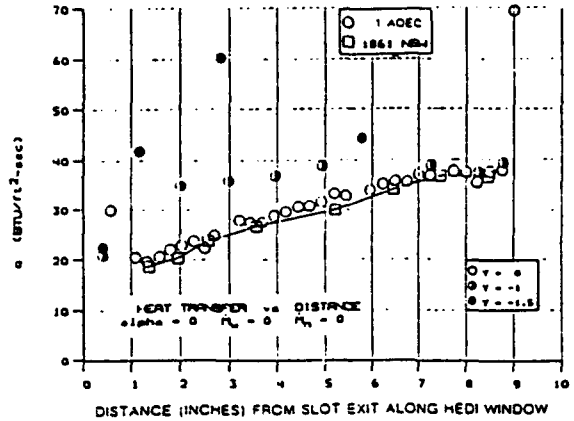


Fig. 11 Comparison between heat transfer measurements in shock tunnel and NSWC for uncooled HEDI window.

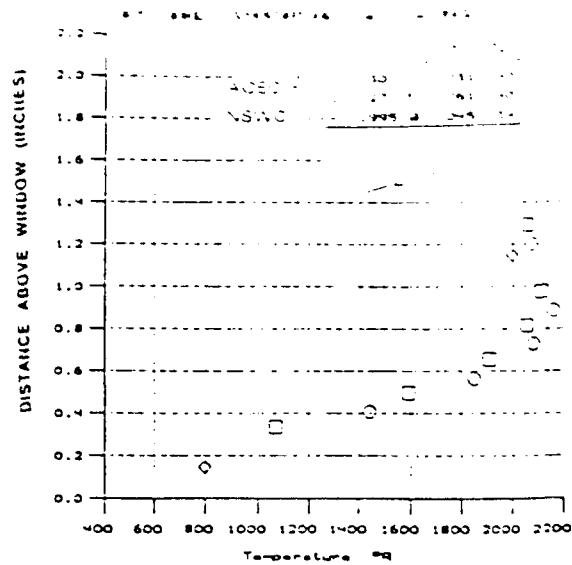
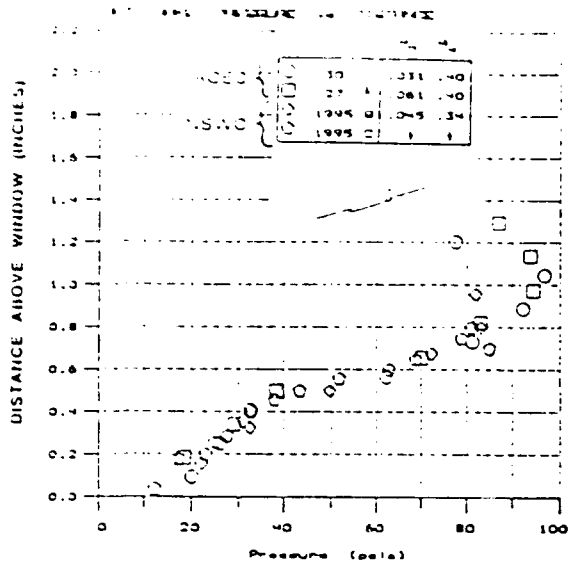


Fig. 12 Comparison between rake survey of pitot pressure and total temperature over HEDI window in NSAC and shock tunnel facilities.



Fig. 13 Inlet compression ramp installed in 48" shock tunnel.

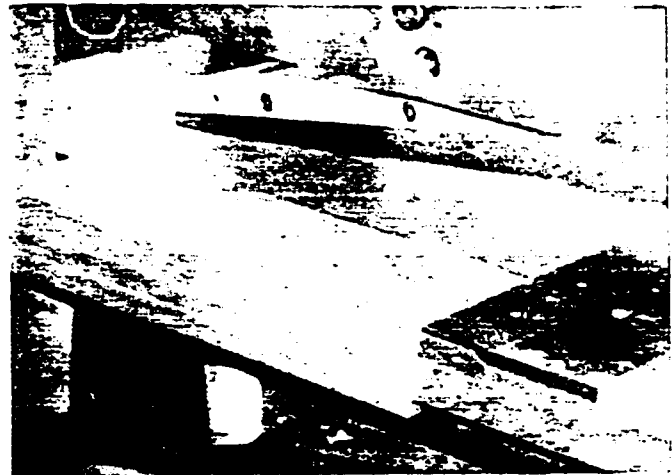


Fig. 15 Transpiration-cooled surface model with shock generator.

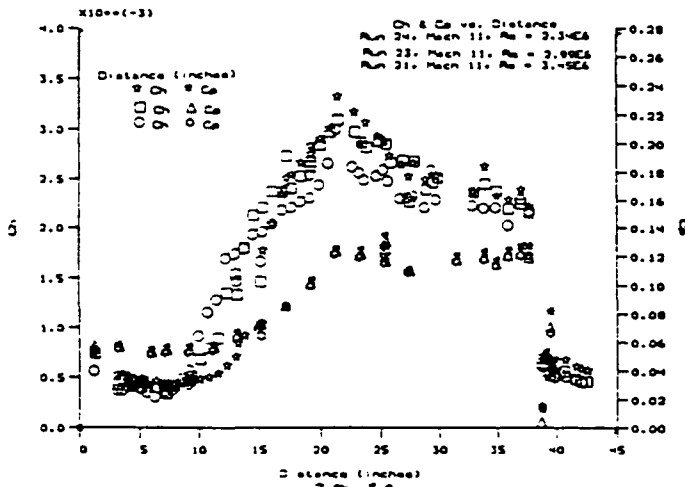


Fig. 14. Distribution of heat transfer and pressure on compression ramp for three Reynolds numbers at Mach 11.

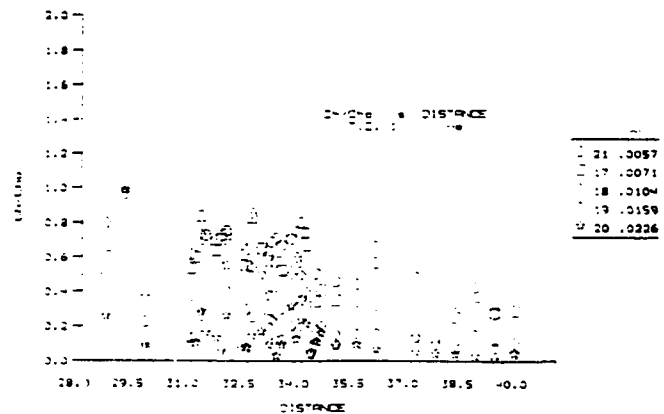


Fig. 16 Variation of distribution of heating on transpiration-cooled surface with cooling rate.

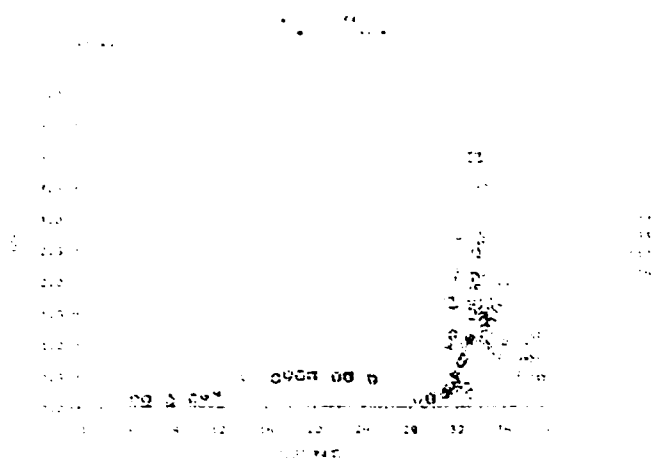


Fig. 17 Variation in the heat transfer, in flows with shock impingement, with transpiration-cooling rate.

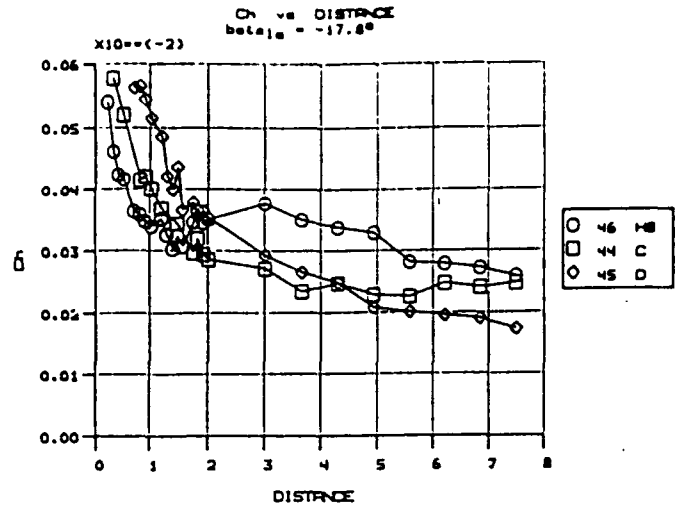


Fig. 19 Distribution of heating rate in turbulent and relaminarizing flow on expansion surface.



Fig. 18 Flat plate expansion surface model used in relaminarization studies.

Best Available Copy

APPENDIX 2

AIAA PAPER NO. 91-1778

**STUDIES OF THE MEAN AND UNSTEADY STRUCTURE OF
TURBULENT BOUNDARY LAYER SEPARATION IN
HYPERSONIC FLOW**



AIAA 91-1778

**Studies of the Mean and Unsteady
Structure of Turbulent Boundary Layer
Separation in Hypersonic Flow**

M.S. Holden

Calspan-University at Buffalo Research Center
Buffalo, NY

**AIAA 22nd Fluid Dynamics, Plasma Dynamics
& Lasers Conference**

June 24-26, 1991 / Honolulu, Hawaii

STUDIES OF THE MEAN AND UNSTEADY STRUCTURE OF TURBULENT BOUNDARY LAYER SEPARATION IN HYPERSONIC FLOW*

M.S. Holden**
Calspan-UB Research Center
P.O. Box 400
Buffalo, NY 14225

Abstract

An experimental study in which surface and flowfield measurements were made has been conducted to examine the structure of turbulent flow separation over large cone/flare configurations. This study was conducted in Calspan's 96-Inch Shock Tunnel, at Mach numbers of 11, 13 and 16, and at Reynolds numbers up to 100×10^6 . Surface heat transfer and pressure measurements were made in attached and separated flows at the cone/flare junction for 30° and 36° flare angles. Flowfield surveys were made in the separated region with pitot pressure and total temperature rakes. Holographic interferometry and Schlieren photography were used to obtain details of the flowfield structure. This study suggests that, in hypersonic flow, the separation region extends only a very small fraction of the boundary layer thickness and is a highly unsteady process. Only by employing instrumentation with frequency response high enough to follow the unsteady movement of the separation shock is it possible to determine the fundamental structure of flow separation in turbulent hypersonic flows.

1. Introduction

The emergence of advanced high-speed computing capabilities and numerical techniques, coupled with major increases in the need for numerical solutions to the full and reduced Navier-Stokes equations, has resulted in a refocusing of both pure and applied experimental research. Direct experimental simulation of complete aerodynamic configurations has in the past been the backbone of design efforts for new aerospace vehicles. However, recent applied experimental research has been increasingly directed toward acquiring more detailed measurements on segments of such configurations for code "validation" purposes. This is particularly true for hypersonic

vehicle design, where complete experimental simulation is difficult above Mach 13. Likewise, in pure research, the role of recent experiments has been increasingly one of providing insight into the macroscopic modeling of the flow (e.g., turbulence modeling) rather than as a means of constructing and validating gross flowfield models. In both cases, there is an increasing emphasis on the determination of flowfield properties, which, in many cases, provides the more direct and definitive evaluation of the modeling employed in the codes. Also, the increased emphasis on turbulent interacting and separated flows has resulted in a key need for time-resolved measurements over a broad frequency range. These requirements place a premium on flow quality and duration of tests, as well as on sophisticated high-frequency surface and flowfield instrumentation.

Recently, intense use of numerical solutions of full or reduced time-averaged Navier-Stokes equations has resulted in significant progress in the development of efficient and stable numerical algorithms and in greater understanding of gridding techniques. However, little real progress has been made in developing the fluid mechanical models required for these codes. In many instances, the phenomena of greatest importance in the aerothermal design of advanced vehicles are also the most difficult to model in the codes. The aerothermal loading and flowfield distortion that often accompany regions of viscous/inviscid interaction in hypersonic flow present some of the most important and difficult problems for both the designer and the predictor. Compressibility effects, shock/turbulence interaction, and the gross instabilities associated with separated flows must also be studied. In hypersonic flows, modeling of turbulence in regions of strong pressure gradients, embedded shocks, and separated flow is a key problem.

* This work was supported by the U.S. Air Force under AFOSR Contract No. F33615-85-C-3003. This paper is declared a work of the U.S. Government and is not subject to copyright protection in the United States.

** Staff Scientist; Associate Fellow, AIAA

To provide the information required to construct and verify the turbulence models used in the codes, flowfield measurements and direct measurements of skin friction and heat transfer must be obtained. Surface pressure data provide little information to validate codes and do not provide insight for turbulence modeling. To understand the structure of hypersonic turbulent boundary layers and shear layers as well as boundary layer separation in regions of shock wave/boundary layer interaction, we must understand the structure of the flow at the base of the boundary layer (at the wall and sublayer of the turbulent flow). For separated flows, such measurements can be made only with nonintrusive techniques with high spatial resolution on large models. As difficult as it is to make such measurements in high-enthalpy hypersonic flows, only by obtaining both the mean and fluctuating components of these flows can sufficient evidence be obtained to construct meaningful models of these flows.

For the last four years, we have embarked upon a program to design, develop, and construct the experimental tools required to: (i) make mean and fluctuating surface and flowfield measurements, and (ii) provide the insight and model validation required to develop detailed numerical solutions that would form the basis for future predictive capabilities. We have also pursued design studies and a shock tunnel modification program to provide a test capability tailored to generate flows of the highest quality and duration for fundamental studies of turbulent hypersonic flows. Instrumentation already developed includes miniature pitot pressure and total temperature probes for high-enthalpy, high Reynolds number flows, and a range of unique surface instrumentation. Two flowfield measurement techniques have also been developed specifically for shock tunnel studies of high Reynolds number hypersonic flows. Electron-beam fluorescence instrumentation was developed specifically to make mean and fluctuating density measurements in turbulent boundary layers at pressures up to 100 torr. Holographic interferometry techniques are being developed to measure flowfields in complex shock interaction regions. Presently, we are constructing and testing a series of unique models that will enable us to develop and explore the flow phenomena that we believe are central to developing prediction techniques that accurately describe complex interacting turbulent flows, with embedded separated regions.

This paper describes a program of experimental research to examine the mean and fluctuating boundary and shear layer structures in regions of strong pressure gradient and flow separation over models in hypersonic flows. Section 2 describes the objective and design of the experimental program, and the facilities, test conditions, models, and instrumentation used in the study. The results of the preliminary study are described in Section 3. In Section 4, we discuss the design of our current program. The conclusions of the preliminary study are summarized in Section 5.

2. Experimental Program

2.1 Program Objectives and Design of the Experimental Study

The major objective of this study was to develop and use models and instrumentation to obtain detailed measurements of the profile characteristics of a turbulent boundary layer ahead of and through regions of flow separation induced by shock wave/boundary layer interaction over a large cone/flare configuration. Such measurements are of key importance in evaluating the theoretical modeling of the turbulent separation process in hypersonic flows. As discussed in the introduction, current turbulence models are incapable of describing the complex development of turbulence in regions of strong pressure gradients and boundary layer separation in hypersonic flow. For these flows, we believe that compressibility, shock/turbulence interaction, and gross flow unsteadiness are important under hypersonic highly cooled wall conditions. In hypersonic high Reynolds number flows over highly cooled walls, the "wall layer," in which our earlier studies¹ have suggested separation first takes place, and which contains the principal information on the character of the boundary layer, is very thin. Boundary layer thicknesses of over 1 inch are required to enable this layer to be probed with the required resolution. While turbulent boundary layers originating on the walls of hypersonic nozzles have been used as sources of thick turbulent boundary layers in experimental studies, it has been shown that significant turbulent non-equilibrium effects can exist in these nozzle flows². The distortion of the structure and turbulent characteristics of the boundary layer generated through the strong expansion in the nozzle can persist well downstream of the nozzle exit plane and can significantly influ-

ence the characteristics of a separating turbulent boundary layer.¹ For this reason, we elected to perform a study to examine the characteristics of the constant-pressure turbulent boundary layer ahead of and in regions of shock wave/boundary layer interaction on a large slender cone/flare configuration in the large contoured "D" nozzle in the Calspan 96-Inch Shock Tunnel. The technique employed in the design of the "D" nozzle, and indeed most contoured nozzles, is such that the test core is a cone-shaped region of uniform flow that originates well upstream of the exit plane. Thus, by designing a conical model so that it can be fit within this uniform conical region, it is possible to develop a constant-pressure boundary layer over a large conical model that extends well into the contoured nozzle. The ultimate objective of the overall program is to obtain both mean and fluctuation measurements on the surface and across the turbulent layer. However, during this preliminary study, we concentrated on obtaining measurements of the mean properties across the viscous layer—more specifically, measurements of the pitot pressure, total temperature, total heat transfer rate, and (using holographic interferometry) the mean density distribution.

2.2 Experimental Facilities and Test Conditions

The experimental study was conducted in the Calspan 96-Inch Shock Tunnel at Mach 11, 13, and 16 for Reynolds numbers from 30×10^6 to 80×10^6 . Under these conditions, the boundary layer is fully turbulent well upstream of the cone/flare junction, and, as discussed in the following section, the measurements of heat transfer were in good agreement with prediction techniques based on a large number of measurements on highly cooled walls in high Reynolds number hypersonic flows. The test conditions at which the studies were conducted are listed in Table 1.

The facility and its performance characteristics are described in Reference 3. The shock tunnel is basically a "blowdown tunnel" with a shock compression heater. The 96-inch shock tunnel used in this study is shown in Figure 1a. The operation of the shock tunnel in the reflected-shock mode is shown with the aid of the wave diagram in Figure 1b. The tunnel is started by rupturing a double diaphragm, permitting high-pressure helium in the driver section to expand

Table 1
TEST CONDITIONS, LARGE 6° CONE

	AIR			N ₂
	3,4,8	6,7	9	5,10-15
M_i	3.345E+00	3.633E+00	4.200E+00	2.635E+00
p_o (psia)	7.216E+03	1.760E+04	1.705E+04	5.430E+03
H_o (ft ² /sec ²)	1.825E+07	2.147E+07	2.795E+07	1.287E+07
T_o (°R)	2.717E+03	3.104E+03	3.875E+03	1.939E+03
M	1.096E+01	1.301E+01	1.543E+01	1.111E+01
U (ft/sec)	5.922E+03	6.458E+03	7.404E+03	4.981E+03
T (°R)	1.214E+02	1.026E+02	9.574E+01	8.065E+01
p_w (psia)	9.172E-02	7.345E-02	1.860E-02	6.698E-02
q_w (psia)	7.721E+00	8.712E+00	3.104E+00	5.800E+00
q_w (slug/ft ³)	6.340E-05	6.038E-05	1.631E-05	6.734E-05
μ_w (slug/ft/sec)	1.021E-07	8.634E-08	8.054E-08	6.783E-08
Re/ft	3.680E+06	4.544E+06	1.499E+06	4.945E+06
p_o' (pitot)(psia)	1.431E+01	1.619E+01	5.798E+00	1.070E+01

into the driven section. This generates a normal shock, which propagates through the low-pressure air. A region of high-temperature, high-pressure air is produced between this normal-shock front and the gas interface (often referred to as the contact surface) between the driver and driven gases. When the primary or incident shock strikes the end of the driven section, it is reflected, leaving a region of almost stationary, high-pressure, heated air. This air is then expanded through a nozzle to the desired freestream conditions in the test section.

The stagnation and freestream test conditions were determined based on measurements of the incident shock wave speed, U_i , the initial temperature of the test gas (in the driven tube), T_1 , the initial pressure of the test gas, p_1 , and the pressure behind the reflected shock wave, p_o . We calculated the incident shock wave Mach number, $M_i = U_i/a_1$, where the speed of sound, a_1 , is a function of p_1 and T_1 . The freestream Mach number, M_∞ , was determined from correlations of M_∞ with M_i and p_o . These correlations were based on previous airflow calibrations of the "D" nozzle used.

Freestream test conditions of pressure, temperature, Reynolds number, etc., were computed based on isentropic expansion of the test gas from the conditions behind the reflected shock wave to the freestream Mach number. Real gas effects were taken into account for this expansion under the justified assumption that the gas was in thermochemical equilibrium. In the freestream, the static temperature, T_∞ , was sufficiently low that the ideal gas equation of state, $p_\infty = \rho \bar{R} T_\infty$ was applicable, where \bar{R} is the gas constant for the test gas.

The stagnation enthalpy, H_o , and temperature, T_o , of the gas behind the reflected shock wave (shown as region 4 in Figure 1b) were calculated from:

$$H_o = (H_4/H_1)H_1 \text{ and } T_o = (T_4/T_1) T_1 \quad (1)$$

where (H_4/H_1) and (T_4/T_1) are functions of U_i (or M_i) and p_1 and are given in Reference 4 for air. H_1 was obtained from Reference 5 for air, knowing p_1 and T_1 .

The freestream static temperature was found from the energy equation, knowing H_o and M_∞ .

$$T_\infty = \frac{H_o}{c_p} \left(\frac{1}{1 + \frac{(\gamma-1)}{2} M_\infty^2} \right) \quad (2)$$

where $c_p = 6006 \text{ ft-lb/slug/R}^\circ$ and $\gamma = 1.40$.

The freestream static pressure was calculated from

$$p_\infty = \frac{P}{P_p} p_o \left(1 + \frac{(\gamma-1)}{2} M_\infty^2 \right)^{\left(\frac{-\gamma}{\gamma-1} \right)} \quad (3)$$

where
$$\frac{P}{P_p} = \frac{(p_\infty/p_o)_{REAL}}{(p_\infty/p_o)_{IDEAL}} \quad (4)$$

is the real gas correction to the ideal gas static-to-total pressure ratio as described in Reference 6. The sources for the real gas data used in this technique are References 7 and 8.

The freestream velocity was determined from

$$U_\infty = M_\infty a_\infty \quad (5)$$

where
$$a_\infty = \sqrt{\gamma \bar{R} T_\infty} \quad (6)$$

the speed of sound.

The freestream dynamic pressure was found from

$$q_\infty = 1/2 \gamma p_\infty M_\infty^2 \quad (7)$$

and the freestream density then was calculated from the ideal gas equation of state

$$\rho_\infty = p_\infty / \bar{R} T_\infty \quad (8)$$

where $\bar{R} = 1717.91 \text{ ft-lb/slug/R}^\circ$ for air. Values of the absolute viscosity, μ , used to compute the freestream Reynolds number per foot were obtained using the technique described in Reference 4.

The test section pitot pressure, p_o' , was determined from q_∞ and the ratio (p_o'/q_∞) . This

ratio has been correlated as a function of M_∞ and H_o for normal-shock waves in air in thermodynamic equilibrium.

For the test conditions at which our study was conducted, the uncertainty in pitot pressure measurements from errors in calibration and recording is $\pm 2.5\%$. The reservoir pressure can be measured with an uncertainty of $\pm 2.0\%$, and the total enthalpy (H_o) can be determined from the driven tube pressure and the incident-shock Mach number with an uncertainty of $\pm 1.5\%$. These measurements combine to yield an uncertainty in the Mach number and dynamic pressure measurements of $\pm 0.8\%$ and $\pm 3.5\%$, respectively.

2.3 Models and Instrumentation

2.3.1 Cone/Flare Model

As discussed in the previous subsection, the large conical region of uniform flow that extends well into the contoured "D" nozzle allows us to generate a constant-pressure boundary layer on a conical model that extends into the nozzle.

For this study, we selected a large 6° cone with flares of 30° and 36° attached at its base. The cone/flare configuration is shown in Figure 2. The cone angle and length were selected, on the basis of calculations, to achieve the maximum length over which uniform constant-pressure flow could be established within the further constraints of tunnel blockage and sting loading. A diagram of the cone/flare model and its positioning within the "D" nozzle is shown in Figure 3. In an initial experiment to demonstrate that this large model could be used to produce the required flow, we obtained pressure and heat transfer for this model equipped with both sharp and blunt nosetips. The good agreement between the measured pressure and heat transfer distributions and theory for these configurations, shown in Figures 4 through 8, is described in Section 3 and demonstrates that the design and positioning of the model have produced the required testing environment.

2.3.2 Heat Transfer Instrumentation

Platinum thin-film instrumentation was used to obtain heat transfer measurements on the surface of the cone/flare model and as the sensing element of the 0.05-inch-diameter stagnation heating probes. Because each of these gages has a 1-MHz frequency response, it can be used to examine the unsteady characteristics of the turbulent boundary layer and separated region. The large

gradients that are generated along the walls and in the flow in the separation and reattachment region of shock wave/boundary layer interactions make it essential that distortion of the heat transfer distribution resulting from lateral heat conduction be minimized by employing models constructed with low-conductivity materials. The Pyrex-backed thin-film gages, with their high resolution, sensitivity, and frequency response, are almost ideal for this type of study. The platinum thin-film probes shown in Figure 9 were used, in conjunction with the total temperature instrumentation, to examine the structure of the turbulent boundary layer and shear layer.

The thin-film heat transfer gage is a resistance thermometer that reacts to the local surface temperature of the model. The first step of the data reduction was to convert the measured voltage time history for each gage to a temperature time history, taking into account the gage resistance, the current through the gage, the gage calibration factor, and the amplifier gain. The theory of heat conduction was used to relate the surface temperature to the rate of heat transfer. The platinum resistance element has negligible heat capacity and, hence, negligible effect on the Pyrex-substrate surface temperature. The substrate can be characterized as being homogeneous and isotropic. Furthermore, because of the short duration of a shock tunnel test, the substrate can be treated as a semi-infinite body. The final data reduction was done using the Cook-Felderman⁹ algorithm.

The Stanton number, C_H , based on the freestream conditions, was calculated from the following

$$C_H = \frac{\dot{q}}{\rho_\infty U_\infty (H_o - H_w)} \quad (9)$$

where H_w is the enthalpy at the measured wall temperature.

For the thin-film heat transfer instrumentation, the uncertainties associated with the gage calibration and the recording equipment are estimated to be $\pm 5\%$ for the levels of heating obtained in the preliminary study.

2.3.3 Pitot and Static Pressure

Instrumentation

Calspan-designed and constructed piezo-electric pressure transducers mounted in pitot pressure rakes, and beneath orifices in the model surface, were used to obtain the mean pitot pressure through the boundary layer and the static pressure along the surface, respectively. The pitot pressure gages had 0.030-inch orifices and were staggered as shown in Figure 9 to achieve a transverse spacing of 0.010 inch at the base of the boundary layer.

The pressures were converted to absolute pressures (psia) by adding the measured initial vacuum pressure in the test section. The latter was the reference pressure for the transducers. The pressures were then averaged over the time interval of steady flow to obtain an average value for each case. The values of the pressure coefficients, C_p , were calculated from

$$C_p = p / (1/2 \rho_\infty U_\infty^2) \quad (10)$$

where p was the measured model pressure (psia).

The uncertainties in the pressure measurements associated with the calibration and recording apparatus are $\pm 3\%$. Again, the variations associated with the unsteady nature of the fluid dynamics can be as large as $\pm 15\%$.

2.3.4 Total Temperature Instrumentation

A significant effort was devoted to the design and development of a total temperature gage that responded within 2 milliseconds, withstood the large static and dynamic pressures generated in regions of shock/boundary layer interaction in the shock tunnel flows, and was small enough to resolve the total temperature in the wall layer. The result of this development was a gage 0.030 inch in diameter that uses a 0.0005-inch butt-welded iron/constantan thermocouple in the arrangement shown schematically in Figure 10. The typical response of one of these gages (Figure 11) clearly shows that we have adequate time to obtain accurate measurement. A small amount of radiation (2% of full scale) is applied, and this factor is checked for measurements in the freestream, where the total temperature is known accurately. The gages were deployed in a staggered array (Figure 9) similar to that employed for the pitot pressure gages.

2.3.5 Flow Visualization

We used a single-pass Schlieren system with a focal length of 10 feet for flow visualization in these studies. The horizontal knife edge used in these studies was adjusted to give between 15% and 50% cutoff. A single microsecond spark was triggered close to the end of the steady run time. The tunnel windows have 16-inch diameters.

3. Results and Discussion

The experimental study had two objectives. First, we sought to generate a model and environment in which we could establish a thick, well developed and defined turbulent boundary layer under constant-pressure conditions. We then sought to design, develop, and use instrumentation to obtain mean and fluctuating profile measurements: first, in the constant-pressure boundary layer; then, in regions of strong adverse pressure gradient in regions of shock wave/boundary layer interaction generated at a cone/flare junction. In the preliminary study, we employed two cone/flare configurations, one (a 30° flare) that promoted a flow close to incipient separation, and a second (a 36° flare) that promoted a well-separated flow.

The measurements of the heat transfer and pressure distributions over the two cone/flare configurations are shown in Figures 4 through 8. The measurements of the pressure along the entire length of the cone were in good agreement with predictions based on Sim's solutions for a sharp cone, and the pressures at the back of the flare were in good agreement with calculations based on an inviscid shock compression from the cone to the flare, as shown in Figures 5 and 6. Based on comparisons and correlations with a large number of heat transfer and skin friction measurements made on flat plates and cones in the shock tunnels and in other high Reynolds number hypersonic facilities, we have found that predictions based on the Van Driest(II) technique¹⁰ are in best agreement for hypersonic flows over highly cooled walls. The Van Driest method is based on a transformation to relate measurements in compressible flow to those in incompressible flow. Here, the measured coefficient of local skin friction and heat transfer rate (C_{f_i} and C_{H_i}) are related to an equivalent quantity in an incompressible flow (C_{f_i} and C_{H_i}) through the relationships

$$C_{f_i} = F_c \left(M_e, \frac{T_w}{T_o} \right) C_f \quad \text{and} \quad C_{H_i} = F_c \left(M_e, \frac{T_w}{T_o} \right) C_H$$

The local Reynolds numbers, Re_θ and Re_x , based on the momentum thickness, θ , and on the distance from the virtual origin, X_v , respectively, are related to similar quantities in the incompressible plane through the relationships

$$F_c C_f = F_\theta Re_\theta \\ F_c C_f = F_x Re_x$$

We have assumed the Karman-Schoenherr¹¹ relationship

$$\log_{10}(Re_x C_{F_i}) = \log_{10}(2Re_\theta) = 0.242(C_{F_i})^{-1/2}$$

where the average skin friction, C_{F_i} , is related to the local skin friction, C_{f_i} , by

$$C_{f_i} = 0.242 C_{F_i} [0.242 + 0.8686(C_{F_i})^{1/2}]^{-1}$$

Van Driest's analysis is based on the Prandtl-Karman¹² mixing length model, together with a compressibility transformation, to describe the compressible turbulent boundary layer over a flat plate. From this analysis, the transformation or compressibility factors are

$$(F_c)_{VD} = r m_e (\sin^{-1} \alpha + \sin^{-1} \beta)^{-2}$$

$$(F_\theta)_{VD} = \mu_e / \mu_w$$

and $F_x = F_\theta F_c^{-1}$

where

$$\alpha = (2A^2 - B) / (4A^2 + B^2)^{1/2} \quad \text{and} \quad \beta = B / (4A^2 + B^2)^{1/2}$$

and

$$A = \left[r m_e \left(\frac{T_w}{T_e} \right)^{-1} \right]^{1/2} \quad \text{and} \quad B = \left(1 + r m_e - \frac{T_w}{T_e} \right) \left(\frac{T_w}{T_e} \right)^{-1}$$

where a recovery factor, r , of 0.89 was used, and $m_e = \frac{\gamma - 1}{2} M_e^2$.

To compare the prediction methods with the experimental measurements in the $C_f F_c - F_\theta Re_\theta$ plane, the momentum thickness, θ , must be calculated. We have used the relation-

ship from the momentum equation $\theta = \int_0^x C_f / 2 dx$ to calculate this quantity. For our measurements in transitional and turbulent flows, we found that the Reynolds analogy factor was close to unity, as shown in Figures 12 and 13. Thus, when only heat transfer measurements were available, we calculated the momentum thickness from the expression $\theta = \int_0^x C_H dx$.

In correlating the measurements made on the conical models in the expression $F_c C_H - F_{R_x} Re_x$, we employed the Mangler¹³ transformation in the form suggested by Bertran and Neal¹⁴ to relate the measurements on the cones to an equivalent two-dimensional flow. For an equal distance from the virtual origin of the turbulent boundary layer on flat plates and cones, the local Stanton number on the cone would be larger than that on a flat plate by the ratio

$$\frac{(C_H)_{cone}}{(C_H)_{fp}} = \left(\frac{2n-1}{n-1} \right)^{1/n} \left[\left(1 + \frac{R_{xv}}{R_x} \right) - \frac{R_{xv}}{R_x} \left(\frac{R_{xv}/R_x}{1 + (R_{xv}/R_x)} \right)^{n/(n-1)} \right]^{-1/n}$$

where $n = 0.429 + 0.404 \ln(F_x \cdot Re_x)$.

By employing the above equation, the measurements on the conical bodies were transformed into the equivalent two-dimensional compressible plane, and, subsequently, to the incompressible plane.

A typical comparison between a large body of heat transfer measurements obtained earlier and the Van Driest approach is shown in Figure 14. The good agreement between the heat transfer measurements on the large cone and the Van Driest prediction technique suggests that, at both Mach 11 and 13 (shown in Figures 12 and 13), the boundary layers are well developed.

Flowfield surveys were made to determine the distributions of pitot pressure, total temperature, and total heat transfer at a number of stations through the interaction region at each of the flow conditions described above. Figures 15 and 16 show the pitot and total temperature measurements for the Mach 11 condition with a 30° flare. The profiles, which were obtained at 2, 1.2, 0.8, and 0 inches ahead of the cone/flare junction, indicate that there is very little upstream influence

at this condition. (A similar set of measurements for the 36° flare is shown in Figures 17 and 18.)

$$\frac{T}{T_w} = 1 + \left[(1 - C_t)(1 + m_e) \frac{T_e}{T_w} - 1 \right] \frac{u}{u_e} + \frac{T_e}{T_w} \left[C_t \left(\frac{1 + m_e}{m_e} \right) - 1 \right] m_e \left(\frac{u}{u_e} \right)^2$$

$0 < C_t < 0.5$; $C_t = 0$ for Crocco, $C_t = 0.5$ for quadratic.

These measurements are compared with the Crocco relationship between enthalpy and velocity in Figure 19. It is clear that our measurements follow a parabolic relationship

$$\frac{\overline{P}_{wake}}{\overline{P}_{cone}} = \left[\frac{(\gamma + 1)M_b^2}{2} \right]^{\frac{\gamma}{\gamma-1}} \cdot \left[\frac{\gamma + 1}{2\gamma M_b^2 - (\gamma - 1)} \right]^{\frac{1}{\gamma-1}}$$

$$\frac{u_b}{u_e} = \left(\frac{M_b}{M_e} \right) \left(\frac{T_{ob}}{T_{oe}} \right)^{1/2} \left(\frac{1 + m_b}{1 + m_e} \right)^{1/2}$$

rather than Crocco's linear relationship

$$\frac{T_d}{T_w} = 1 + B \left(\frac{u}{u_e} \right) - A^2 \left(\frac{u}{u_e} \right)^2$$

In the past, it has been assumed that the "fuller than Crocco" velocity profile obtained in studies over tunnel walls was associated with turbulent nonequilibrium effects related to the strong favorable pressure gradient upstream on the nozzle wall; however, no such explanation can be advanced to explain our results.

Of the transformation techniques that have been postulated to cast the compressible flow measurements into an equivalent incompressible form, the relationships derived by Van Driest have received the greatest support. Van Driest starts with the assumption that the Crocco relationship is valid and uses the mixing length theory to calculate the Reynolds stresses in the flow. By inspection, the transformation is

$$\frac{u^*}{u_e} = \frac{1}{A} \sin^{-1} \left(\frac{2A^2 \frac{u}{u_e} - B}{(B^2 + 4A^2)^{1/2}} \right) + \frac{1}{A} \sin^{-1} \left(\frac{B}{(B^2 + 4A^2)^{1/2}} \right)$$

The original form of the incompressible law of the wall relationship is

$$\frac{u^*}{u_\tau} = \frac{1}{K} \ln y^* + C$$

However, because the wake region of the flow is so extensive, Maise and McDonald¹⁵ have suggested that the Coles¹⁶ wake function be included:

$$\frac{u^*}{u_\tau} = \frac{1}{K} \ln y^* + C + \frac{\pi}{K} W \left(\frac{y}{\delta} \right)$$

They, in fact, suggest a defect form of this relationship:

$$\frac{u^* - u^*}{u_\tau} = f \left(\frac{y}{\delta} \right) = \frac{1}{K} \ln \left(\frac{y}{\delta} \right) + C(2 - W)$$

Comparisons between our measurements in each of the incompressible formats are shown in Figures 20 and 21. It is clear that the transform is not as successful at these high Mach numbers as it has been below Mach 5. Comparisons between the measurements and these prediction techniques in the compressible plane are shown in Figure 22. It can be seen that this is a relatively insensitive way of examining the measurements.

4. Ongoing Studies

We are now studying the mean and fluctuating turbulent flow structure over two basic flow axisymmetric configurations: (i) a large cone/flare model (Figure 23) and (ii) an axisymmetric curved compression ramp (Figure 24). The measurements made in each of these flows are designed principally to examine the response of the turbulent flow structure in a flow strained by an adverse pressure gradient—in one case, with a strong embedded shock system. Flowfield measurements with both non-intrusive and intrusive instrumentation are focused on obtaining the streamwise variation of turbulent scale size through the interaction regions. We are examining the surface and flowfield fluctuation measurements to determine shock/turbulence interaction and the magnitude and mechanisms of large-scale flow instabilities in separated interaction regions. Direct measurements of density and density fluctuation with the electron-beam fluorescence equipment enable us to determine directly the magnitude of turbulent compressibility effects in these flows. The experimental studies are being conducted at freestream Mach numbers of 11, 13, and 15, which give conditions on the cone from

Mach 9 to 12 where we believe compressibility effects are of importance. The large model scale enables us to obtain boundary layer thicknesses up to 2 inches, which give good resolution at the base of the viscous layer as well as generate high Reynolds number, fully turbulent flows.

The models are equipped with high-frequency heat transfer, skin friction, and pressure instrumentation. The major flowfield instrumentation is electron-beam fluorescence equipment, installed as shown schematically in Figure 25. The traverse mechanism shown in Figure 26 enables flowfield measurements to be made at streamwise stations encompassing the complete interaction region. High-frequency thin-film, pitot pressure, and total temperature measurements can be made at each streamwise station of interest. The large aperture optical system being used is designed to enable us to record and analyze turbulent fluctuation measurements up to 1 MHz. These optics give us the ability to obtain a 0.010-inch resolution across the 1.5-inch boundary layer, as shown in Figure 27.

Detailed flowfield fluctuation measurements are being made for three cone/flare configurations to obtain attached, incipient separated, and well-separated flow, respectively. Figure 26 shows the basic cone/flare model configuration with the electron-beam optics installed and the separated flow generated by a 36° ramp (flare). Two additional ramp angles, of 30° and 28° are being employed in these studies. Additional studies of the response of turbulence to adverse pressure gradients are being conducted for the axisymmetric curved compression ramp model shown in Figure 28. Here, the turbulence is not subjected to as great an adverse pressure gradient, and we do not expect the shock/turbulence interaction associated with the shock system embedded within the boundary layer to be as significant.

Double-pulsed holographic interferometry is being used to determine both the mean flowfield density distribution and, with pulse separations of the order of 1 microsecond, the variation of turbulent scale size through the interaction region. The mean distributions of flow properties across the boundary layers and shear layers are being determined from the probes and from the electron-beam and interferometry measurements, so we have a number of independent ways of calculating the same property. For example, the mean density can be deduced independently from measurements using the electron beam, using in-

terferometry, and using a combination of total temperature and total pressure measurements. Static temperatures can be determined directly from the electron-beam measurements and from a combination of probe measurements. The major efforts in analysis of the measurements are being directed to definition of the turbulent and unsteady structure of these flows. Knowledge of the streamwise and transverse variations of turbulent scale size through the interaction regions is of key importance to the evaluation of the models of turbulence. Scale size measurements are to be determined independently from cross-correlations of transverse-fluctuation measurements with those obtained using electron-beam, pitot pressure, and thin-film instrumentation. Turbulent spectra will also be obtained from the various measurement techniques to provide the correlations required for evaluating the turbulence models and for providing insight into the fluid mechanics associated with compressibility effects, shock/turbulence interaction, and large-scale flow unsteadiness.

5. Summary and Conclusions

An experimental study has been conducted to examine the detailed flowfield structure of a *separated boundary layer flow over a large cone/flare model*. In this study, the structure of the separating boundary layer was examined with pitot, total temperature, and laser holography measurements. These measurements suggest that the total temperature/velocity relationship in the cone boundary layer is quadratic rather than the usually assumed linear form suggested by Crocco. The Van Driest transformation, which has been used successfully in supersonic flows over adiabatic walls to relate the measured velocity to similar measurements in subsonic flow, is apparently not as effective in hypersonic flows over highly cooled walls. The measurements portray the rapid change in the structure of the sublayer as separation takes place, as well as the formation of strong shock waves in the turbulent shear layer.

Studies are now being made to examine the mean and fluctuating characteristics of boundary layers and separated shear layers in regions of adverse pressure gradient and shock wave/turbulent boundary layer interaction. In these studies, conducted at Mach numbers between 8 and 16, high-frequency heat transfer, skin friction, and pressure measurements are being made on a large cone/flare model and an axisymmetric curved

compression ramp model. Flowfield measurements are also being made with high-frequency pitot pressure, hot-film, and total temperature instrumentation, and advanced electron-beam fluorescence and holographic interferometry techniques will be used to make non-intrusive measurements of the mean and fluctuating density and the static temperature distributions throughout the flowfields.

Nomenclature

<i>A</i>	As Defined in Section 3
<i>a</i>	Speed of Sound
<i>B</i>	As Defined in Section 3
<i>C</i>	Constant
<i>C_F</i>	Average Skin Friction Coefficient
<i>C_f</i>	Local Skin Friction Coefficient
<i>C_H, C_H</i>	Stanton Number
<i>C_p, C_p</i>	Pressure Coefficient
<i>c_p</i>	Specific Heat at Constant Pressure
<i>C_t</i>	As Defined in Section 3
<i>F_c</i>	As Defined in Section 3
<i>F_R</i>	As Defined in Section 3
<i>F_θ</i>	As Defined in Section 3
<i>H</i>	Total Enthalpy
<i>K</i>	Mixing Length Constant
<i>M</i>	Mach Number
<i>m</i>	$= \frac{\gamma - 1}{2} M^2$
<i>p</i>	Pressure
<i>p₀'</i>	Pitot Pressure
<i>q</i>	As Defined in Section 3
<i>q̇</i>	Heat Transfer Rate
<i>q_∞</i>	Dynamic Pressure
<i>R̄</i>	Gas Constant
<i>Re</i>	Reynolds Number
<i>Re_θ</i>	As Defined in Section 3
<i>T</i>	Temperature
<i>U</i>	Velocity
<i>u_τ</i>	$= (\tau_w / \rho_w)^{1/2} = u_e \left(\frac{C_f T_w}{2 T_e} \right)^{1/2}$
<i>W</i>	Wake Function
<i>X_v</i>	Distance from Normal Origin

<i>y</i>	Normal Distance from Surface
<i>y*</i>	As Defined in Section 3

GREEK SYMBOLS

<i>γ</i>	Ratio of Specific Heat
<i>δ</i>	Boundary Layer Thickness
<i>δ_F, δ_{FLARE}</i>	Flare Angle
<i>θ</i>	Momentum Thickness
<i>μ</i>	Viscosity
<i>π</i>	As Defined in Section 3
<i>ρ</i>	Density

SUBSCRIPTS

<i>b</i>	Boundary Layer
<i>BE</i>	Beginning-to-End
<i>C</i>	As Defined in Section 3
<i>c</i>	As Defined in Section 3
<i>cone</i>	Cone Value
<i>e</i>	Edge
<i>fp</i>	Flat-Plate Value
<i>i</i>	Incident
<i>i</i>	Incompressible
<i>IDEAL</i>	Ideal Gas
<i>P</i>	Perfect Gas
<i>REAL</i>	Real Gas
<i>VD</i>	Van Driest
<i>w</i>	Wall
<i>x</i>	Distance from Virtual Origin
<i>ξ</i>	As Defined in Section 3
<i>0</i>	Stagnation Value
<i>1</i>	Initial Value
<i>1, 4</i>	Regions 1 and 4 As Defined in Figure 1(b)
<i>∞</i>	Freestream Value

SUPERSCRIPIT

<i>•</i>	Incompressible Conditions
----------	---------------------------

References

1. Holden, M.S., "Shock-Wave Turbulent Boundary Layer Interaction in Hypersonic Flow," AIAA Paper No. 72-74, Presented at AIAA 10th Aerospace Sciences Meeting, San Diego, CA, 17-19 January 1972.

2. Knight, D., "Improved Calculation of High-Speed Inlet Flows: Part I. Numerical Algorithm and Part III. Results," *AIAA Journal*, Vol. 19, pp. 34-41, 1972-1979, 1980.
3. "Calspan Hypersonic Shock Tunnel, Description and Capabilities Brochure," 1975.
4. Lewis, C.H. and Burgess, E.G., III, "Charts of Normal Shock Wave Properties in Imperfect Air (Supplement M = 1 to 10)," AEDC-TR-196, September 1965.
5. Hilsenrath, J., *et al.*, "Tables of Thermal Properties of Gases," NBS Circular 565, 1955.
6. Reece, J.W., "Test Section Conditions Generated in the Supersonic Expansion of Real Air," *Journal of Aeronautical Sciences*, Vol. 29, No. 5, May 1962, p. 617, 618.
7. Hilsenrath, J., *et al.*, "Tables of Thermodynamic Properties of Air Including Dissociation and Ionization from 1500°K to 15,000°K," AEDC-TR-59-20, December 1959.
8. Neil, C.A. and Lewis, C.H., "Interpolations of Imperfect Air Thermodynamic Data, II — at Constant Pressure," AEDC-TDR-64-184, September 1964.
9. Cook, W.J., "Determination of Heat Transfer Rates from Transient Surface Temperature Measurements," *AIAA Journal*, Vol. 8, No. 7, July 1970, pp. 1366-1368.
10. Van Driest, E.R., "Problem of Aerodynamic Heating," *Aeronautical Engineering Review*, Vol. 15, No. 10, October 1956.
11. Schoenherr, K.E., "Resistance of Flat Surfaces Moving Through a Fluid," *Soc. of Naval Arch. and Marine Engrs. Trans.*, Vol. 40, pp. 279-313, 1932.
12. von Karman, T., *The Problems of Resistance in Compressible Fluids*, GALCIT Pub. No. 75, 1936.
13. Howarth, L., *Modern Developments in Fluid Dynamics*, Oxford University Press, NY, 1953, pp. 382-386.
14. Bertram, M.H. and Neal, L., Jr., "Recent Experiments in Hypersonic Turbulent Boundary Layers," NASA Report No. TMX-56335, May 1965.
15. Maise, G. and McDonald, H., "Mixing Length and Kinematic Eddy Viscosity in a Compressible Boundary Layer." AIAA Paper No. 67-199, January 1967.
16. Coles, D., "Measurements in the Boundary Layer on a Smooth Flat Plate in Supersonic Flow," Ph.D. Thesis, California Institute of Technology, 1953.

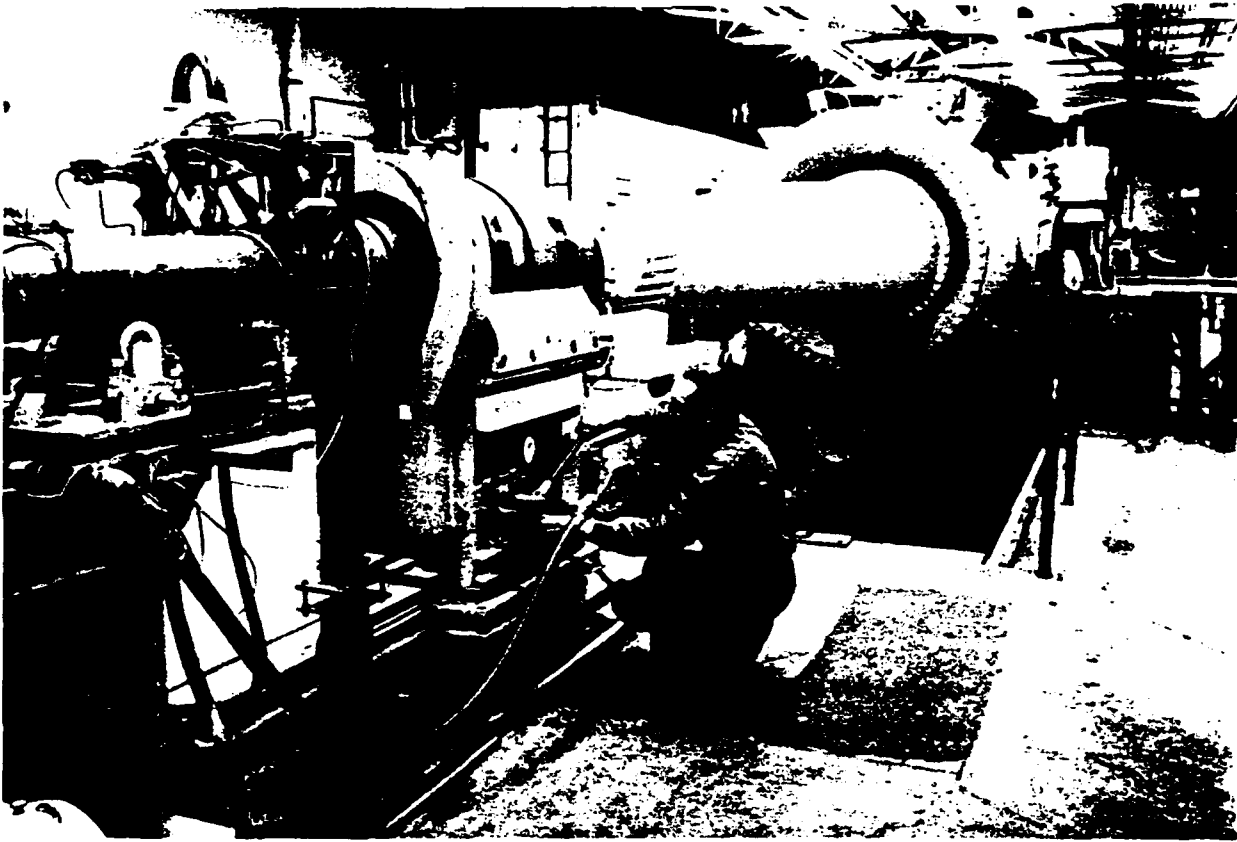


Figure 1 (a) CALSPAN'S 96-INCH SHOCK TUNNEL

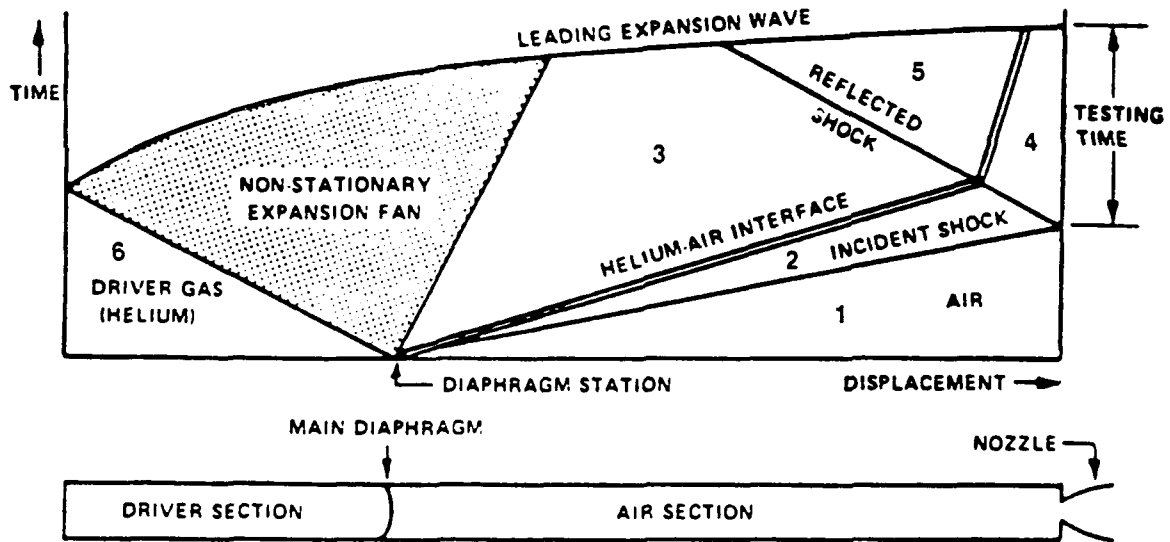


Figure 1 (b) WAVE DIAGRAM FOR TAILORED-INTERFACE SHOCK TUBE

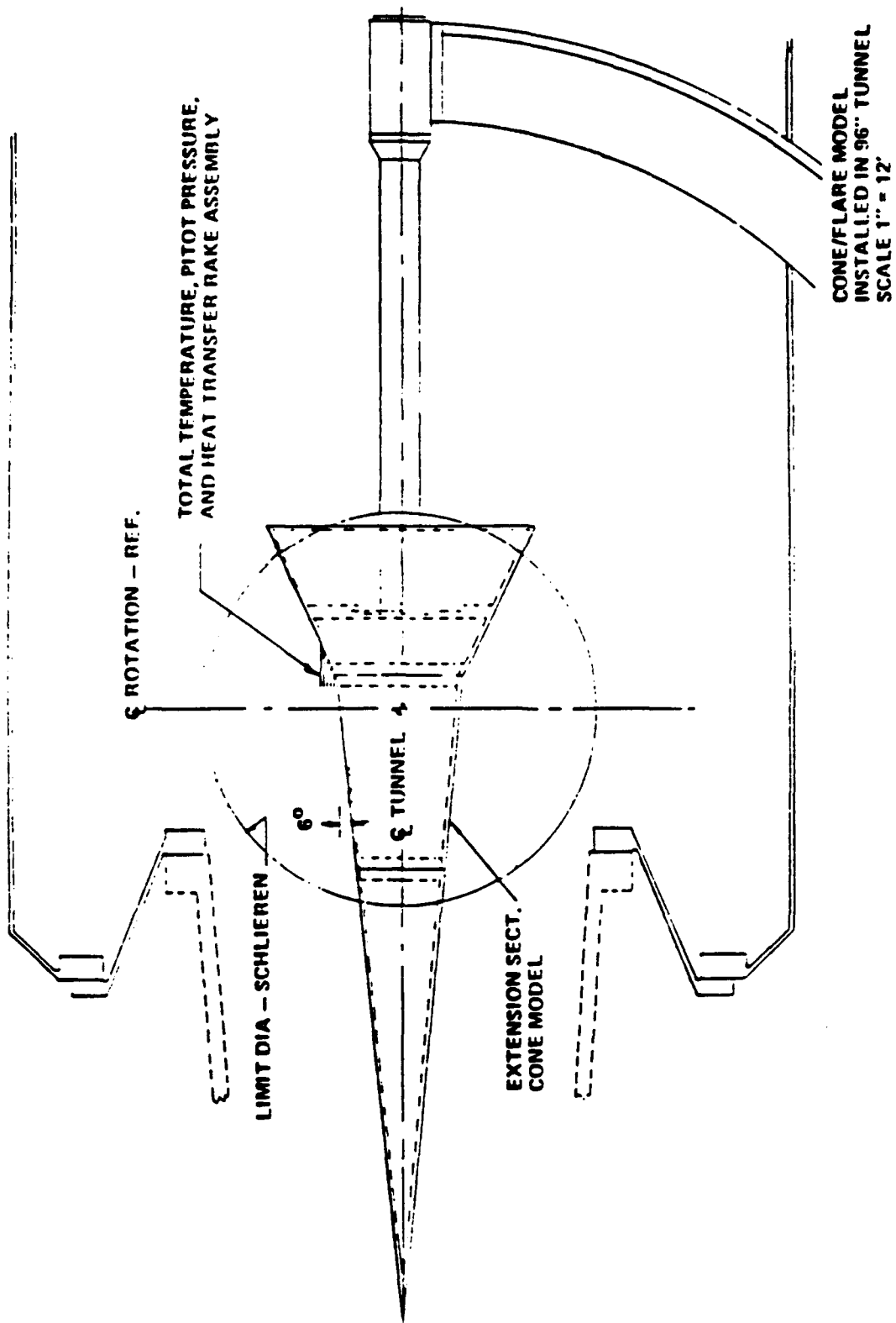


Figure 3 INSTALLATION DRAWING OF CONE/FLARE MODEL

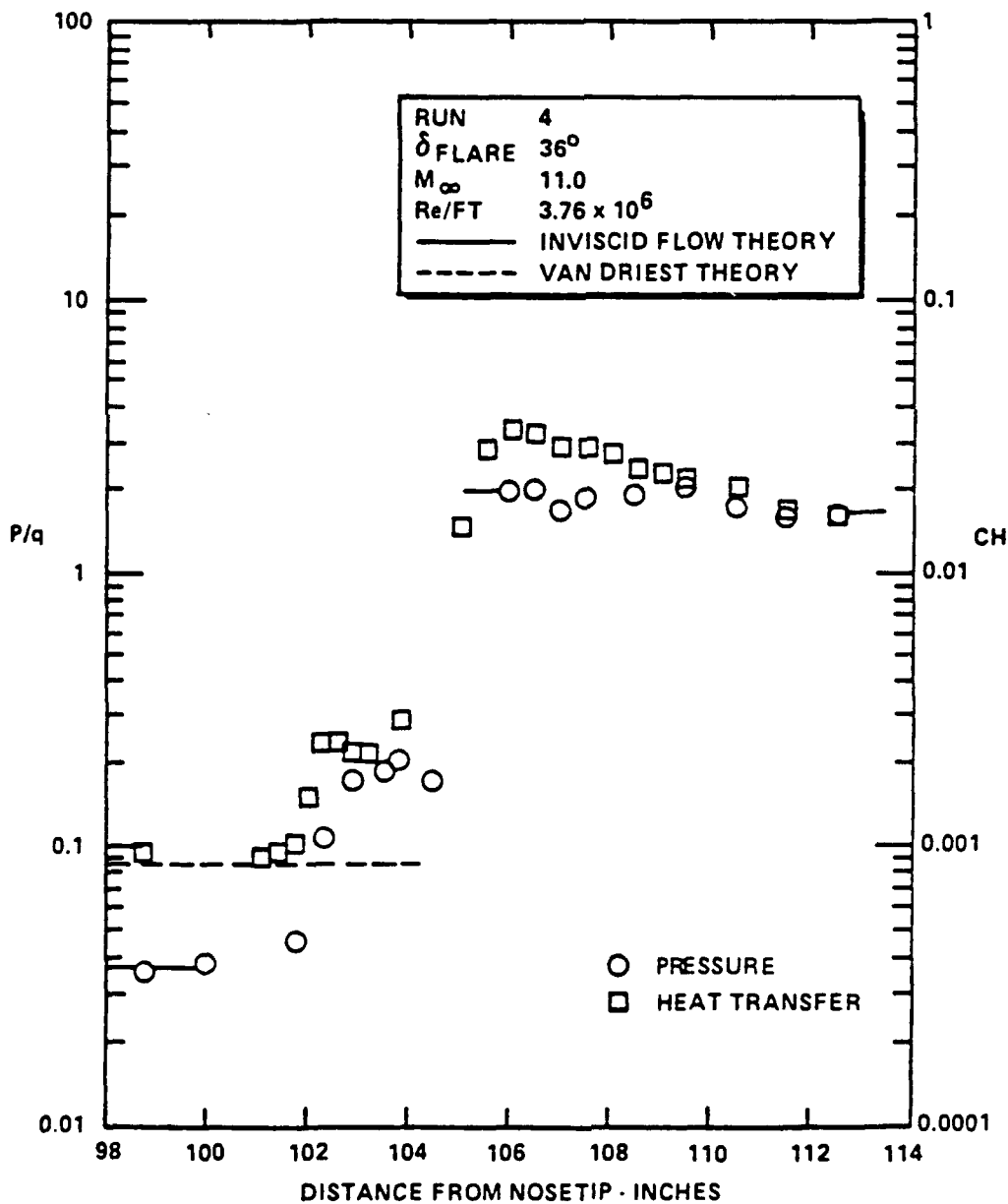
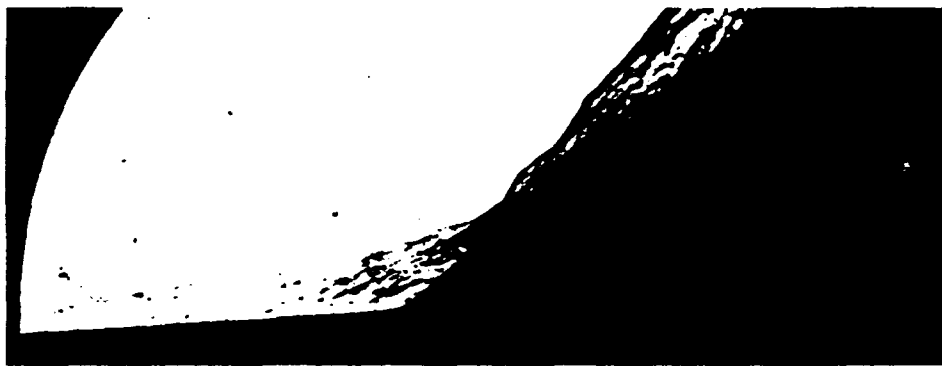


Figure 5 DISTRIBUTION OF PRESSURE AND HEAT TRANSFER IN SEPARATED FLOW OVER THE LARGE 6° CONE/36° FLARE CONFIGURATION

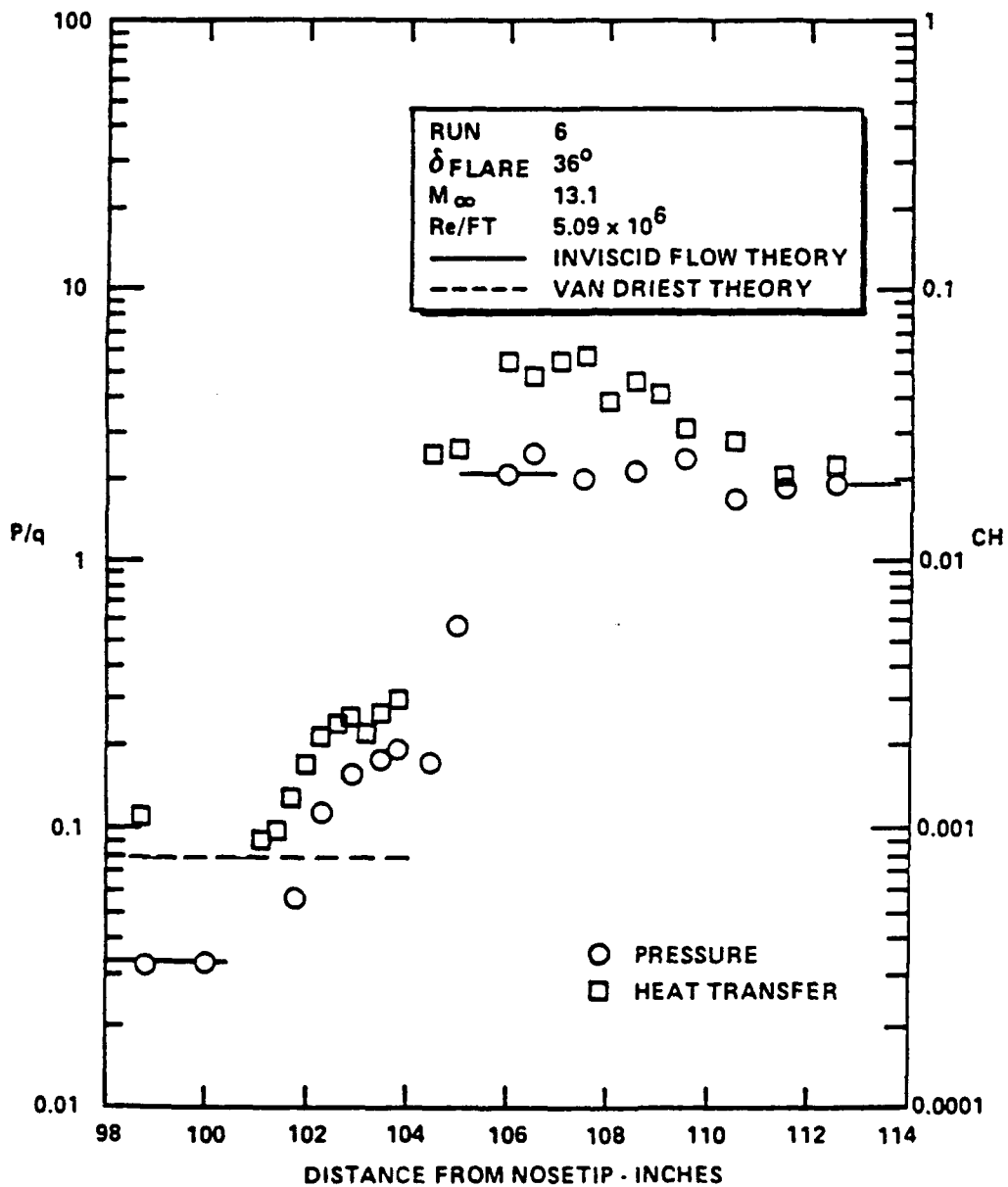
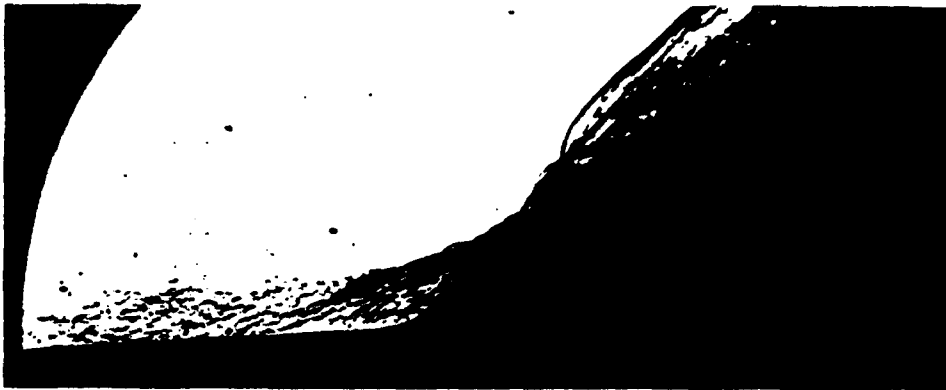


Figure 7 DISTRIBUTION OF PRESSURE AND HEAT TRANSFER IN SEPARATED FLOW OVER THE LARGE 6° CONE/ 36° FLARE CONFIGURATION



Figure 9 RAKE ASSEMBLY

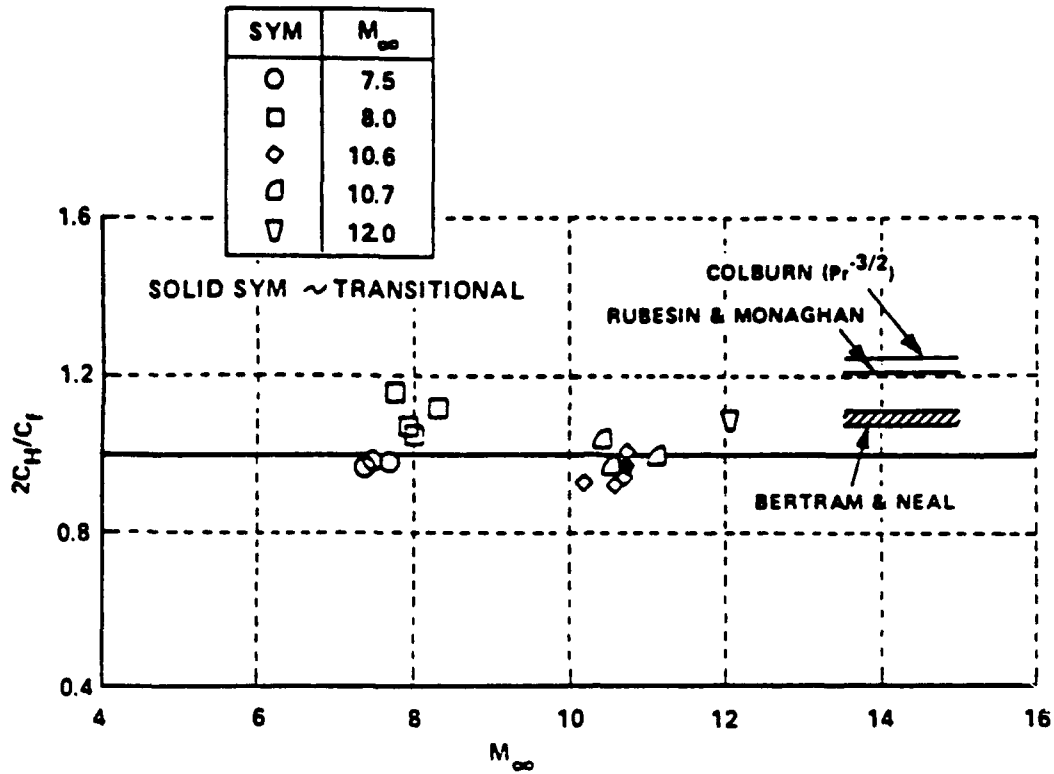


Figure 12 REYNOLDS ANALOGY FACTORS FOR TURBULENT
HYPERSONIC BOUNDARY LAYERS

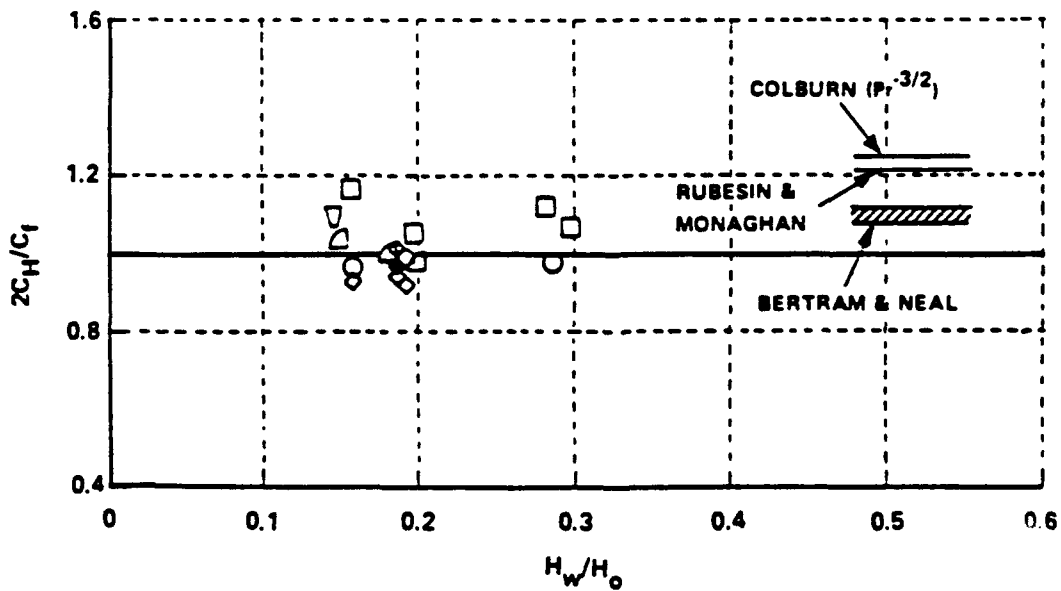


Figure 13 REYNOLDS ANALOGY FACTORS FOR TURBULENT
HYPERSONIC BOUNDARY LAYERS

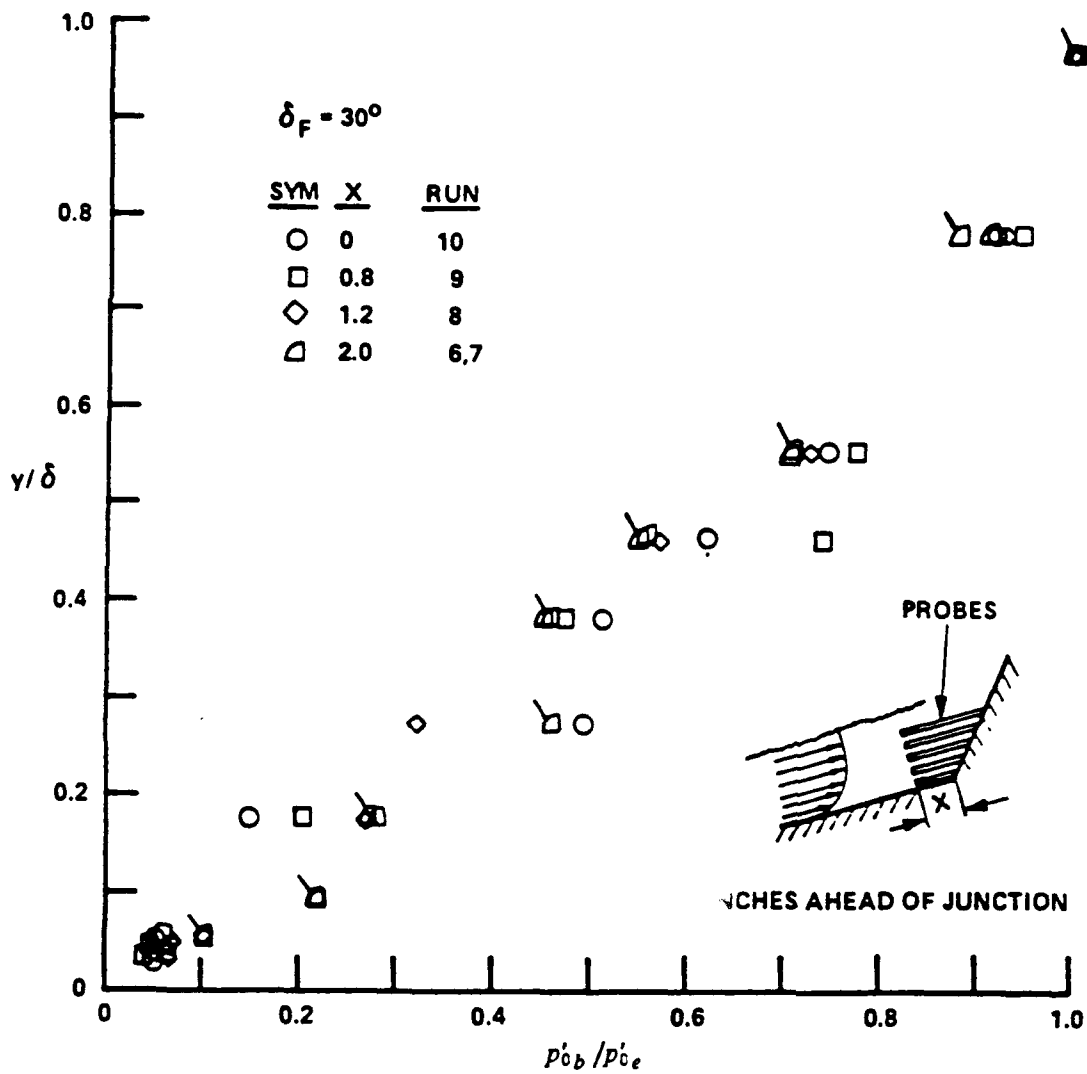


Figure 15 DISTRIBUTION OF PITOT PRESSURE ACROSS BOUNDARY LAYER UPSTREAM OF CONE/FLARE JUNCTION, 30° FLARE

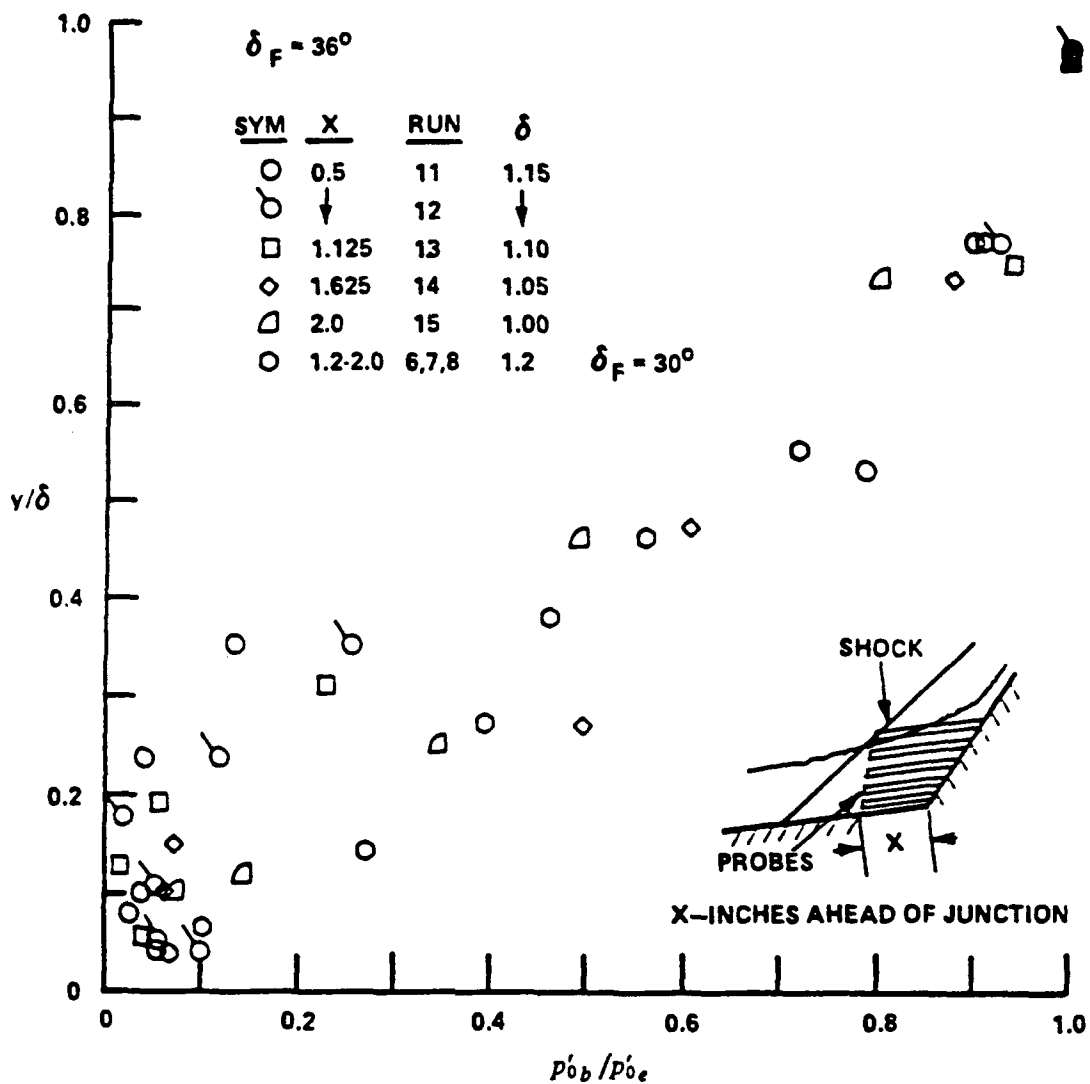


Figure 17 DISTRIBUTION OF PITOT PRESSURE ACROSS BOUNDARY LAYER UPSTREAM OF CONE/FLARE INTERACTION, 36° FLARE

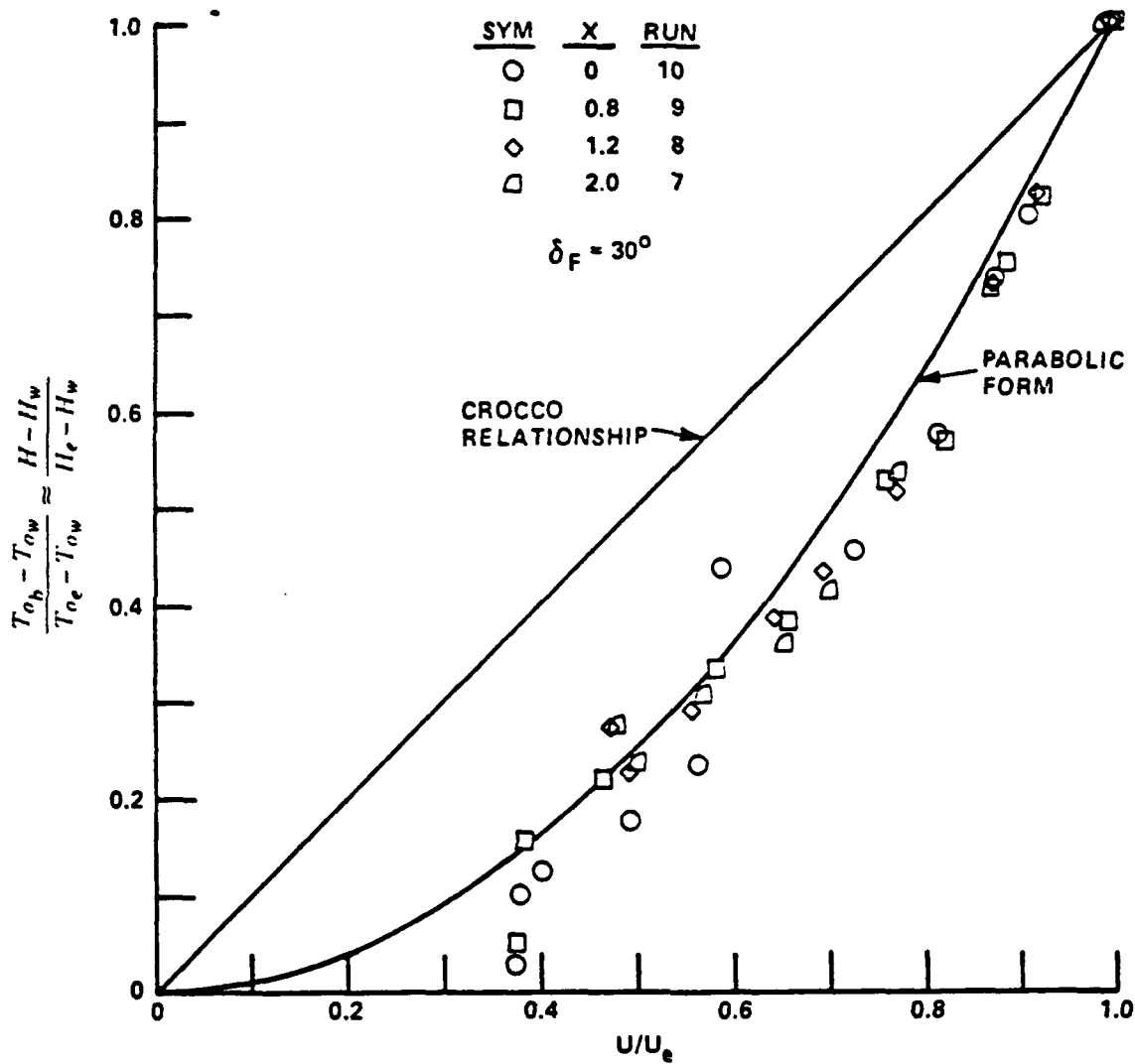


Figure 19 TOTAL TEMPERATURE AND VELOCITY MEASUREMENTS PRESENTED IN CROCCO FRAMEWORK

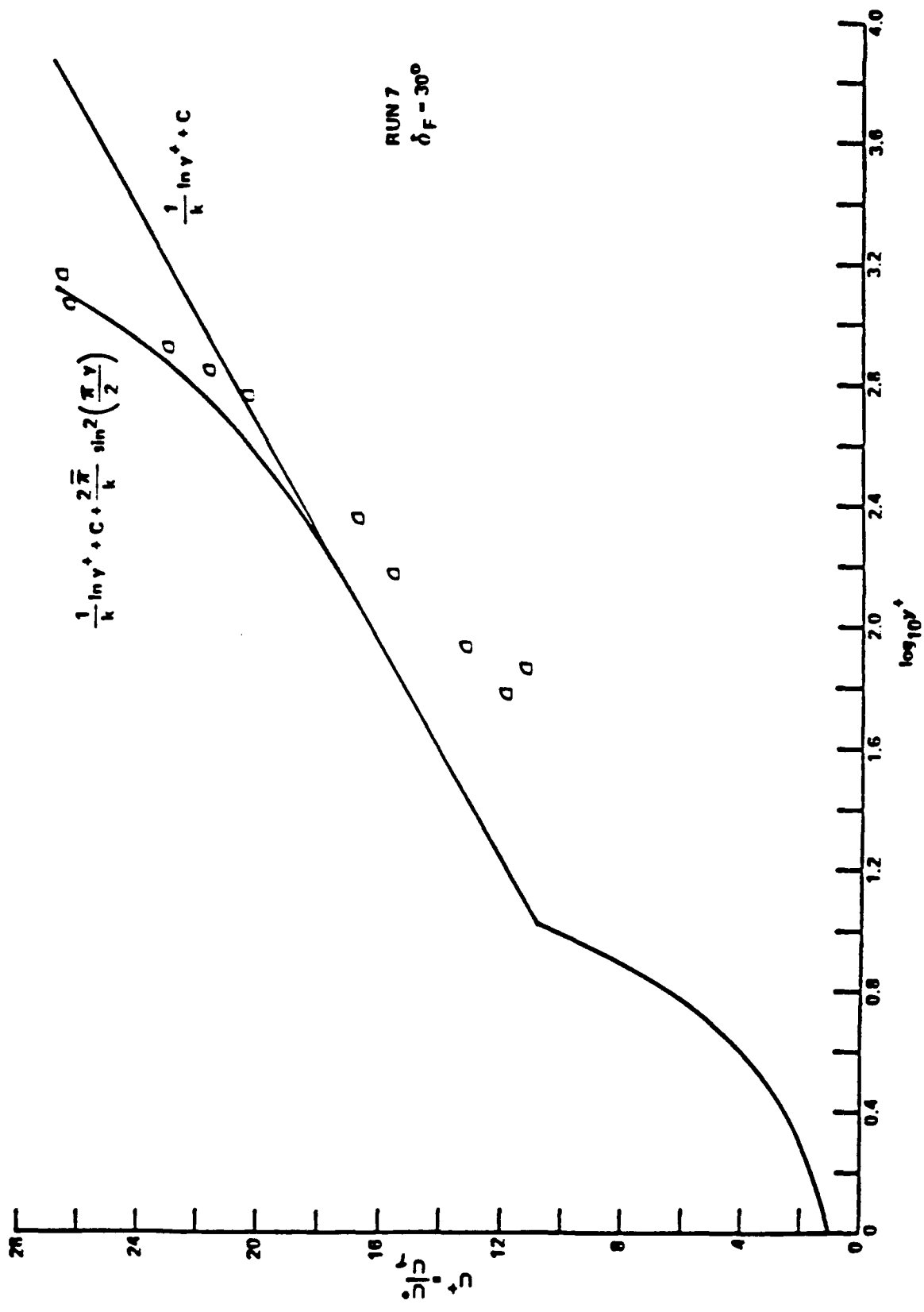


Figure 21 VELOCITY PROFILE MEASUREMENTS IN INCOMPRESSIBLE WALL COORDINATES

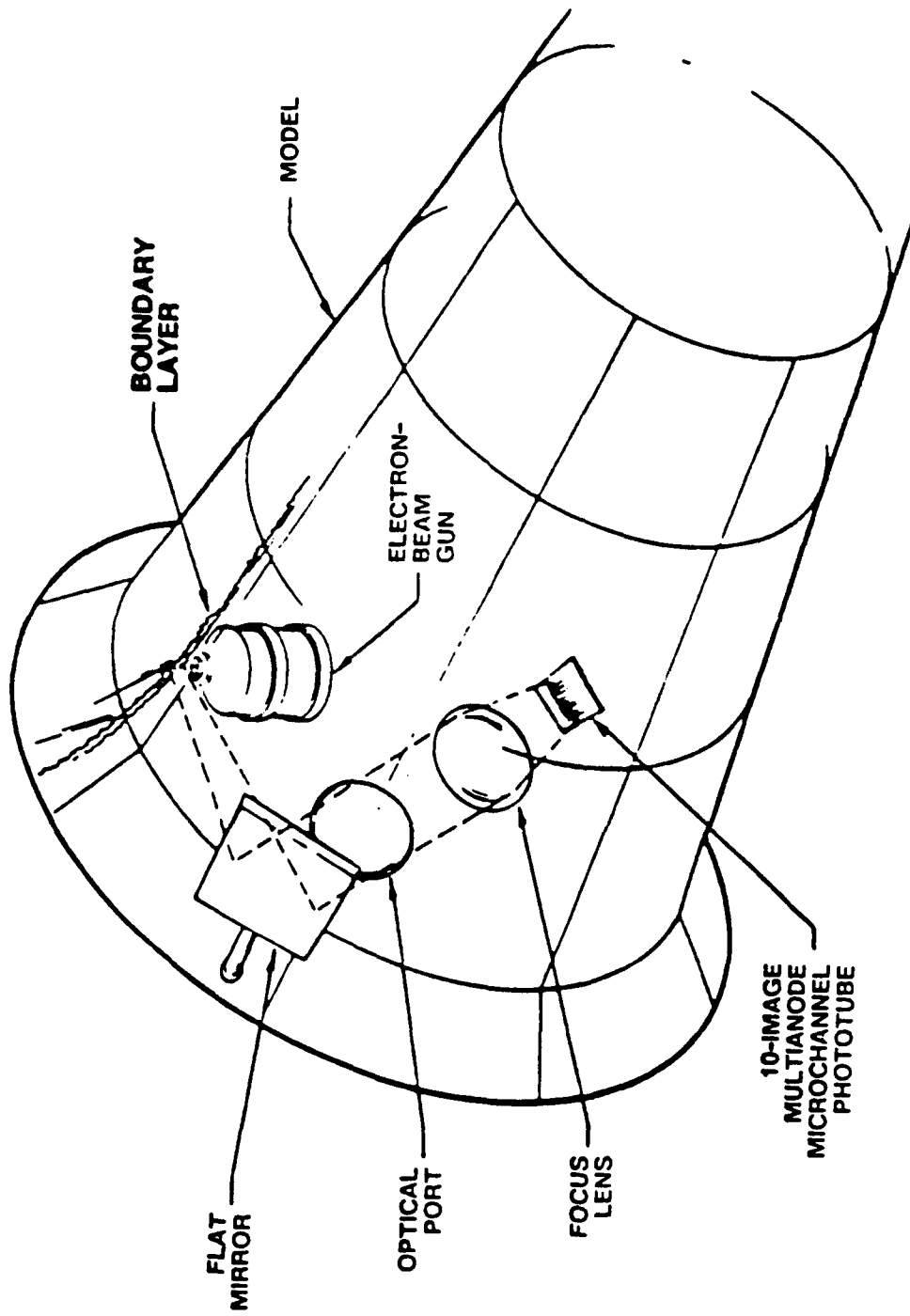


Figure 23 GENERAL LAYOUT OF ELECTRON-BEAM APPARATUS IN CONE/FLARE MODEL

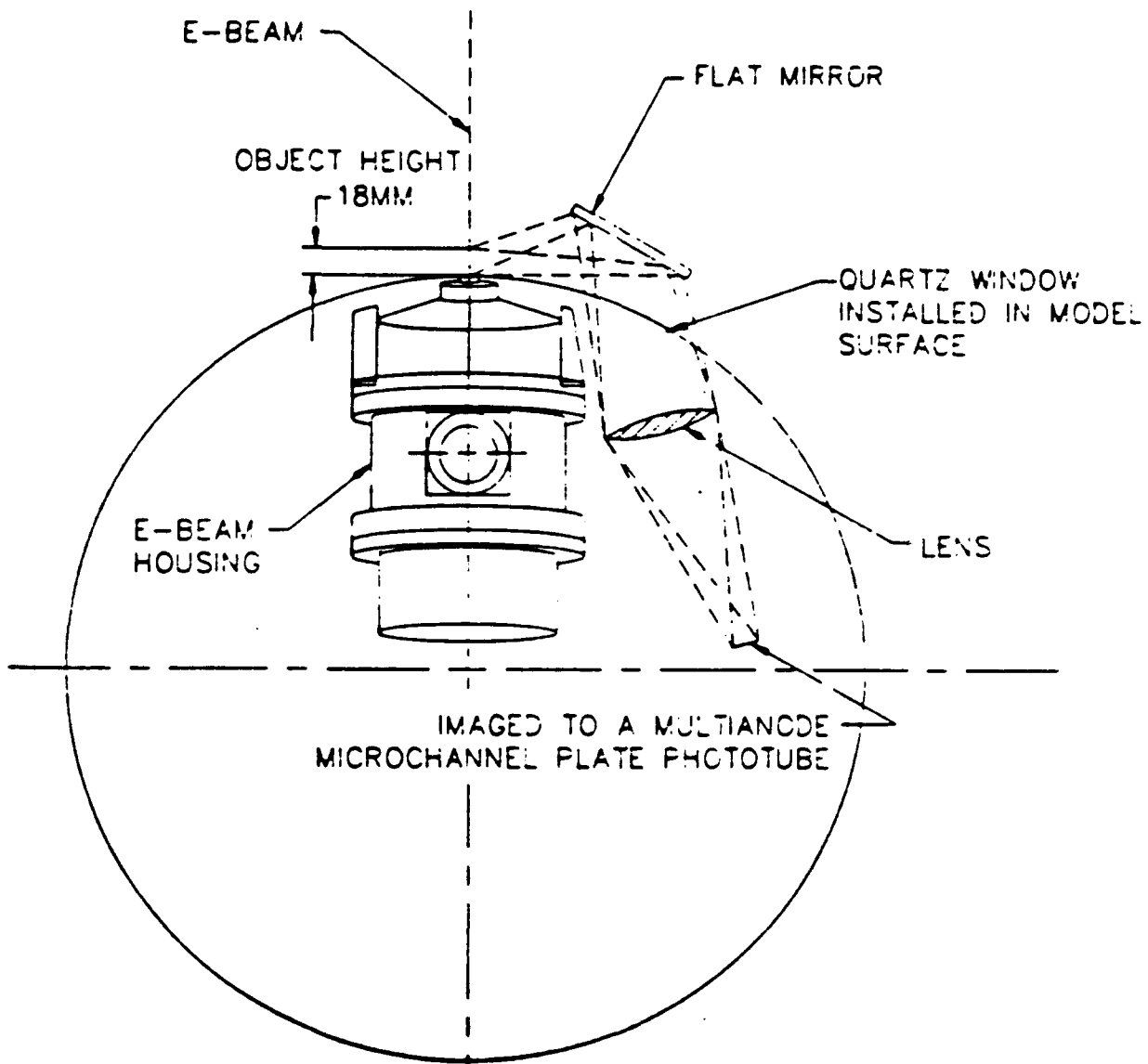


Figure 25 GENERAL LAYOUT OF OPTICAL SYSTEM FOR ELECTRON-BEAM DETECTORS

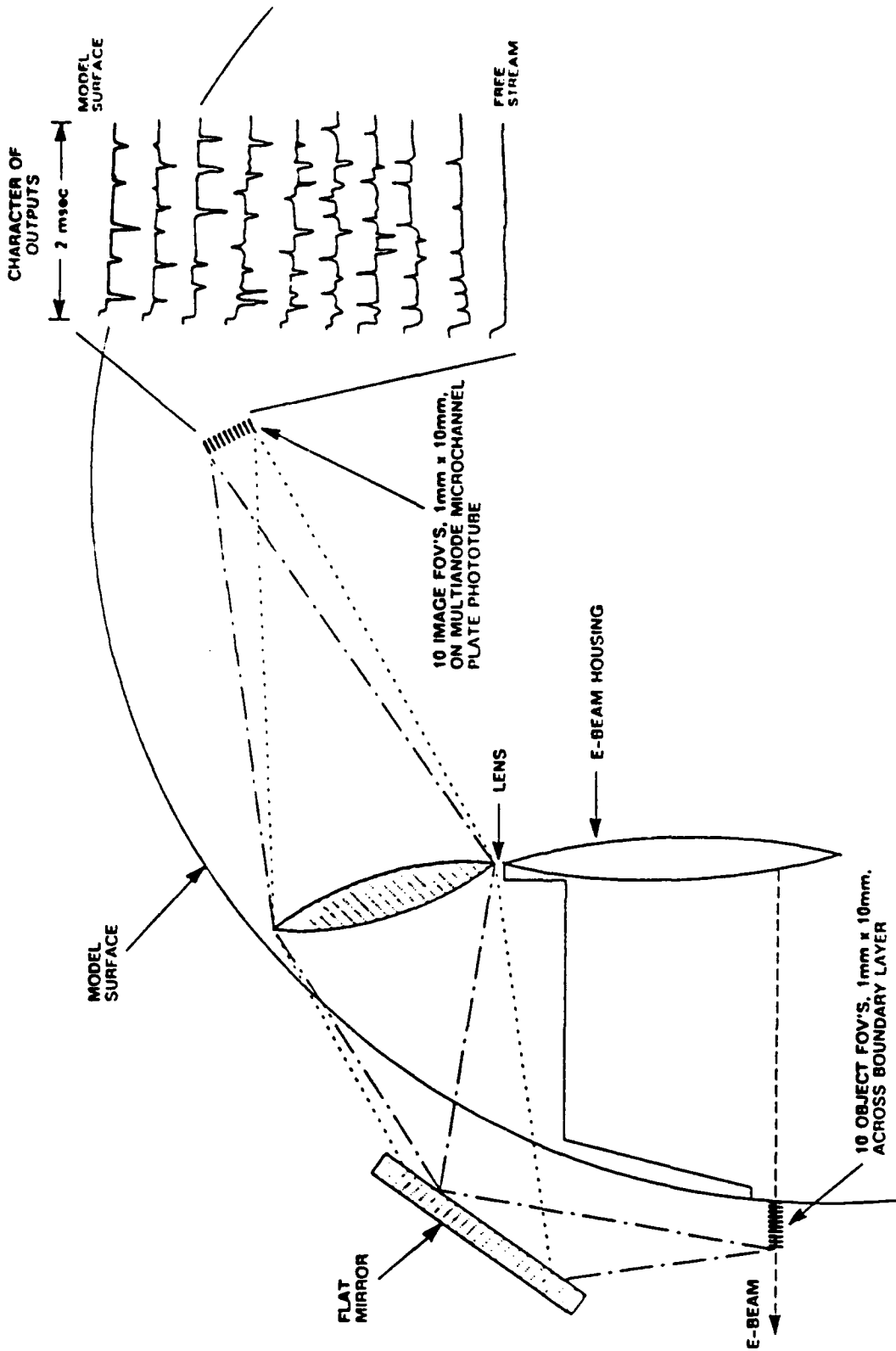


Figure 27 OPTICAL RESOLUTION OF DETECTOR SYSTEM

APPENDIX 3

AIAA PAPER NO. 92-4023

**A DATABASE OF AEROTHERMAL MEASUREMENTS IN
HYPERSONIC FLOW FOR CFD VALIDATION**



AIAA 92-4023
A Database of Aerothermal
Measurements in Hypersonic
Flow for CFD Validation

M.S. Holden
J.R. Moselle
Calspan Corporation
Calspan-University at Buffalo Research Center
Buffalo, NY

AIAA 17th
Aerospace
Ground Testing Conference
July 6-8, 1992 / Nashville, TN

A DATABASE OF AEROTHERMAL MEASUREMENTS IN HYPERSONIC FLOW FOR CFD VALIDATION†*

M. S. Holden **
J. R. Moselle ‡
Calspan Corporation
Calspan-UB Research Center
P.O. Box 400
Buffalo, NY 14225

Abstract

This paper presents an experimental database selected and compiled from aerothermal measurements obtained on basic model configurations on which fundamental flow phenomena could be most easily examined. The experimental studies were conducted in hypersonic flows in Calspan's 48-inch, 96-inch, and 6-foot shock tunnels during the past 25 years. The measurements selected for this database were assembled from a far larger data set by choosing only the measurements in laminar, transitional, and turbulent flows, which we believe are of the greatest value for code validation. A special computer program, "CUBDAT," was constructed to provide easy access to the measurements in the database as well as the means to plot the measurements and compare them with imported data. The database contains tabulations of model configurations; freestream conditions; and measurements of heat transfer, pressure, and skin friction for each of the studies selected for inclusion. The measurements tabulated in this database are divided into seven main areas. The first segment contains measurements in laminar flow emphasizing shock wave-boundary layer interaction. In the second segment, we present measurements in transitional flows over flat plates and cones. The third segment comprises measurements in regions of shock wave/turbulent boundary layer interactions. Studies of the effects of surface roughness of nosetips and conical afterbodies are presented in the fourth segment of the database. Detailed measurements in regions of shock/shock boundary layer interaction are contained in the fifth segment. Measurements in regions of wall jet and transpiration cooling are presented in the final two segments.

1. Introduction

1.1 Review of Key Aerothermodynamic Problems Associated With Hypersonic Flight

With the renewed interest in hypersonic vehicles, whose design requirements are more complex and sophisticated than the essentially ballistic systems that have been developed to date, there has come the realization that current predictive capabilities are inadequate in a number of important areas. While there has been a significant increase in computing power during the past decade, relatively little progress has been made in understanding and modeling the fundamental mechanisms that must be incorporated into the machine codes.

The high-altitude hypervelocity flight regime, where real-gas, nonequilibrium, viscous interaction, surface slip, and catalytic wall effects are important, is one area where the lack of measurements in high enthalpy ground test facilities is most evident. While, in the short term, (with sufficient funding) flight tests could help obtain measurements in the hypervelocity transition regime; the development of ground test facilities in which clean, reacting airflows at velocities of up to 20,000 ft/sec are generated should receive high priority. High-temperature high-Reynolds-number facilities are also required so that turbulent flows under ideal and real gas conditions on models in airflows at Mach numbers up to 16 can be studied.

In the flow regime between free molecular and continuum flow, where viscous interaction, non-equilibrium, surface slip, and catalysis are important, there is a real need to obtain detailed flowfield measurements in

† Major contributions to the assembly of this database were made by members of the CUBRC staff: Shirley Sweet, Joseph Kolly, Daniel Aiken, Kathleen Rodriguez, John Weglian and Mark Preischel.

* This work was supported by the U.S. Air Force and the National Aeronautics and Space Administration under a number of contracts and grants as specified herein. This paper is declared a work of the U.S. Government and is not subject to copyright protection in the United States.

** Staff Scientist; Associate Fellow, AIAA

‡ Principal Mathematician

such flow properties with earlier measurements have been made. Good agreement was found between the measurements and calculations using Holden's⁴ integral analyses of these flows. Solutions to the time-dependent Navier-Stokes equations were found to be in good agreement with the measurements for attached or mildly separated flows, but they significantly underpredicted the size of well separated interaction regions.

2.3 Laminar Separated Flows on Curved Compression Surfaces, $M = 1.4$ [NCURVSURF]

This research was sponsored by the Air Force Office of Scientific Research under Contract No. F33615-67-C-1298 and was published as "Theoretical and Experimental Studies of the Shock Wave-Boundary Layer Interaction on Curved Compression Surfaces," paper presented at the ARL Symposium on "Viscous Interaction Phenomena in Supersonic and Hypersonic Flow," WPAFB, OH, May 1969.

In this experimental study, we explored the conditions under which the inertial forces generated by surface curvature become important. Beginning with a flat plate/wedge compression surface, surface curvature was introduced by interposing cylindrical sections between the flat plate and wedge. A series of circular cylindrical sections with different radii of curvature was tested; each cylindrical section contained segments that could be added or subtracted to change the degree of turning. The position and angle of the wedge was adjusted so that it formed a continuous surface tangential to the trailing edge of each cylindrical segment.

The measurements were made in Calspan's 48-inch shock tunnel at freestream Mach numbers 14.0 and 14.5 and Reynolds numbers of 7.2×10^4 and 1.8×10^5 /foot, respectively. Reservoir pressures of 1,500 and 4,200 psia were used at a common stagnation temperature of 5330°R. The models used in this study consisted of a flat plate followed by a circular cylindrical surface that was terminated into a second flat plate. Cylindrical surfaces with radii of curvature of 6, 12, and 20 inches were inserted between the flat plate and ramp in the program, and these surfaces were constructed in segments so that the degree of turning could be varied. The second flat plate, or ramp, was supported so that the slope at the junction

between the curved surface and the ramp was continuous. The length of the leading edge of the flat plate could be varied to obtain flat plate lengths from 12 to 17 inches.

The flat plate, cylindrical sections, and ramp were fully instrumented with skin friction, heat transfer, and pressure transducers. Pitot and cone pressure traverses were also made to obtain an estimate of the pressure gradients normal to the surface in the separation and reattachment regions. Figure 2.3 shows a photograph for the model used in this experimental study and the instrumentation layout on the model. Also shown are a typical segment of the test matrix and a set of measurements made in the program. In these flows, the first indication that flow separation was to occur was provided by the skin friction measurements on the compression surface; the skin friction was first observed to be negative on the surface downstream of the flat plate. On the compression surfaces with large radii of curvature, the incipient separation condition could not accurately be detected by observing the first occurrence of an inflection point in the pressure distribution or a change in the form of the heat transfer distribution. The static pressure distributions, evaluated from the pitot and cone pressure measurements across the boundary layers in the separation and reattachment regions, indicated that the normal pressure gradients were of the same magnitude as those in the streamwise direction. Although the experiments were conducted for a range of ratios of boundary layer thickness to radius of curvature as used by Kuehn⁵ and Sterrett and Emery⁶, we found that incipient separation was far less sensitive to surface curvature than indicated in these earlier studies. This, we believe resulted from the structure of the laminar boundary layer in hypersonic flow over highly cooled walls, where the streamwise distances for a surface disturbance to propagate to the edge of the boundary layer (where most of the momentum is concentrated) are greater than the length of the curved surface.

2.4 Laminar Separated Flows on Flat Plate/Wedge, in Low Re Flow, $M=11$ to 20 [NINCIPSEP]

This research was sponsored by the Air Force Office of Scientific Research under Contract No. AF33(615)-1205 and was published as "Theoretical and Experimental Studies of

while monitoring both the longitudinal and spanwise properties of the model. Although increasing the model span from 1 foot to 1.5 feet did not measurably influence the properties of the attached interaction regions, it did cause a small increase in the size of large separated regions. However, further increasing the model span to 2 feet had little additional effect, and the addition of side fences to this latter configuration did not affect the flow. It was found that a uniform distribution of properties across the center span of the model does not necessarily imply that the measurements are free from span effects. Also, side fences should be used with care, because adding them to some configurations can cause as much flow distortion as not using them.

In the experimental studies of shock wave/boundary layer interaction on the highly cooled, sharp flat plate/wedge models, which were performed at Mach numbers of 14 to 20 and at unit Reynolds numbers from 2,200/inch to 14,000/inch, we found that the upstream influence on the wedge in attached flows was extremely small. However, when separation was promoted, the interaction moved forward very rapidly as the wedge angle increased. The abrupt change in the extent of the upstream influence was in marked contrast with the character of laminar boundary layers in supersonic flow, where the upstream influence increased uniformly with wedge angle in both attached and separated flows. The length of the separated region was found to decrease with increasing freestream Mach number and decreasing unit Reynolds number. A plateau pressure region was found in all well separated flows, and the plateau ratio was correlated in terms of $\chi_{E L}^{1/2}$. The incipient separation condition was determined at each freestream condition from the skin friction, heat transfer, and pressure measurements. The skin friction measurements verified the separation criteria, based on characteristic changes in heat transfer and pressure distributions with wedge angle, which had been proposed in earlier studies. We found that these measurements of the incipient separation condition correlated in the form $M\theta_{incip} = 4.3 \chi_{E L}^{1/2}$.

The study of the interaction regions on the blunted flat plate/wedge was performed at a freestream Mach number of 19.8 and unit Reynolds numbers of 8,700/inch and 2,055/inch for a series of leading edge thicknesses (from 0.007 to 1.2 inches) and shapes (cylindrical and flat) to obtain conditions on the basic flat plate from the viscous to the bluntness-dominated

regime ($0.08 < \chi_{E L} / K_{E L}^{2/3} < 2$). The measurements of skin friction, heat transfer, and pressure made in the attached flow over the blunted flat plates agree well with the theory of Cheng, et al.³ from the displacement to the bluntness-dominated regime ($2 > \chi_{E L} / K_{E L}^{2/3} > 0.08$). For well separated flows, increasing the leading edge bluntness for $\chi_{E L} / K_{E L}^{2/3} > 0.5$ slightly increased the size of the separated region, whereas for $\chi_{E L} / K_{E L}^{2/3} < 0.5$, an increase in the bluntness caused a marked decrease in the length of the separated flow. A well separated region in these flows was always characterized by a plateau pressure region. The plateau pressure ratio decreased with increased bluntness, and it was found that the measurements correlated in the form $p_{plateau}/p_0 (K_{E L} / \chi_{E L}^2)^2$ versus $\chi_{E L} / K_{E L}^{2/3}$. The pressure, heat transfer, and skin friction on the wedge in both attached and separated flows were markedly reduced by leading edge bluntness. Thus, in the design of compression surfaces, a compromise must be reached between protecting the leading edge and recovering as much pressure as possible on the ramp. We found that, in flows strongly influenced by leading edge bluntness, the skin friction measurements were the only accurate method of determining incipient separation, although the heat-transfer measurements still provided a qualitative separation criterion. The wedge angle required to cause incipient separation was reduced by leading edge bluntness, although the trend was weak; the measurements correlated in the form $M_{incip} (K_{E L} / \chi_{E L}^2) = 4.34 (\chi_{E L} / K_{E L}^{2/3})^{-7/5}$.

3. Measurements in Transitional Hypersonic Flows

3.1 Introduction

Measurements tabulated in this segment of the database were obtained from programs designed to examine the structure of transition regions in regions of constant, adverse, and favorable pressure gradients in hypersonic flow. The first set of measurements was made on flat plates to obtain laminar transitional and turbulent flows for a large range of freestream Mach numbers and Reynolds numbers. The measurements of heat transfer and skin friction distributions through the transition regions provide a valuable resource to examine the code predictions of length and structure of constant pressure transition regions. The measurements

in best overall agreement, it overpredicts the heat transfer and skin friction in the low hypersonic Mach number regime, where the agreement between the measurements and the Spalding-Chi theory¹¹ is best. Because only surface measurements were made, a question remains on the magnitude of the distance downstream of the maximum heating point, where all the transition process remnants were dissipated. While this is unimportant in our studies at the lower Mach numbers, where we have measurements at many hundreds of boundary layer thicknesses downstream of the point of maximum heating, at Mach numbers 11 and 13, we were forced to ask the question: Does the disagreement between the measurements and the Spalding-Chi theory result from the persistence of turbulent remnants in the flow, a low Reynolds number effect, or an inadequacy of the theory? Only boundary layer surveys will provide a complete answer on the relaxation distance of a transitional boundary layer from the maximum heating point to the point where the boundary layer is fully turbulent.

3.3 Laminar, Transitional, and Turbulent Flows on Sharp and Blunted Cones, M=11 to 13 [BDYFIXTR]

This research was sponsored by the Air Force Office of Scientific Research under Contract No. F44620-76-C-0003 and was published as "Experimental Studies of the Effects of Asymmetric Transition on the Aerothermal Characteristics of Hypersonic Blunted Slender Cones," AIAA Paper No. 85-0325, January 1985.

This experimental study was conducted to investigate the effects of asymmetric boundary layer transition on the aerothermal characteristics of slender blunted cones at angle of attack in hypersonic flow. In this study, which was conducted in Calspan's 96-inch shock tunnel at Mach numbers of 11 and 13, simultaneous measurements of force, heat transfer, and pressure were made to examine the effects of asymmetric transition induced by angle of attack, and by roughness and steps and gaps in the frusta and nosetip, on the aerodynamic stability and asymmetric heating loads generated over the cones. Figure 3.3 shows a photograph for the model used in this experimental study and the instrumentation layout on the model. Also shown are a typical segment of the test matrix and a set of measurements made in the program. Observations of the mechanisms of boundary layer transition in these studies, made with spark-source photography, revealed the presence of

ordered, "wave-like" instabilities preceding the massive breakdown of the laminar boundary layer. Our measurements of the Reynolds numbers at which boundary layer transition occurred were found to be in good agreement with those from flight tests and ballistic range studies. The studies of the effects of asymmetric transition induced by angle of attack demonstrated that transition moved first onto the leeside of sharp or slightly blunted cones, inducing a destabilizing effect; for cones with bluntness ratios (r/R_b) greater than 12%, transition occurred first on the windward ray. For "wind-fixed" transition, this has resulted in center-of-pressure (C_p) movements on the order of 1%. The studies of "body-fixed" transition regions demonstrated that "wedge-shape" transition regions could be induced with relative ease by small gouges in the spherical nosetip, or by surface roughness near the nosetip. In contrast, gaps in the surface of the frustum were not found to be effective trips. Our studies indicated that the magnitude of the destabilizing forces was relatively independent of the tripping mechanism. Typical forces and moments associated with such regions were $\Delta C_n = -1.8E-3$ and $\Delta C_m = 6E-3$. Such force levels were in general agreement with calculations based on the increased pressures and skin friction forces induced in the asymmetric transition regions.

3.4 Laminar, Transitional, and Turbulent Flows on Curved Ramp, M=8 to 11*

3.5 Attachment-Line Transitional Flow on Swept Cylinder Configurations, M=11 to 16*

3.6 Transition and Relaminarization on Flat Plate/Expansion Cone, M=11 to 13*

4. Measurements in Regions of Shock Wave/Turbulent Boundary Layer Interaction in Hypersonic Flow

4.1 Introduction

In hypersonic flow regions of wedge- or shock-induced shock wave/turbulent boundary layer interaction provide one of the most stringent tests for turbulence modeling in solutions to the full-time average Navier-Stokes equations. In these flows, correctly describing

* Currently in Preparation

measurements on the model surface were made, and schlieren photographs of the flowfield were taken, for a series of incident shock strengths and turning angles of the compression surface so that attached, incipient separated, and well separated turbulent interaction regions could be studied at each freestream condition. We investigated whether there was a reversal in the variation of the length of a separated interaction region, as well as a pressure rise to induce incipient separation, with Reynolds number (Re_δ). The model contained over 200 instruments, distributed over three leading edge plates, a center section, and a flap or wedge section. Because of the severity of the fluctuating flowfield in the reattachment region under some conditions, the skin friction gages were torn apart, again emphasizing the importance of the reattachment region in both the thermal and mechanical design of hypersonic reentry vehicles. Figure 4.3 shows a photograph for the model used in this experimental study and the instrumentation layout on the model. Also shown are a typical segment of the test matrix and a set of measurements made in the program.

Detailed heat transfer and pressure measurements were made in regions of shock- and wedge-induced turbulent interaction regions. These measurements demonstrated a reversal in the trend of incipient separation with Reynolds number, postulated previously on the basis of experiments for widely different model configurations and test conditions. It is believed that this trend reversal results directly from changes that occur in the velocity profile downstream of transition such that N (in the relationship $N = N(Re_\delta)$) decreased downstream of transition until an equilibrium boundary layer was established, when N increased slowly with Reynolds number. Correlations of the characteristics of these interaction regions are presented in terms of model configuration and freestream conditions. Solutions to the Navier-Stokes equations were found to be in surprisingly good agreement with the measurements, considering the problems involved in describing the development of turbulence through these interaction regions. However, further detailed profile measurements are required to assist in the development of accurate models to describe turbulence in regions of shock wave/turbulent boundary layer interaction.

4.4 Attached and Separated Induced By Skewed and Swept Incident Shocks. $M=11$ [SWEPTSKU]

This research was sponsored by the Air Force Office of Scientific Research under Contract No. F49620-82-C-0026 and was published as "Experimental Studies of Quasi-Two-Dimensional and Three-Dimensional Viscous Interaction Regions Induced by Skewed Shock and Swept-Shock Boundary Layer Interaction," AIAA Paper No. 84-1677, June 1984.

In this experimental study, measurements were made to examine the characteristics of two- and three-dimensional flows induced by: (1) skewed oblique-shock/turbulent boundary layer interaction, and (2) the three-dimensional viscous/inviscid interaction in the corner formed between a flat plate and a vertical fin. Both studies were conducted at Mach 11 for unit Reynolds numbers of up to 50×10^6 , under highly cooled wall conditions. Detailed distributions of heat transfer and pressure were obtained and schlieren photographs taken for a range of model configurations to examine both attached and separated flows. We explored the basic mechanisms associated with three-dimensional turbulent boundary layer separation in high speed flows, with special emphasis placed on the large heat transfer rates and gradients developed in the separation and reattachment regions of these flows. Experimental measurements were made to extend the simple semi-empirical prediction methods to the turbulent hypersonic highly cooled wall flow regime, where no previous data existed, as well as to provide measurements to compare later with solutions to the Navier-Stokes equations. Figure 4.4 shows a photograph for the model used in this experimental study and the instrumentation layout on the model. Also shown are a typical segment of the test matrix and a set of measurements made in the program.

The principal objective of the skewed interaction studies was to determine the effects of crossflow on the size and properties of separated interaction regions. Keeping the strength of the interaction constant, the degree of crossflow was varied by skewing the oblique shock between 0 and 45° to the flat plate's leading edge. These studies demonstrated that crossflow has little effect on the scale and properties of the separated interaction regions; this contrasts with the findings of Settles and Perkins¹², who, in an

$\times 10^6$ to examine surface roughness effects in hypersonic flow. Measurements were made to examine the effects of roughness shape and spacing on heat transfer to and skin friction of slender models in hypersonic flow. The slender cone model was coated and instrumented successively with six different patterned surfaces and the corresponding heat transfer, skin friction, and pressure instrumentation. The rough surface was designed so that measurements could be obtained from the closest to the most widely spaced roughness packing of practical interest ($2.5 < A_p/A_s^{-1} < 25$), spanning the "peak" in effective sand-grain roughness. The roughness height, position of the instrumentation, angle of attack of the model, and freestream conditions were selected so that the measurements covered the fully rough to the smooth regimes. Figure 5.6 shows a photograph for the model used in this experimental study and the instrumentation layout on the model. Also shown are a typical segment of the test matrix and a set of measurements made in the program.

The shape of the roughness elements and the spacing between the roughness elements have a large effect on the heat transfer to and skin friction of the surface. Correlations are presented showing the monotonic decrease in roughness heating with increased spacing and decreased bluntness of the roughness elements. This contrasts with the multi-valued relationships exhibited in correlations of the low-speed measurements. Both $(A_p/A_s)^{-1}$ and $D/K (A_{ws}/A_p)^{4/3}$, the shape/spacing parameters against which the measurements were plotted, gave a good correlation of the data. None of the patterned rough surfaces examined induced heating rates more than 10% larger than those of sand-grain surfaces with the same roughness height, which contrasts with up to 100% enhancement predicted using the Dirling correlation of low-speed measurements. The strong decrease in heating enhancement with roughness spacing exhibited in our measurements and predicted with good accuracy by simple methods would, for roughness spacings and shapes typical of carbon/carbon surfaces, result in heating enhancement on the order of 50% of the sand-grain value. Measurements on models with discontinuous change in surface roughness indicated that, in hypersonic flow, turbulent relaxation is an important effect. These studies, coupled with the theoretical studies of Finson⁷, suggest that compressibility effects are important in high speed flows over rough, highly cooled surfaces.

6. Shock/Shock Interaction Studies in Hypersonic Flow

6.1 Introduction

The heat transfer rates generated in regions of shock/shock interaction can provide one of the most serious problems in the design of the thermal protection systems for a hypersonic ramjet-propelled vehicle. Both on the cowl lip and inside the engine on the stagnation line of the strut injectors, heat transfer rates of the order of 25 times those in the undisturbed stagnation region can be expected in regions of shock/shock interaction. In this segment of the database we present detailed heat transfer and pressure measurements in shock/shock interaction regions over two-dimensional cylinders and hemispherical nosetips. These studies were conducted at Mach numbers from 6 to 19 for a range of unit Reynolds numbers to create laminar and turbulent shear layer conditions in the shock/shock interaction regions. The prediction of these flows is made more complicated by the requirement for an accurate model for the transition of the shear layer ahead of the surface in both type III and type IV interaction regions. For fully laminar flows, this complication does not exist; but, in both laminar and turbulent flows, an accurate solution can be obtained only by careful and detailed gridding of the shear layer and the region close to jet or shear layer impingement of the body. The large range of freestream conditions, coupled with the highly spatially resolved nature of the measurements, makes these data a unique resource for code validation.

6.2 Detailed Heat Transfer and Pressure Measurements in Regions of Shock/Shock Interaction over Swept and Unswept 2-D Cylinders, M=6 to 19 [SHK-SHK]

This research was supported by the National Aeronautics and Space Administration under Grant No. NAS1-17721 and was published as "Studies of Aerothermal Loads Generated in Regions of Shock/Shock Interaction in Hypersonic Flow," AIAA Paper No. 88-0477, January 1988.

Detailed measurements of the distribution of heat transfer and pressure were made in the peak heating regions around a cylinder for a number of shock/shock interactions

7. Wall-Jet/Window Cooling Studies

7.1 Introduction

Understanding and predicting the mixing between a cold supersonic walljet and a hot hypersonic freestream is a problem of fundamental importance in the design of ramjet combustors and the externally cooled windows in the seeker heads of hypersonic interceptors. In hypervelocity flows, there appears to be a strong decrease in the mixing when the convective Mach number between the two flows approaches and exceeds Mach 1, which is believed to be associated with turbulent compressibility effects. To examine this mixing problem, measurements in high temperature hypersonic flows with supersonic convective Mach numbers and freestream and injector gases with dissimilar molecular weights are required. In this segment of the database, two sets of measurements are presented that will provide data for code comparison to evaluate the effects of compressibility and turbulent nonequilibrium. In the first data set, detailed measurements of heat transfer are presented in the constant pressure flow downstream of a Mach 3 injector. Also for this configuration, measurements are presented with the mixing region perturbed by the impingement of an oblique shock. The measurements on the HEDI configuration provide detailed heat transfer and pressure measurements in the externally cooled flow typical of a large interceptor window. In both these studies, the correlation of heat transfer measurements in terms of the major non-dimensional parameters indicates that significant convective Mach number and the specific heat of the injectant are important parameters controlling the magnitude and length of the cooling.

7.2 Oblique Shock/M=3 He Wall-Jet Interaction on Flat-Plate Injector Model, M=6 to 8 [SLOT 080, SLOT 120]

This research was supported by the National Aeronautics and Space Administration under Grant No. NAG1-790 and was published as "Experimental Studies of Shock Wave/Wall Jet Interaction and Hypersonic Flow," AIAA Paper No. 90-607, January 1990.

An experimental study was conducted to examine the interaction between a planar shock wave and hypersonic flow. The experimental studies were conducted in the 48-inch shock tunnel at Calspan at a freestream Mach number

of 6 and a Reynolds number of 35×10^6 based on the length of the model. The Mach 3 planar wall jet was generated from 40 transverse nozzles (0.08 and 0.12-inch height) producing a film that extended the full width of the model. The nozzles were operated at pressures and velocities matching the freestream, as well as at conditions where the nozzle flows were over- and under-expanded. A two-dimensional shock generator was used to generate shocks of total turning of 11, 16, and 21°, which were impinged at a series of stations downstream of the nozzle exits. Detailed measurements of heat transfer and pressure were made both ahead and downstream of the nozzle exits. Detailed measurements of heat transfer and pressure were also made both ahead and downstream of the injection stations, with the greatest concentration of measurements in the regions of shock wave/boundary layer interaction. Figure 7.2 shows a photograph for the model used in this experimental study and the instrumentation layout on the model. Also shown are a typical segment of the test matrix and a set of measurements made in the program. The principal objectives of the experimental studies were to explore the effectiveness of film cooling in the presence of regions of shock wave/boundary layer interaction and, more specifically, to determine how boundary layer separation and the large recompression heating rates are modified by film cooling. Detailed distributions of heat transfer and pressure were obtained in the incident shock/wall jet interaction region for a series of shock strengths and impingement positions for the two nozzle heights. The major conclusion from these studies was that the cooling film could be readily dispersed by relatively weak incident shocks such that the peak heating in the recompression region was not significantly reduced by even the largest levels of film cooling. While, in the absence of film cooling, the interaction regions were unseparated, regions of boundary layer separation were induced in the film cooling layer, the size of which first increased and then decreased with increased film cooling. Surprisingly, the size of the separated regions and magnitude of the recompression heating were not strongly influenced by the thickness of the cooling film or point of shock impingement relative to exit plane of the nozzles. The measurements with and in the absence of shock interaction are compared with the results of earlier experimental studies and correlated in terms of the major parameters controlling these flows.

Organization of Information in RUNn.LTS Files

Line(s)	Description of Entry	Units
1	The run sequence number is the initial entry in the file. Lines 2 thru 7 contain the number of entries for the type of measurement [units] indicated:	
2	Pressure	[PSIA]
3	Skin Friction	[PSIA]
4	Force/Moment	[LBF/IN-LBF]
5	Heat Transfer	[BTU/Ft ² /SEC]
6	Calorimeter	[BTU/Ft ² /SEC]
7	Pressure (for separation from data levels in line 2)	[PSIA]

Let N be the total number of entries for all the types of measurement. Then, there follow three groups of N entries whose contents are:

Line(s)	Description of Entry
8,N+7	Group 1 -- Gauge labels within double quotes which may be preceded by a single non-blank character
N+8,2•N+7	Group 2 -- Gauge positions (inches) relative to a reference point provided in report documentation
2•N+8,3•N+7	Group 3 -- Data level in units appropriate to the type of measurement a) Heat transfer measurements may contain a second entry for the temperature at the surface in °R b) "N" indicates no measurement or nulled data

Thirteen values, one per line, corresponding to some of the conditions during the test follow:

Line(s)	Description of Entry	Units
3•N+8	Mi = Shock Tube Incident Shock Mach#	
3•N+9	Po = Reservoir Total Pressure	[PSIA]
3•N+10	Ho = Reservoir Total Enthalpy	[(Ft/sec) ²]
3•N+11	To = Reservoir Total Temperature	[°R]
3•N+12	M = Freestream Mach#	
3•N+13	U = Freestream Velocity	[Ft/sec]
3•N+14	T = Freestream Temperature	[°R]
3•N+15	P = Freestream Static Pressure	[PSIA]
3•N+16	Q = Dynamic Pressure = ½ • Rho • U ² /144	[PSIA]
3•N+17	Rho = Freestream Density	[Slugs/Ft ³]
3•N+18	Mu = Freestream Viscosity	[Slugs/Ft-sec]
3•N+19	Re = Freestream Reynolds Number	[Ft ⁻¹]
3•N+20	Po' = Pitot Pressure	[PSIA]

The remaining lines in the file contain a single character abbreviation from file CONFIGUR in column one followed by the datum for the associated model parameter.

Organization of Information in RUNn.LTS Files

56 Gauge positions follow:

Entry	Line#	Comment
0.0000	64	Press. gauge location
0.3750	65	Press. gauge location
0.7500	66	Press. gauge location
0.9375	67	Press. gauge location
1.1250	68	Press. gauge location
1.3125	69	Press. gauge location
1.5000	70	Press. gauge location
1.6875	71	Press. gauge location
1.8125	72	Press. gauge location
1.8750	73	Press. gauge location
1.9375	74	Press. gauge location
2.0000	75	Press. gauge location
2.0625	76	Press. gauge location
2.1250	77	Press. gauge location
2.1875	78	Press. gauge location
2.2500	79	Press. gauge location
2.3125	80	Press. gauge location
2.3750	81	Press. gauge location
2.5000	82	Press. gauge location
2.6875	83	Press. gauge location
3.0625	84	Press. gauge location
3.4375	85	Press. gauge location
3.8125	86	Press. gauge location
4.1875	87	Press. gauge location
1.2600	88	H.T. gauge location
1.3400	89	H.T. gauge location
1.5000	90	H.T. gauge location
1.5800	91	H.T. gauge location

Entry	Line#	Comment
1.8200	92	H.T. gauge location
1.9000	93	H.T. gauge location
2.0250	94	H.T. gauge location
2.0500	95	H.T. gauge location
2.0750	96	H.T. gauge location
2.1000	97	H.T. gauge location
2.1250	98	H.T. gauge location
2.1500	99	H.T. gauge location
2.1750	100	H.T. gauge location
2.1870	101	H.T. gauge location
2.2000	102	H.T. gauge location
2.2080	103	H.T. gauge location
2.2500	104	H.T. gauge location
2.2707	105	H.T. gauge location
2.2916	106	H.T. gauge location
2.3125	107	H.T. gauge location
2.3334	108	H.T. gauge location
2.3543	109	H.T. gauge location
2.3753	110	H.T. gauge location
2.3753	111	H.T. gauge location
2.4553	112	H.T. gauge location
2.6153	113	H.T. gauge location
2.6953	114	H.T. gauge location
2.7753	115	H.T. gauge location
2.8553	116	H.T. gauge location
2.9353	117	H.T. gauge location
3.0153	118	H.T. gauge location
3.0953	119	H.T. gauge location

56 Data levels follow:

Entry	Line#	Comment	Entry	Line#	Comment
"N"	120	Pressure data	3.1199E+01	132	Pressure data
2.9817E+00	121	Pressure data	4.9766E+01	133	Pressure data
4.8875E+00	122	Pressure data	1.0579E+02	134	Pressure data
4.4496E+00	123	Pressure data	8.7510E+01	135	Pressure data
2.4228E+00	124	Pressure data	6.0132E+01	136	Pressure data
1.2506E+00	125	Pressure data	3.1908E+01	137	Pressure data
9.3307E-01	126	Pressure data	2.5303E+01	138	Pressure data
2.3393E+00	127	Pressure data	2.5834E+01	139	Pressure data
5.2630E+00	128	Pressure data	2.1739E+01	140	Pressure data
7.0792E+00	129	Pressure data	1.6147E+01	141	Pressure data
1.3301E+01	130	Pressure data	9.5870E+00	142	Pressure data
1.7795E+01	131	Pressure data	4.3132E+00	143	Pressure data

Organization of Information in RUNn.LTS Files

Model parameters follow:

Entry	Line#	Comment
A 15.0	189	Parameter abbreviation, Value
B Blunt	190	Parameter abbreviation, Value
C 22.5	191	Parameter abbreviation, Value
D Yes	192	Parameter abbreviation, Value
E 20	193	Parameter abbreviation, Value
F 50	194	Parameter abbreviation, Value

A possible CONFIGUR file for the above model parameters is shown below.

A Angle of Attack (Degrees)
B Nose Type --
C Model Width (Inches)
D Angular Trip (Yes/No)
E Bluntness Ratio (Rn/Rb) (Percent)
F Heat Transfer Reference Run Number =

11. Spalding, D.B. and Chi, S.W., "The Drag of a Compressible Turbulent Boundary Layer on a Smooth Flat Plate with and without Heat Transfer," *Journal of Fluid Mechanics*, pp. 117-143, 1964.

12. Settles, G.S., and Perkins, J.J., "Upstream Influence Scaling of 2D and 3D Shock/Turbulent Boundary Layer Interactions at Compression Corners," AIAA81-0334, 19th Aerospace Sciences Meeting, 1981.

13. Korkegi, R.H., "A Simple Correlation for Incipient Turbulent Boundary Layer Separation Due to a Skewed Shock Wave," *AIAA Journal*, Vol. 11, No. 11, pp. 1578-1579, 1973.

14. Morkovin, M.V., "Instability, Transition to Turbulence and Predictability," Keynote Address to AGARD Symposium on Laminar-Turbulent Transition, Technical University of Denmark, Copenhagen, Denmark, 1977.

15. Fay, J.A. and Ridell, F.R., "Theory of Stagnation Point Heat Transfer in Dissociated Air," *Journal of Aeronautical Sciences*, Vol. 25, No. 2.

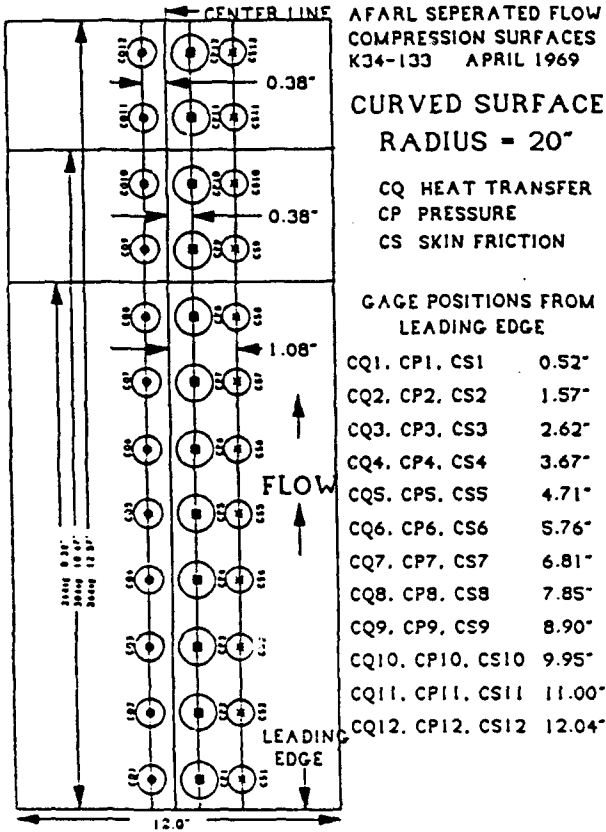


Model Photo Showing Curved Surfaces of Varying Radius and Length

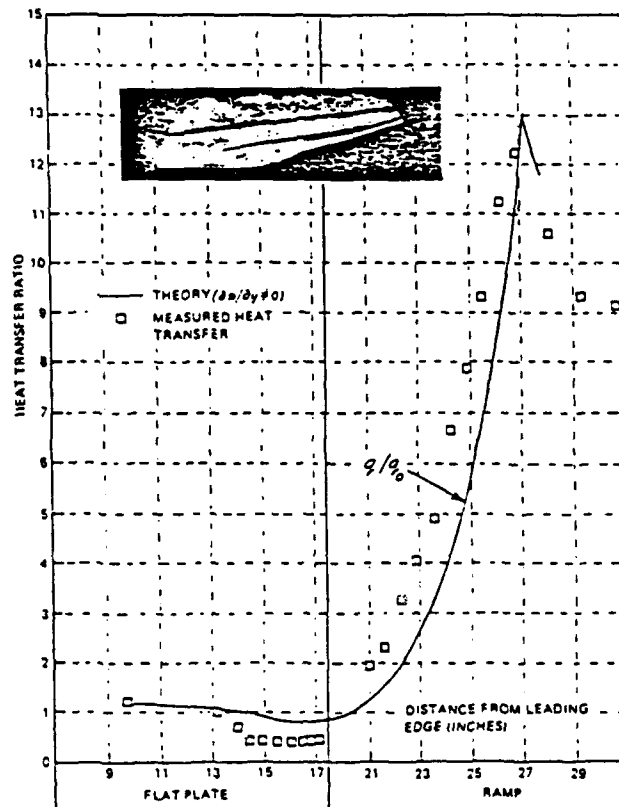
WORI AUTH W34-100 AFFIL 1960
 TEST MATRIX - AFARL SEPARATED FLOW - COMPRESSION SURFACES

RUN	LEADING EDGE EXTENSION (INCHES)	WEDGE ANGLE (DEG)	CURVED SURFACE RADIUS LENGTH (INCHES)	FREE STREAM MACH NUMBER	RE/FT (1/FT)
2	5.00	18	4 1.88	14.05	7.46E+04
5	5.00	24	4 2.51	14.05	6.64E+04
7	5.00	18	10 3.77	14.05	7.15E+04
8	5.00	18	10 3.77	14.08	1.72E+05
9	5.00	24	10 5.05	14.04	6.97E+04
12	5.00	15	0 -	14.05	7.34E+04
13	5.00	18	0 -	14.07	6.87E+04
14	5.00	24	0 -	14.05	7.11E+04
19	NONE	24	20 8.58	14.41	1.87E+05
20	NONE	30	20 10.47	15.98	7.02E+04
24	NONE	24	20 8.58	14.41	7.07E+04

Segment of Test Matrix

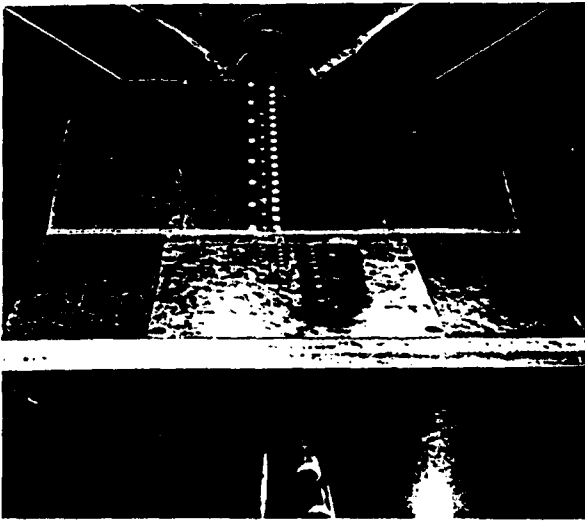


Model Gage Diagram



Comparison of Theory and Experimental Heat Transfer Measurements $M_\infty = 14.5$, $Re/Ft = 1.8 \times 10^5$, $\Theta_w = 18^\circ$

Figure 2.3 Study of Laminar Separated Viscous/Inviscid Interaction Regions Over Curved Compression Ramps at $M = 14$



Blunted Flat Plate Wedge Model Mounted in 6-Foot Tunnel

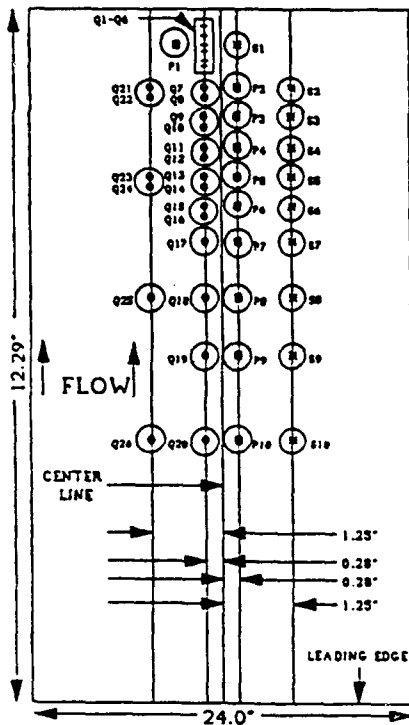
BLUNTNESS TEST

RUN #	M ∞	Re/ft. (1/ft.)	LEADING EDGE (IN.)	WEDGE ANGLE (DEG.)
5	19.8	1.04E+05	SHARP	25.500
6	19.8	1.04E+05	.20d CYL.	17.750
7	19.8	1.04E+05	.20d CYL.	23.917
8	19.8	1.04E+05	.20d CYL.	27.800
9	19.8	1.04E+05	.20d CYL.	20.167
13	19.8	1.04E+05	.71 FLAT	17.783
14	19.8	1.04E+05	.71 FLAT	13.933
15	19.8	1.04E+05	.71 FLAT	25.533
21	19.8	1.04E+05	.07d CYL.	17.917
24	19.8	1.04E+05	.07d CYL.	25.667
25	19.8	1.04E+05	.07d CYL.	21.667
31	19.8	1.04E+05	.007 FLAT	17.750
32	19.8	1.04E+05	.007 FLAT	21.683
33	19.8	1.04E+05	.007 FLAT	25.717

Test Matrix

SEPARATED FLOW - BLUNTNESS EFFECTS

K34-120 SEP 1967



Model Gage Diagram

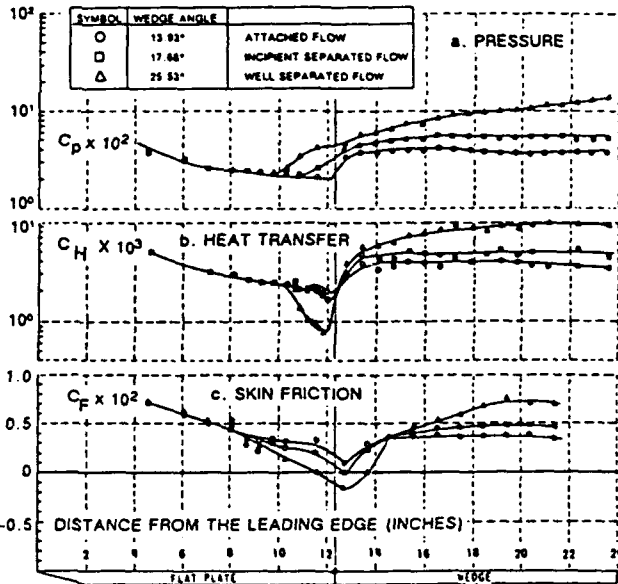
FLAT PLATE

Q HEAT TRANSFER
P PRESSURE
S SKIN FRICTON

GAGE DISTANCES
FROM LEADING EDGE

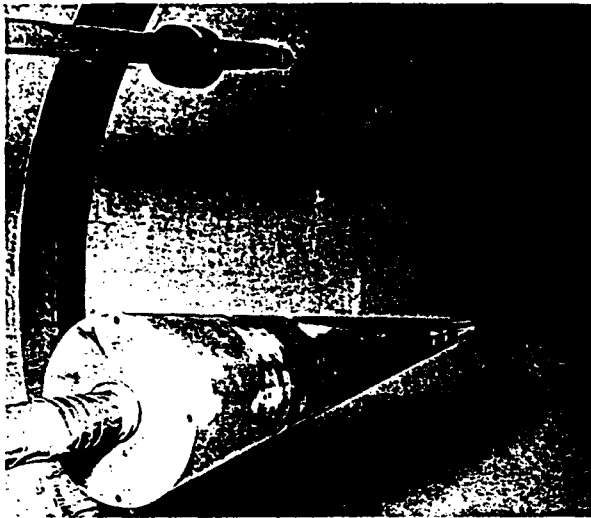
Q1	11.99"
Q2	11.84"
Q3, P1, S1	11.68"
Q4	11.53"
Q5	11.40"
Q6	11.24"
Q7, P2, S2	10.92"
Q8	10.72"
Q9, P3, S3	10.37"
Q10	10.19"
Q11, P4, S4	9.84"
Q12	9.66"
Q13, P5, S5	9.31"
Q14	9.13"
Q15, P6, S6	8.78"
Q16	8.39"
Q17, P7, S7	8.14"
Q18, P8, S8	7.14"
Q19, P9, S9	6.14"
Q20, P10, S10	4.84"

GAGES NOT USED:
Q21-Q26



The Distribution of Skin Friction, Pressure and Heat Transfer on the 0.71" Flat-Ended Blunt Flat Plate-Wedge Model

Figure 2.5 Study of Leading Edge Bluntness Effects on Laminar Separated Flows (M = 14 to 20)



6° Cone Model Mounted in 96 inch Tunnel

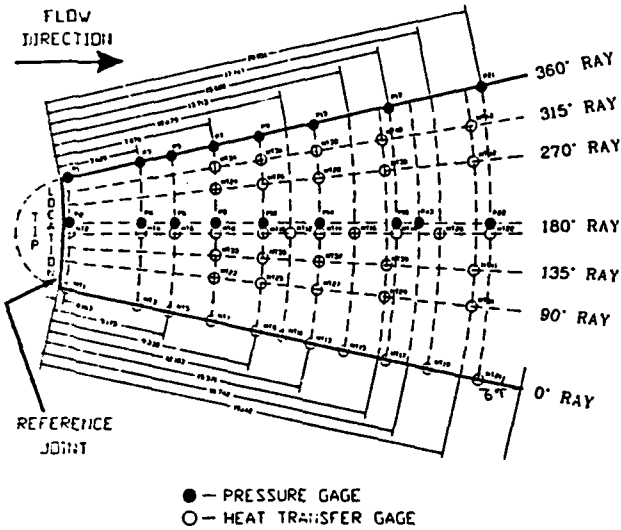
BODY FIXED TRANSITION TEST

RUN #	HACH #	Re/ft.	ATTACK (deg)	TIP	ROUGHNESS (mile)
8	11.30	1.1E+07	2.983	21% SPHERE	N/A
10	11.30	1.1E+07	1.983	21% SPHERE	N/A
12	11.30	1.1E+07	0.983	21% SPHERE	N/A
14	11.30	1.1E+07	0.017	21% SPHERE	N/A
15	11.30	1.1E+07	0.017	12% SPHERE	N/A
16	11.30	1.1E+07	-0.050	12% SPHERE	N/A
18	11.30	1.1E+07	-0.017	12% SPHERE	0.0037
21	11.30	1.1E+07	0.017	6% SPHERE	N/A
22	11.30	1.1E+07	1.017	6% SPHERE	0.0037
23	11.30	1.1E+07	1.017	6% SPHERE	0.0050
24	11.00	3.2E+06	1.017	6% SPHERE	0.0050
27	11.30	1.1E+07	1.017	6% SPHERE	0.0050
28	11.30	1.1E+07	1.017	6% SPHERE	0.0008
29	11.30	1.1E+07	1.017	6% SPHERE	N/A
30	11.30	1.1E+07	0.017	12% AB EL	N/A
31	11.30	1.1E+07	0.017	NASA INT.	N/A
32	11.30	1.1E+07	0.017	12% AB EL	2 GROOVES
33	11.30	1.1E+07	0.017	12% AB EL	N/A
34	11.30	1.1E+07	0.017	12% AB EL	1 GROOVE
35	11.30	1.1E+07	0.017	12% AB EL	N/A
36	11.30	1.1E+07	0.017	9.5% AVED	N/A
37	11.30	1.1E+07	0.017	12% AB EL	1 CIRCUM GAP
38	11.30	1.1E+07	0.017	12% AB EL	3/8 GAP
39	11.30	1.1E+07	0.017	12% AB EL	2 3/8 GAPS
41	11.30	1.1E+07	0.017	12% AB EL	2 CIRCUM GAP
42	11.30	1.1E+07	0.017	12% AB EL	1 CIRCUM GAP
43	11.30	1.1E+07	0.017	12% AB EL	STEP GAP
45	13.20	3.2E+06	3.017	6% SHARP	N/A

Segment of Test Matrix

6° CONE GAGE LOCATIONS (WITHOUT CONE TIP)
SURFACE DISTANCES FROM REFERENCE JOINT (INCHES)

NOTE: FOR GAGE LOCATION FROM LEADING EDGE, ADD APPROPRIATE TIP LENGTH TO THE DISTANCE FROM REFERENCE JOINT

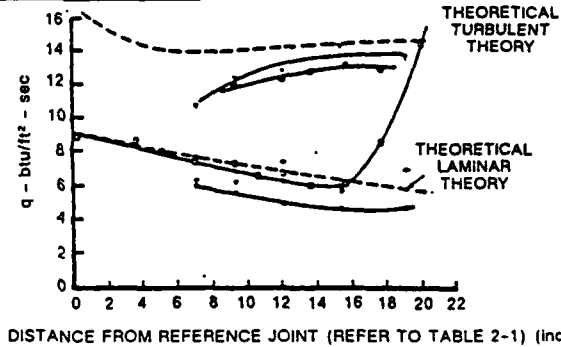
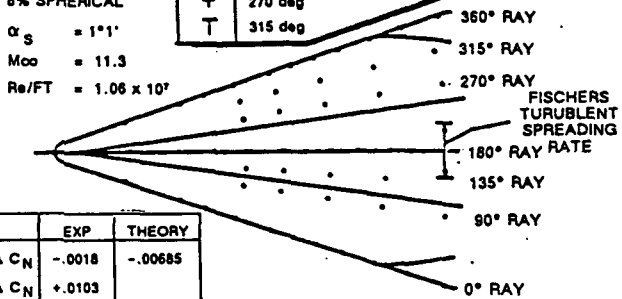


Model Gage Diagram

SYM	RAY
□	0 DEG (BOTTOM-WINDWARD)
X	90 DEG
Y	135 DEG
⊠	180 DEG (TOP-BOTTOM)
+	270 deg
T	315 deg

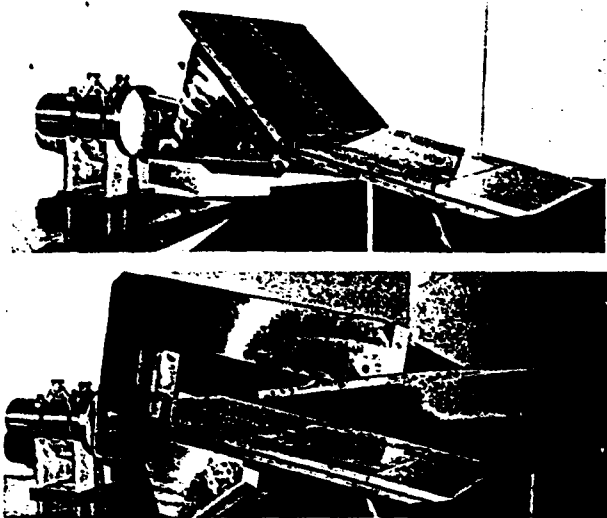
RUN 28
8% SPHERICAL
 $\alpha_s = 1^\circ 1'$
 $M_\infty = 11.3$
 $Re/FT = 1.06 \times 10^7$

	EXP	THEORY
ΔC_N	-0.0018	-0.00685
ΔC_D	+0.0103	



A Body-Fixed Transition Region Induced by Surface Roughness

Figure 3.3 Studies of Laminar, Transitional, and Turbulent Flows on Sharp and Blunted Cones (M = 11 to 13)

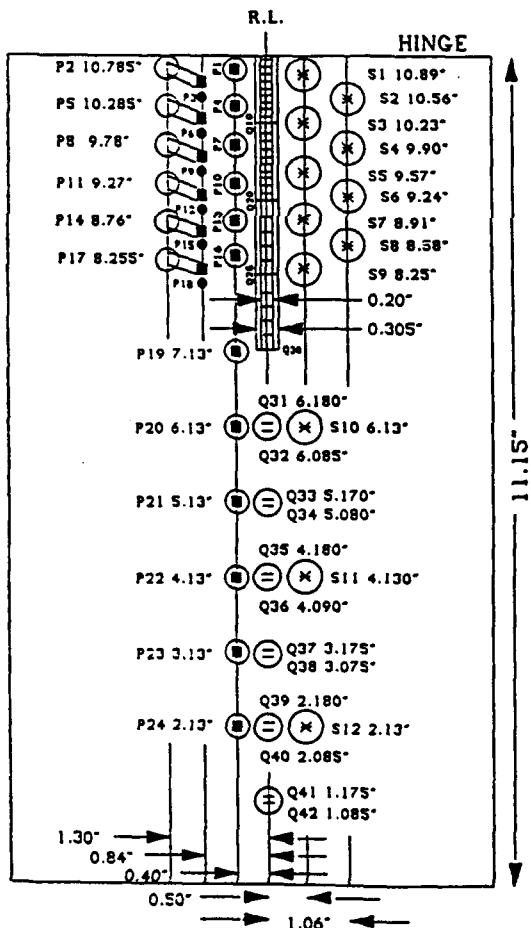


Flat Plate Wedge and Incident Shock Models

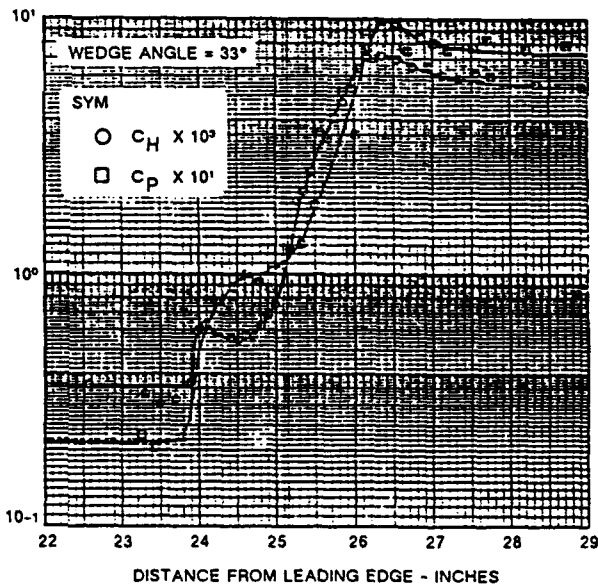
RUN#	MACH#	Re/ft.	ANGLE (DEG.)	DEVICE
2	7.9	1.72E+07	0.00	WEDGE
11	8.2	3.22E+07	27.00	WEDGE
12	8.2	4.18E+07	27.00	WEDGE
13	7.9	1.72E+07	30.00	WEDGE
15	8.2	3.22E+07	30.00	WEDGE
16	8.2	4.18E+07	30.00	WEDGE
17	7.9	1.72E+07	33.00	WEDGE
18	8.2	3.22E+07	33.00	WEDGE
19	8.2	4.18E+07	33.00	WEDGE
22	8.2	5.89E+07	33.00	WEDGE
23	8.2	3.22E+07	36.00	WEDGE
24	8.2	4.18E+07	36.00	WEDGE
26	7.9	1.72E+07	30.00	WEDGE
27	8.2	3.22E+07	30.00	WEDGE
28	8.2	4.18E+07	30.00	WEDGE
31	8.2	4.18E+07	27.00	WEDGE
34	8.2	4.18E+07	33.00	WEDGE
35	8.2	5.89E+07	30.00	WEDGE
36	8.2	3.22E+07	15.00	S.G.
37	7.9	1.72E+07	15.00	S.G.
38	8.2	4.18E+07	15.00	S.G.
39	7.9	1.72E+07	17.50	S.G.
40	8.2	3.22E+07	17.50	S.G.
41	8.2	4.18E+07	17.50	S.G.

FLAT PLATE GAGE DIAGRAM
 TURBULENT SEPARATED FLOW - FLAT PLATE
 S46-100 FEBRUARY - MARCH 1973

Q HEAT TRANSFER P PRESSURE S SKIN FRICTION



Segment of Test Matrix



Distribution of Heat Transfer and Pressure for Attached and Small Separated Regions in Wedge-Induced Flow
 ($M_\infty = 8.2$, $Re/Ft = 4.2 \times 10^7$)

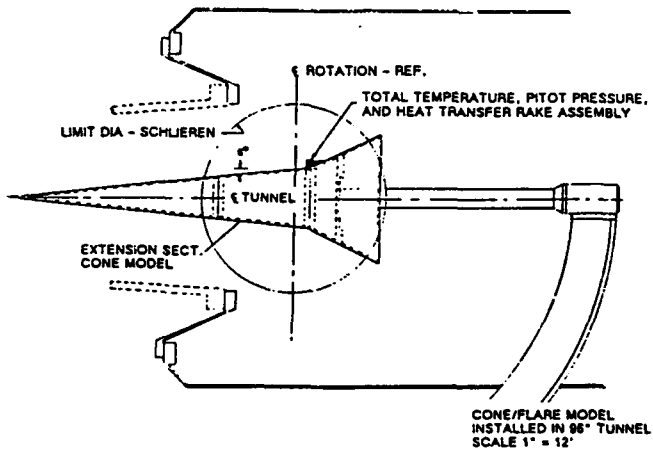
Figure 4.3 Studies of Wedge- and Shock-Induced Turbulent Attached and Separated Flows ($M = 8$)



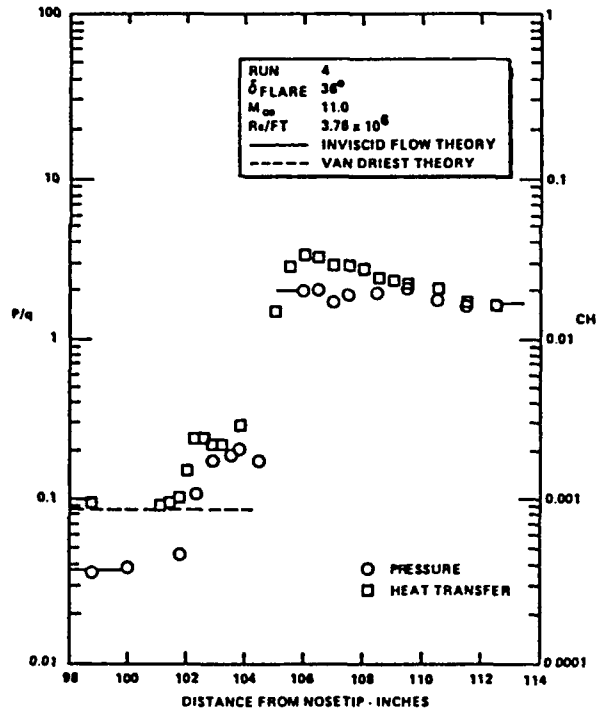
Cone/Flare Model Mounted in Shock Tunnel

RUNS	AIR			N ₂
	3.4.8	6.7	9	6-15
M ₀	3.345E+00	3.633E+00	4.200E+00	2.635E+00
P ₀ PSIA	7.216E+03	1.760E+04	1.705E+04	5.430E+03
H ₀ FT ² /SEC ²	1.825E+07	2.147E+07	2.795E+07	1.287E+07
T ₀ °R	2.717E+03	3.104E+03	3.875E+03	1.939E+03
M	1.096E-01	1.301E+01	1.543E+01	1.111E-01
U FT/SEC	5.922E+03	6.458E+03	7.404E+03	4.981E+03
T °R	1.214E+02	1.026E+02	9.574E+01	8.065E+01
P PSIA	9.172E-02	7.345E-02	1.860E-02	6.698E-02
Q PSIA	7.721E+00	8.712E+00	3.104E+00	5.800E+00
H ₀ SLUGS/FT ³	6.340E-05	6.038E-06	1.631E-05	6.734E-05
μ SLUGS/FT-SEC	1.021E-07	8.634E-08	8.054E-08	6.783E-08
RE/FT	3.680E+06	4.544E+06	1.499E+06	4.945E+06
PITOT PSIA	1.431E-01	1.619E-01	5.798E+00	1.070E-01

Segment of Test Matrix

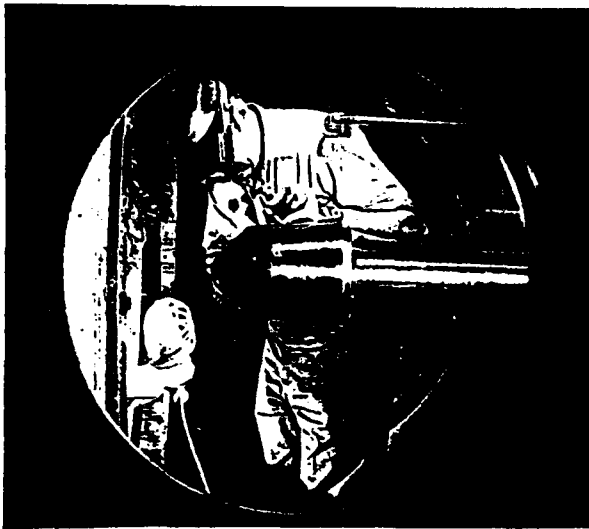


Model Gage Diagram



Distribution of Pressure and Heat Transfer in Attached Flow Over the 6° Cone/36° Flare

Figure 4.5 Attached and Separated Turbulent Flows on Large Cone/Flare Model, M=11 to 16



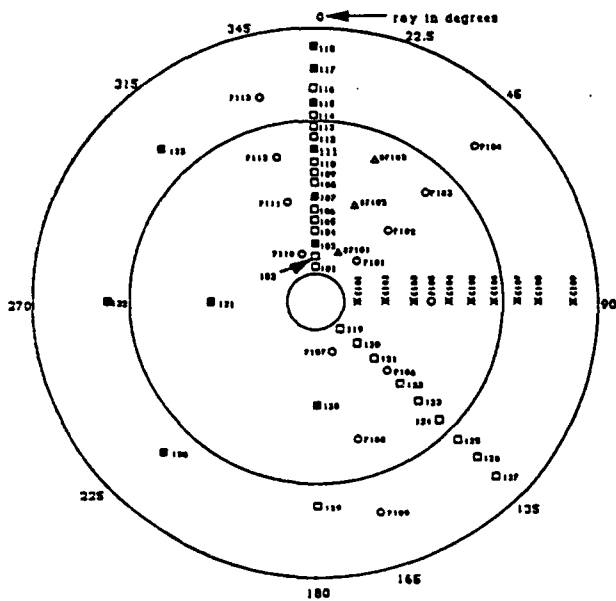
Rough Biconic Model Mounted in 96-inch Tunnel

BICONIC 3 TEST MATRIX

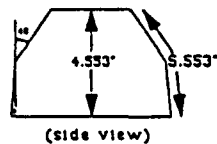
RUN	NOSETIP	ATTACK ANGLE (DEG)	ROLL (DEG)	MACH #	Re/FT (1/FT)	ROUGHNESS (MILS)
1	SHARP	0	0	11.33	1.009×10^{-7}	.004
2	MEDIUM	0	0	11.33	1.017×10^{-7}	.004
3	BLUNT	0	0	11.33	1.026×10^{-7}	.004
5	SHARP	0	0	7.912	8.287×10^{-6}	.004
7	SHARP	0	0	8.190	3.881×10^{-7}	.004
8	MEDIUM	0	0	8.190	4.043×10^{-7}	.004
10	BLUNT	0	0	8.185	3.867×10^{-7}	.004
11	SHARP	0	0	7.860	7.910×10^{-6}	0
12	SHARP	0	0	7.910	7.857×10^{-6}	0
13	SHARP	0	0	8.200	3.933×10^{-7}	0
14	BLUNT	0	0	8.190	3.760×10^{-7}	0
15	MEDIUM	0	0	8.190	3.942×10^{-7}	0
16	MEDIUM	0	0	11.34	1.035×10^{-7}	0
17	MEDIUM	10	0	11.33	9.977×10^{-6}	0
18	MEDIUM	10	45	11.35	1.002×10^{-7}	0
19	MEDIUM	20	0	11.33	1.057×10^{-7}	0
20	MEDIUM	20	45	11.34	1.021×10^{-7}	0
21	MEDIUM	20	0	10.19	2.367×10^{-5}	0
22	SHARP	0	0	11.33	1.018×10^{-7}	0

Segment of Test Matrix

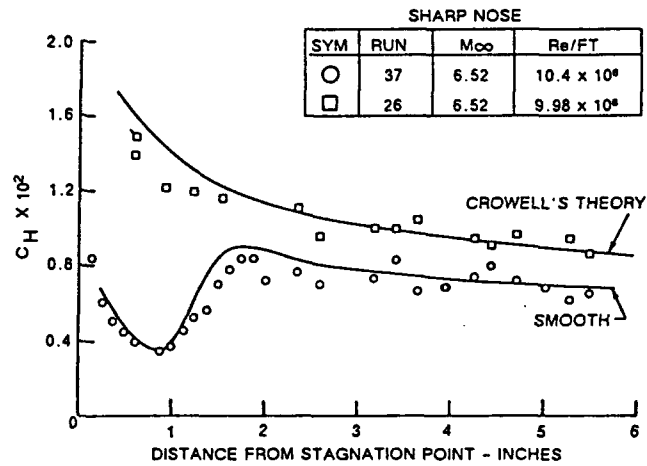
BICONIC III - FRUSTUM (aerial view)



- ✕ calorimeter
- heat transfer (1/8" gage)
- heat transfer (1/4" gage)
- pressure
- △ skin friction

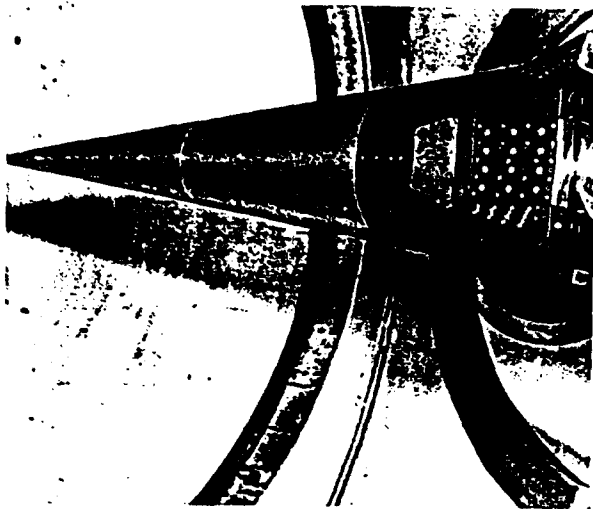


Model Gage Diagram

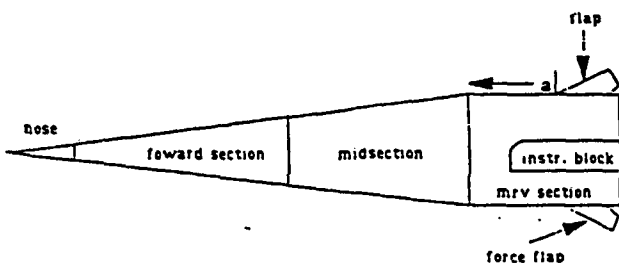


Comparison of Crowell's Prediction Method with Rough and Smooth Wall Measurements

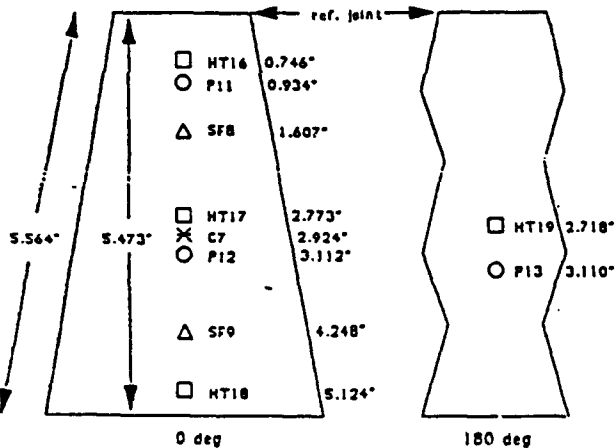
Figure 5.3 Studies of Laminar, Transitional, and Turbulent Flows on Smooth and Sand-Grain Rough Biconic Nostetips, M = 8 to 13



6° Cone Model Mounted in 96-inch Tunnel



MRV - 6 Degree Cone - Sand Grain Roughness
10.4 Degree Forward Section



× Calorimeter ○ Pressure
□ Heat Transfer △ Skin Friction

Model Gage Diagram

Figure 5.5 Studies of Laminar, Transitional, and Turbulent Flows on Smooth and Sand-Grain Rough 6-Degree Cones, $M = 11$

SMOOTH TESTS

RUN SEQUENCE	FORECONE ANGLE (degrees)	ANGLE OF ATTACKS (degrees)	CONE INSTRUMENT. LOCATIONS (degrees)	BLUNTNESS RATIOS (Rn/Rb)
2-9,45-47	6	0,8,16	0	0 (sharp)
10-44	10.4	0,4,8,12,16	0,90,180	0,8.5,14

10 mil ROUGHNESS TESTS

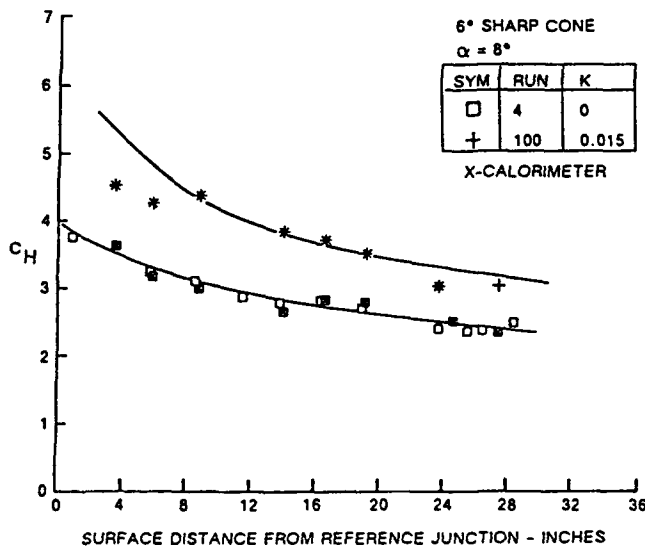
RUN SEQUENCE	FORECONE ANGLE (degrees)	ANGLE OF ATTACKS (degrees)	CONE INSTRUMENT. LOCATIONS (degrees)	BLUNTNESS RATIOS (Rn/Rb)
48-58	6	0,4,8,16	0,90	0
59-96	10.4	0,4,8,12,16	0,180	0,8.5,14

15 mil ROUGHNESS TESTS

RUN SEQUENCE	FORECONE ANGLE (degrees)	ANGLE OF ATTACKS (degrees)	CONE INSTRUMENT. LOCATIONS (degrees)	BLUNTNESS RATIOS (Rn/Rb)
97-109	6	0,4,8,16	0,90,180	0,8.5,14
110-114	10.4	0	90	0,8.5,14

ALL SMOOTH AND ROUGH TESTS PERFORMED AT 11.3 NOMINAL FREESTREAM MACH# AND 1.0E+07 NOMINAL REYNOLDS#/Ft

Segment of Test Matrix



Heat Transfer Distributions Along a 6° Cone with Smooth and 15 mil "Sand Grain" Roughness

SINGLE SHOCK TESTS

RUN SEQUENCE	SHOCK GENERATOR LENGTH (inches)	SHOCK GENERATOR ANGLE (degrees)
9-20	26.5	10
21-26	26.5	12.5
27-30	26.5	15
33-37	26.5	10
42-44	48.0	10
59-69	26.5	12.5
99	26.5	12.5
100	26.5	10
101	26.5	12.5
102-103	46.3	10
104	44.0	10
106-113	46.3	10
114-116	44.0	12.5

SWEPT SHOCK TESTS

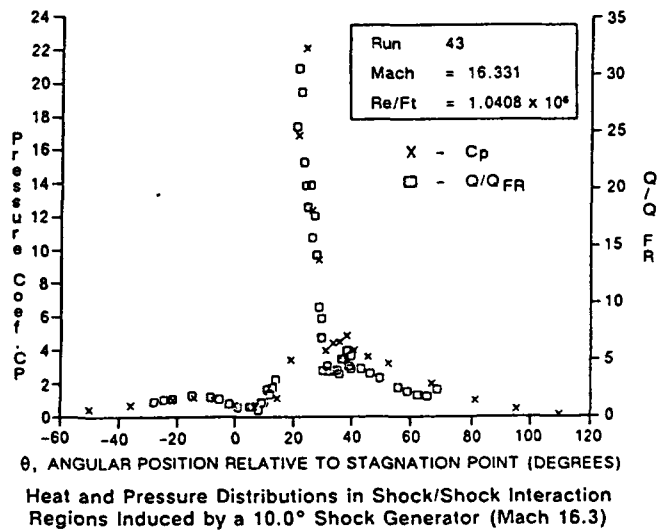
RUN SEQUENCE	SHOCK GENERATOR LENGTH (inches)	SHOCK GENERATOR ANGLE (degrees)	SWEEP ANGLE (degrees)
64	26.5	12.5	0
66-73	26.5	12.5	15
75-80, 98	26.0	12.5	30

MULTIPLE SHOCK TESTS

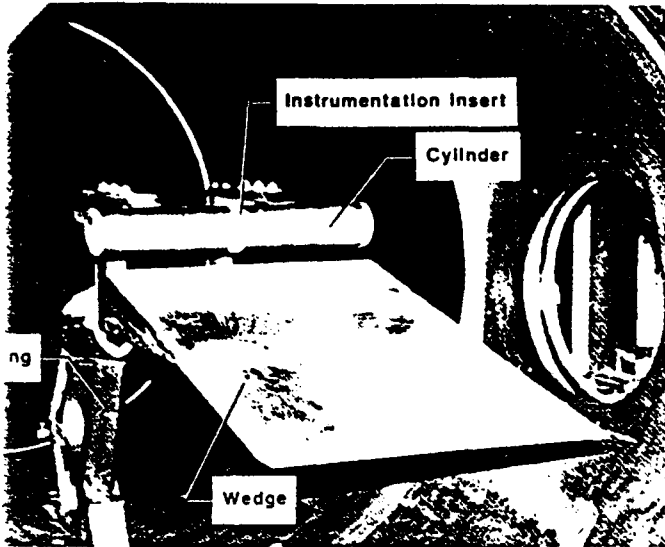
RUN SEQUENCE	S.G. LENGTH (inches)	S.G. ANGLE (degrees)	RAMP LENGTH (inches)	RAMP ANGLE (degrees)
82	36.0	7.5	-	-
83-85	36.0	7.5	14.0	5.0
86	36.0	7.5	11.0	6.0
87-88	36.0	7.5	14.0	5.0
89	36.0	7.5	-	-
90-91	36.0	7.5	11.0	6.0
92-93	36.0	7.5	13.25	6.0
94	36.0	7.5	11.0	6.0
95	36.0	7.5	13.25	6.0

MACH NUMBERS FROM 6 TO 19, Re/Ft FROM 1.6E+05 TO 5.0E+06

Segment of Test Matrix



Heat and Pressure Distributions in Shock/Shock Interaction Regions Induced by a 10.0° Shock Generator (Mach 16.3)



2-D Cylinder/Shock Generator Model Mounted

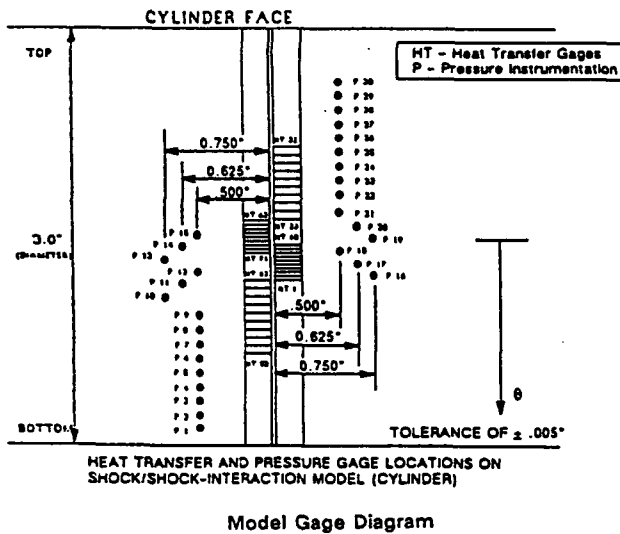
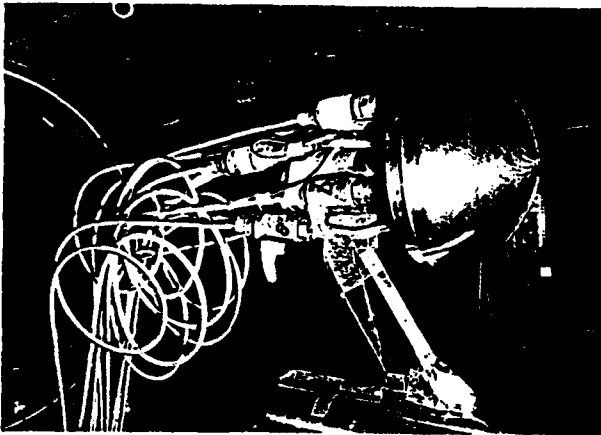
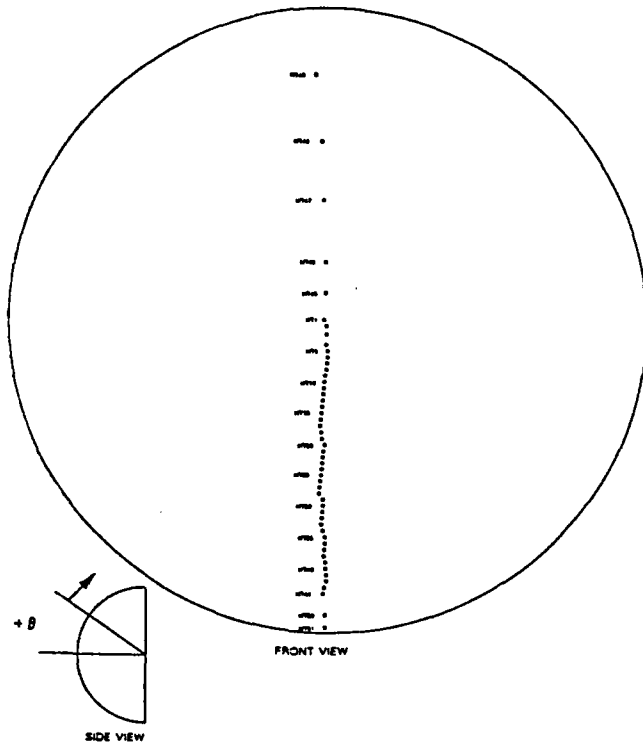


Figure 6.2 Studies of Heat Transfer and Pressure in Regions of Shock/Shock Interaction Over Swept and Unswept 2-D Cylinder, M = 6 to 19



Transpiration-Cooled Hemisphere Mounted in Shock Tunnel



Model Gage Diagram

RUN	TC†	Mach	Re/ft	λ	S.G. CONFIGURATION		
					Lip Rad. (inches)	A* (inches)	B* (inches)
4	1	12.1	3.3E-05	0.07	.	.	.
5	1	12.1	3.2E-05	0	.	.	.
6	1	12.1	3.3E-05	0.08	.	.	.
7	1	12.1	3.3E-05	0.12	.	.	.
8	1	12.1	3.3E-05	0.16	.	.	.
10	1	12.1	3.1E-05	0.15	.	.	.
13	2	12.6	1.5E-06	0	.	.	.
14	2	12.6	1.5E-06	0.06	.	.	.
15	2	12.6	1.3E-06	0.06	.	.	.
16	1	12.1	3.2E-05	0	Rat	11.860	3.121
17	1	12.1	3.1E-05	0	Rat	10.360	3.121
18	1	12.1	3.3E-05	0	Rat	9.375	3.295
19	1	12.1	3.1E-05	0	3/8	9.375	3.295
20	1	12.1	3.2E-05	0.12	Rat	9.375	3.295
21	1	12.1	3.0E-05	0.17	Rat	9.375	3.295
22	1	12.1	3.1E-05	0	5/16	9.375	3.295
23	1	12.1	3.1E-05	0	5/16	9.375	3.295
24	1	12.1	3.0E-05	0	5/16	10.375	3.295
25	1	12.1	3.1E-05	0	5/16	10.875	3.295
27	1	12.1	3.4E-05	0.15	5/16	9.375	3.295
28	1	12.1	3.4E-05	0.20	5/16	9.375	3.295
29	1	12.1	3.4E-05	0.26	5/16	9.375	3.295
30	1	12.1	3.5E-05	0.31	5/16	9.375	3.295
31	1	12.2	3.6E-05	0	5/16	9.375	3.295
33	1	12.2	3.6E-05	0.19	5/16	9.128	3.338
34	1	12.1	3.5E-05	0.31	5/16	9.128	3.338
35	1	12.2	3.5E-05	0.36	5/16	9.128	3.338
36	1	12.2	3.6E-05	0	5/16	9.128	3.338
37	1	12.2	3.5E-05	0	5/16	9.728	3.338
38	1	12.2	3.6E-05	0	5/16	11.428	3.338
39	1	12.2	3.5E-05	0	5/16	8.636	3.425
40	1	12.2	3.4E-05	0	5/16	8.636	3.425
41	1	12.2	3.3E-05	0.20	5/16	8.636	3.425
42	1	12.2	3.5E-05	0.31	5/16	8.636	3.425
43	1	12.2	3.5E-05	0.36	5/16	8.636	3.425
44	1	12.2	3.3E-05	0	5/16	8.143	3.512
45	1	12.2	3.2E-05	0.20	5/16	8.143	3.512
46	1	12.2	3.4E-05	0.32	5/16	8.143	3.512
47	2	12.6	1.3E-06	0	5/16	9.728	3.338
48	2	12.6	1.3E-06	0.06	5/16	9.728	3.338
49	3	12.2	2.0E-05	0	5/16	10.428	3.338
50	3	12.1	2.1E-05	0	5/16	9.128	3.338
51	3	12.1	2.0E-05	0.20	5/16	9.128	3.338
52	3	12.2	2.1E-05	0.24	5/16	9.128	3.338
53	3	12.2	2.2E-05	0	5/16	10.028	3.338
54	1	12.1	3.2E-05	0	5/16	9.128	3.338
55	1	12.1	3.3E-05	0.39	5/16	9.128	3.338
56	1	12.1	3.4E-05	0.30	5/16	8.636	3.425
57	1	12.1	3.4E-05	0.34	5/16	8.636	3.425
58	1	12.2	3.5E-05	0.28	5/16	8.143	3.512
60	4	16.1	3.2E-05	0	5/16	8.743	3.512
61	5	15.3	6.3E-04	0	5/16	8.743	3.512
62	1	12.1	3.1E-05	0	.	.	.

† Test Conditions (Tcs) (Re/M_∞ Pairings) Are Shown in Figure 4a.
* Refer to Figure 9.

Segment of Test Matrix

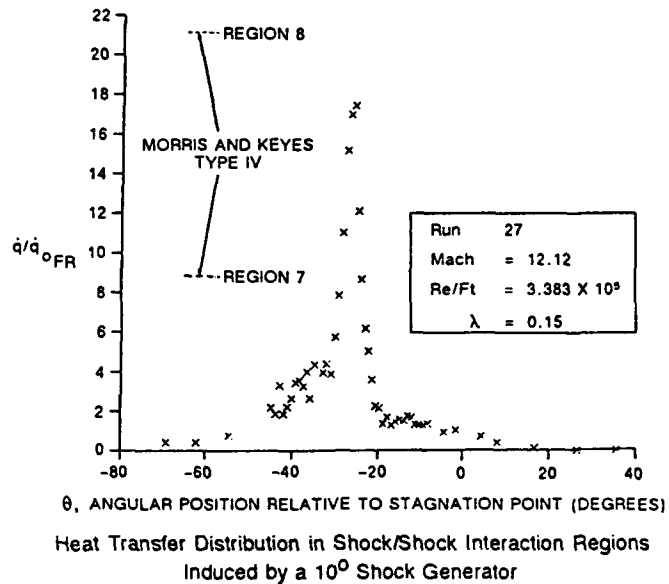


Figure 6.3b Studies of Heat Transfer and Pressure in Regions of Shock/Shock Interaction Over Transpiration-Cooled Spherical Nosetips

Capsule: Shock - Shock Interaction
 Runs: 9-22, 24, 26-44, 59-64, 66-95, 98-104, 106-110, 112-116/
 Title: "Studies of Aerothermal Loads Generated in Regions of Shock/Shock
 Interaction in Hypersonic Flow"
 Author: M.S.Holden, A.R.Weiting, J.R.Moselle, C.Glass
 Date: 8/86 - 9/87
 W/A: 25-576
 Report#: AIAA paper No. 8P-0477 (Jan 1988)

SHK-SHK Test Matrix

RUN	MACH	RE/FT	STAG GAGE	<----- MODEL PARAMETERS ----->				RAMP PARAMETERS			
				CLEARANCES		ANGLE	LENGTH	SWEEP	ANGLE	LENGTH	DIST
				V (in)	H (in)	C (deg)	P (in)	ANGLE (deg)	D (deg)	W (in)	B (in)
9	6.35	4.50	P18	N/A	N/A	N/A	26.5	0.00	N/A	N/A	N/A
10	6.35	4.40	P18	3.20	0.09	10.0	26.5	0.00	N/A	N/A	N/A
11	6.35	4.40	P18	3.50	0.05	10.0	26.5	0.00	N/A	N/A	N/A
12	6.35	4.30	P21	3.34	0.06	10.0	26.5	0.00	N/A	N/A	N/A
13	6.35	4.40	P18	3.34	0.06	10.0	26.5	0.00	N/A	N/A	N/A
14	6.36	4.70	P23	3.55	0.09	10.0	26.5	0.00	N/A	N/A	N/A
15	6.33	2.40	P23	3.55	0.09	10.0	26.5	0.00	N/A	N/A	N/A
16	8.02	1.40	P23	2.95	0.06	10.0	26.5	0.00	N/A	N/A	N/A
17	8.06	1.50	P23	2.95	0.06	10.0	26.5	0.00	N/A	N/A	N/A
18	8.03	1.50	P21	2.86	0.50	10.0	26.5	0.00	N/A	N/A	N/A
19	8.03	1.50	P21	2.78	0.50	10.0	26.5	0.00	N/A	N/A	N/A
20	7.94	0.76	P21	2.78	0.50	10.0	26.5	0.00	N/A	N/A	N/A
21	8.03	1.60	P21	2.89	0.59	12.5	26.5	0.00	N/A	N/A	N/A
22	7.95	0.77	P21	2.89	0.59	12.5	26.5	0.00	N/A	N/A	N/A
24	8.14	3.80	P21	2.89	0.59	12.5	26.5	0.00	N/A	N/A	N/A
26	8.03	1.50	HT39	3.36	0.63	12.5	26.5	0.00	N/A	N/A	N/A
27	8.03	1.50	P21	2.95	0.31	15.0	26.5	0.00	N/A	N/A	N/A
28	7.93	0.72	P21	2.95	0.31	15.0	26.5	0.00	N/A	N/A	N/A
29	8.03	1.50	P23	3.19	0.31	15.0	26.5	0.00	N/A	N/A	N/A
30	8.15	1.80	P11	2.31	0.75	15.0	26.5	0.00	N/A	N/A	N/A
31	8.03	1.50	P18	N/A	N/A	N/A	N/A	0.00	N/A	N/A	N/A
32	6.38	5.00	P18	N/A	N/A	N/A	N/A	0.00	N/A	N/A	N/A
33	11.00	4.30	P21	2.00	0.44	10.0	26.5	0.00	N/A	N/A	N/A
34	11.01	4.40	P21	2.25	0.44	10.0	26.5	0.00	N/A	N/A	N/A
35	11.02	4.50	P21	2.72	1.81	10.0	26.5	0.00	N/A	N/A	N/A
36	11.01	4.30	P21	2.41	1.50	10.0	26.5	0.00	N/A	N/A	N/A
37	11.00	4.20	P21	2.41	2.10	10.0	26.5	0.00	N/A	N/A	N/A
38	11.00	4.30	P18	N/A	N/A	N/A	N/A	0.00	N/A	N/A	N/A
39	12.97	4.70	P18	N/A	N/A	N/A	N/A	0.00	N/A	N/A	N/A
40	16.50	1.20	P18	N/A	N/A	N/A	N/A	0.00	N/A	N/A	N/A
41	19.14	0.37	P18	N/A	N/A	N/A	N/A	0.00	N/A	N/A	N/A
42	16.31	1.00	P21	2.94	0.16	10.0	48.0	0.00	N/A	N/A	N/A
43	16.33	1.00	P23	3.63	0.09	10.0	48.0	0.00	N/A	N/A	N/A
44	16.27	0.94	P25	3.94	-0.25	10.0	48.0	0.00	N/A	N/A	N/A
59	8.04	1.40	P21	2.83	2.76	12.5	26.5	0.00	N/A	N/A	N/A
60	8.04	1.40	P21	3.19	1.81	12.5	26.5	0.00	N/A	N/A	N/A
61	8.05	1.50	P23	3.08	0.35	12.5	26.5	0.00	N/A	N/A	N/A
62	8.05	0.73	P24	3.08	0.35	12.5	26.5	0.00	N/A	N/A	N/A
63	7.75	0.37	P24	3.08	0.35	12.5	26.5	0.00	N/A	N/A	N/A

Figure 9.1 Format of Source Capsule and Test Matrix for Shock/Shock Interaction Database Available in CUBDAT

Sym Legend
 X Cp
 □ Q/Q(F-R)

Run 100
 HEAT AND PRESSURE DISTRIBUTION

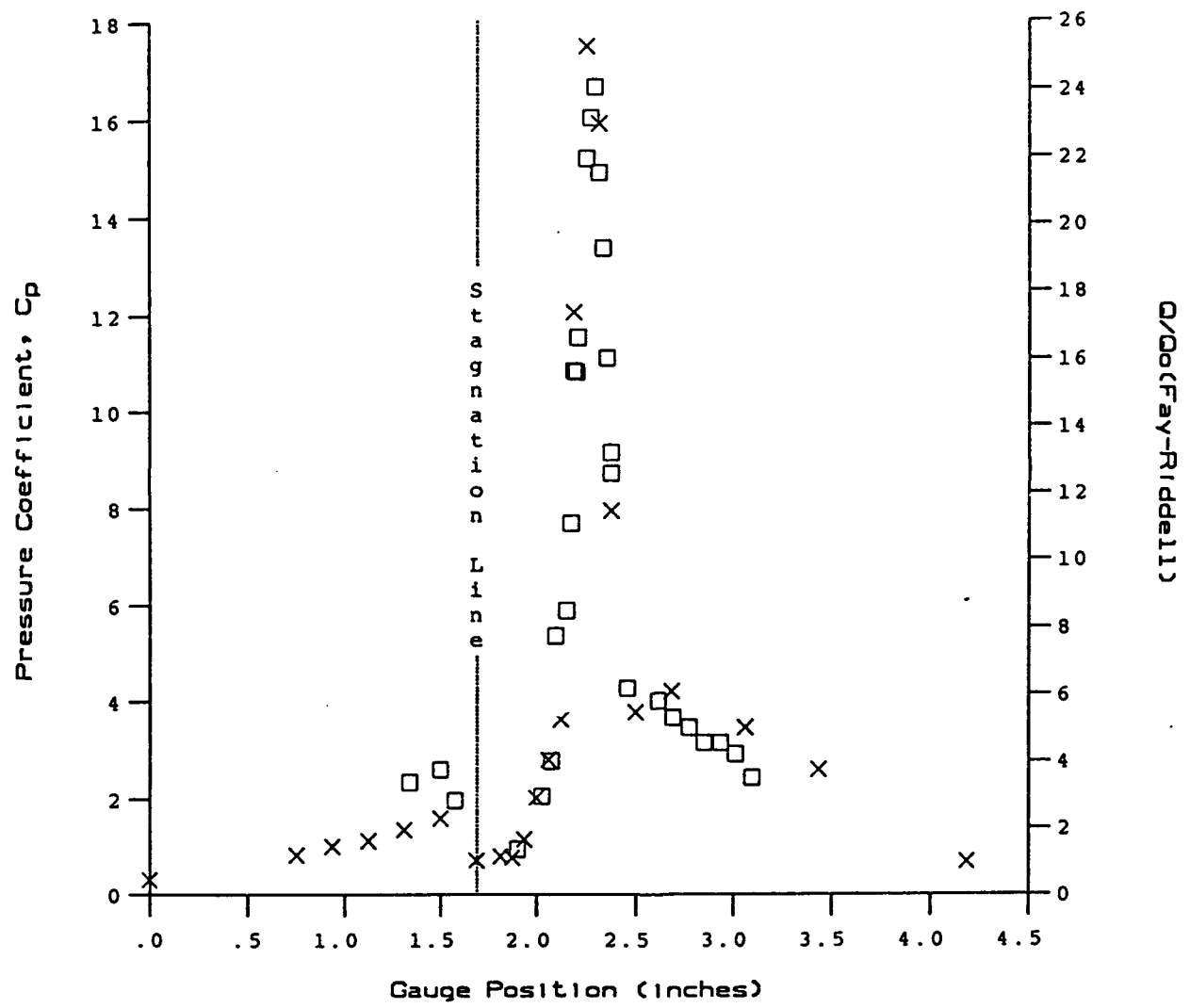


Figure 9.3 Typical Plots of the Heat Transfer and Pressure Distribution in Regions of Shock/Shock Interaction Which Can Be Obtained Directly from the CUBDAT Database

Appendix

Distribution of Program CUBDAT on 5-1/4" Floppy Diskettes

CUBDAT is a program which runs on an IBM PC AT or compatible computer having 640kB of RAM, hard disk, math coprocessor, graphics card and a 5-1/4" high density floppy drive. Under limited conditions, the program may be run from "MAIN_DISK", a bootable diskette which uses COMPAQ PC DOS Version 3.31. However, it is advisable to install the necessary software on the system hard disk and run the program there.

Until recently, program CUBDAT has been distributed to interested parties on a fixed number of 5-1/4", High Density (1.2MB), DOS formatted floppy diskettes. The experience gained as a result of that methodology has led to a more practical approach to handling the continually expanding database and the ability to correct errors detected after distribution. This document will discuss the rationale behind the structure of each diskette and serve as a guide for potential users.

CUBDAT, in its entirety, is delivered on four diskettes whose contents are described at the bottom of this page. However, in general practice, the data files from a single experimental study are delivered on a single diskette with the executable and configuration files needed to access them. In this instance CUBDAT may be run from diskette.

The current complete set of CUBDAT diskettes follows:

- | | | | |
|----|-----------|------------------------------------|-------------|
| 1. | MAIN_DISK | Executable and configuration files | |
| 2. | DISK_1 | Subdirectories | |
| | A. | BDYFIXTR | F. BLUNTLE |
| | B. | BICONIC3 | G. CURVSURF |
| | C. | BICONIC4 | H. INCIPEP |
| | D. | BLOWRUFF | I. LAMINAR |
| | E. | BLUNTBOD | |
| 3. | DISK_2 | Subdirectories | |
| | A. | MRVPAT | F. SWEPTSKU |
| | B. | MRVSAND | G. TURBFLO |
| | C. | NASAFP | |
| | D. | SEP-K90 | |
| | E. | SHK-SHK | |
| 4. | DISK_3 | Subdirectories | |
| | A. | SLOT_080 | F. CONEFLAR |
| | B. | SLOT_120 | G. SHK-COMP |
| | C. | SCANT | H. HEDI |
| | D. | SMTHBLW1 | I. SCRAMJET |
| | E. | SMTHBLW2 | |

Whenever CUBDAT is invoked the default drive and directory are checked for the existence of files "summary.fil" and "summary.mtx". An error message is delivered if either file is missing. The user is then asked to specify in which drive and directory the program is to confine its searches. Unless all files are copied to the hard disk, it is necessary to place the appropriate diskette in the floppy drive. Subsequently, a menu of options is presented which gives the user the ability to select a specific experimental run's data for plotting or tabulation. Reduced data may be stored for pressure, skin friction, force/moment, heat transfer and calorimeter measurements. Test conditions and model configuration parameters may also be displayed for individual runs. The data from a particular run is stored in an ASCII file named "run*.lts" (* = run sequence # w/o leading zeroes). These files are also capable of being "imported" to LOTUS 1-2-3.

prompt at the top of the display. The remaining executable files extract information from the "run*.lts" files and place it on program prescribed or user designated filenames. Each is used by first entering its name and then responding to the prompts.

Optimum use of CUBDAT can be obtained by copying all files from MAIN_DISK into a single subdirectory on the system's hard disk. CALSPAN will be assumed for the purpose of illustration but the user is free to choose any name which is unique to DOS. The "config.sys" file in the system's root directory should be edited to include the lines "files=20", "buffers=40" and "device=\calspan\plotdev.?" (see below) to provide the environment required to successfully execute CUBDAT. Always transfer to the CALSPAN subdirectory by entering "cd \calspan" before invoking CUBDAT.

A slight improvement in performance can be obtained by also copying the files from the remaining diskettes into appropriately named subdirectories. If space on the hard disk is limited, CUBDAT can be directed to search for data on the floppy drive.

A list of all filenames delivered on "MAIN_DISK", with remarks enclosed in parentheses, follows:

- ASCIIDAT.EXE (appends selected run info to file ASCIIDAT.OUT)
- AUTOEXEC.BAT (consult your DOS reference manual for file's content)
- BOOTDISK.DOC (enter "TYPE BOOTDISK.DOC" to display useful info)
- CLR.EXE (use instead of "CLS" to clear screen display)
- COMMAND.COM (needed for booting from MAIN_DISK)
- CONFIG.SYS (must contain "DEVICE=PLOTDEV.?" for ?=ATT,CGA,EGA or HGC)
- CUBDAT.EXE (invoke CUBDAT where SUMMARY.FIL and SUMMARY.MTX reside)
- DRAW.EXE (draws plot files created by CUBDAT)
- GETTALL.EXE (appends selected test conditions to ALLPARMS.LTS)
- GETMODEL.EXE (appends run information to MODELSIN.LTS)
- GETTCS.EXE (appends all test conditions to TESTCONS.LIS)
- IBMBIO.COM (system hidden file)
- IBMDOS.COM (system hidden file)
- PLOTDEV.ATT (CONFIG.SYS device name for COMPAQ plasma display)
- PLOTDEV.CGA (CONFIG.SYS device name for Color Graphics Adaptor (CGA))
- PLOTDEV.EGA (CONFIG.SYS device name for Enhanced Graphics Adaptor (EGA))
- PLOTDEV.HGC (CONFIG.SYS device name for Hercules Graphics Card (HGC))
- PSTEK.PRO (required to successfully run TEK2PS.EXE)
- SUMMARY.FIL (used by CUBDAT for valid study (directory) names)
- SUMMARY.MTX (used by CUBDAT for test matrix specifications)
- TABULATE.EXE (tabulates selected calibration type(s) to named file)
- TEK2PS.EXE (translates Tektronix plot files to PostScript)

CUBDAT was created for qualified requesters with the intention of providing a useful PC tool for accessing experimental data from Calspan's shock tunnels. In the course of time, the program has evolved based on in-house analysis and reporting needs. It is hoped that use of CUBDAT by others will lead to a greater understanding of the information contained in the data files and foster a dialogue to improve its usefulness. Toward that end, please address your comments to

John R. Moselle (716) 631-6850
Calspan Corporation
P.O. Box 400
Buffalo, NY 14225